MANIPULATING CELLS WITH A DYNAMICALLY RECONFIGURABLE ELECTRO-MAGNETIC COIL

A Dissertation

Presented to

the Faculty of the Department of Electrical and Computer Engineering

University of Houston

In Partial Fulfillment

of the Requirements for the Degree

Doctor of Philosophy

in Electrical Engineering

by

Ruoli Jiang

August 2015

MANIPULATING CELLS WITH A DYNAMICALLY RECONFIGURABLE ELECTRO-MAGNETIC COIL

Ruoli Jiang

Approved:

Chair of the Committee
Dr. Ben H. Jansen, Professor,
Electrical and Computer Engineering

Committee Members:

Dr. Ji Chen, Professor,
Electrical and Computer Engineering

Dr. David Jackson, Professor,
Electrical and Computer Engineering

Dr. Ralph Metcalfe, Professor,
Mechanical Engineering

Dr. Shoujun Xu, Associate Professor,
Chemistry

Dr. Suresh K. Khator, Associate Dean,
Cullen College of Engineering

Dr. Badrinath Roysam,
Professor and Department Chair,
Electrical and Computer Engineering

Acknowledgements

Although there is only my name on this dissertation, a great number of people have contributed to it. Thus my sincere gratitude goes to my parents, my advisor and all my friends for their love, support and patience for making this dissertation possible.

I would like to thank my advisor, Dr. Ben Jansen, who is one of the best teachers I have ever met. His experience and wisdom always helped me resolve tough problems in my research work. His patience and support helped me to overcome obstacles and to finish the dissertation. I would also like to thank Dr. Ji Chen, Dr. David Jackson, Dr. Ralph Metcalfe, and Dr. Shoujun Xu for serving as members of my dissertation committee and for their valuable suggestions. Thanks to my partners, Wunjun Zhao, Rui Cheng, and Dr. Leidong Mao at the University of Georgia Athens, without their help I would not have been able to finish the experiment.

Most importantly, none of this would have been possible without the love and care of my family. My parents Xiaoqin Jiang and Hong Zhou, my uncle John Carter and aunt Bing Carter have always supported me. Thanks to my friends, my roommates, Cissy and my band Random.

This work was supported by grant 5R21GM104528-02 from NIH to University of Georgia and University of Houston.

MANIPULATING CELLS WITH A DYNAMICALLY RECONFIGURABLE ELECTRO-MAGNETIC COIL

A Dissertation

Presented to

the Faculty of the Department of Electrical and Computer Engineering

University of Houston

In Partial Fulfillment

of the Requirements for the Degree

Doctor of Philosophy

in Electrical Engineering

by

Ruoli Jiang

August 2015

Abstract

Current cancer screening techniques are often labor-intensive, require high initial costs, and are difficult to apply to cytology samples because of their heterogeneous nature. To address these issues, we are participating in a project to develop a low-cost chip for cell enrichment. The proposed system uses water-based bio-compatible ferrofluids as a uniform magnetic environment that surrounds the non-magnetic (cancer) cells within a set of microfluidic channels and reservoirs. The novelty of our approach is that we apply an external magnetic field generated by a dynamically-reconfigurable electromagnetic coil. The magnetic field will push away the non-magnetic objects (including cancer cells) so that they can be potentially trapped, manipulated, and directed towards a specific location. In this research, we developed the reconfigurable electromagnetic coil with the help of a mathematical model of the motion of non-magnetic particles in ferrofluids induced by (changing) magnetic fields. This model was used to compute the magnetic fields required for effective particle manipulation. Test results of an actual microfluidic device equipped with our electromagnetic coil are presented. A microfluidic device with electromagnetic wire-mesh coil has been developed. Bench experiments on single wire and parallel wires configurations have achieved non-magnetic trapping and manipulation with speed around 50 μm/s. Experiments with the figure-eight coil configuration differed from the simulations, but a 'sandwich' type coil could improve on these results.

Table of Contents

List of Figures

List of Tables

Chapter 1 Introduction

1.1 Essential Background

1.1.1 Cell Sorting

Exfoliated cervical cytology, the Pap test, has been the basis of effective cervical cancer screening. However, substantial inter-observer variability exists in interpreting cervical cytology. Cytology screening requires an expensive infrastructure and highly trained cytotechnologists, limiting its implementation in low resource settings with the highest burden of disease. High-risk human papillomavirus (HR-HPV) testing increases the sensitivity of screening, but specificity remains relatively low, especially in younger women with high HPV prevalence. Recently-developed prophylactic HPV vaccines have promise, but their implementation is hampered by the high cost of introducing a comprehensive cervical cancer control program involving vaccination, screening and treatment. Therefore, easy to use objective screening tests are needed to improve the efficiency of cervical cancer screening. Biomarkers based on molecular changes in response to HPV infection and neoplastic progression identified in biopsies are difficult to apply in exfoliated samples because of their heterogeneous nature; abnormal cells comprise a very small portion of the total and the contribution of local inflammatory cells can be hidden by bleeding during sample collection. False-negative rates are greatest when abnormal cervical cells are a small proportion of total cells. Misinterpreted cervical cytology ranks third among causes of medical negligence claims against pathologist. The assay platforms that are not affected by dilution require a large amount of time and

expertise to screen for the rare neoplastic cells. Cervical cancer screening would greatly benefit from enrichment of abnormal cells.

There are some limitations for current cell enrichment technologies. Standard techniques such as FACS (fluorescence activated cell sorter) have been developed for cell enrichment (Bonner et al., 1972). They need much labor and 'tags' are required to identify cells of interest (Toner et al., 2005). Moreover, their high costs, usually about $250,000, limit their broader adoption (Gossett et al., 2010). Microfluidic chips use a small amount of cell samples, and can carry out enrichment and manipulation based on physical biomarkers of cells. These biomarkers include size, density, shape, elasticity and polarization (Jacobson et al., 1999, Huang et al., 2004, Davis et al., 2006, Whitesides et al. 2006, Balvin et al., 2009, Loutherback et al., 2009). Manipulations can be done on cells based on the polarization by non-uniform electric fields (Gadish et al., 2006, Voldman et al., 2006, Hunt et al., 2008, Tornay et al., 2008, Park et al., 2009), however, this method may polarize the cell membrane and disrupt normal metabolic function (Vernhes et al., 1999, Muller et al., 2003, Voldman et al., 2006). Optical tweezers exert force on cells with a laser beam (Grier et al., 2003), but this method can only be used to manipulate a single cell at a time and may over-heat the cell body, rendering it denatured. Compared with the method mentioned above, magnetic bead manipulation is a practical alternative (Pamme et al., 2004, 2006, Rida et al., 2004, Lee et al., 2007, Liu et al., 2009). The downside of this is that it is manually-intensive and time-consuming. The scaling up of this method is difficult (Hafeli et al., 1997, Miller et al., 2001, Rife et al., 2003, Mihajlovic et al., 2007, Shevkoplyas et al., 2007) because the magnetic moments of these beads often vary due to the manufacturing procedure. Automation-assisted cytology is no

better or even less sensitive than manual reading (Nieminen et al., 2005, Kitchener et al., 2011, Anttila et al., 2011).

To overcome the limits of current cell enrichment technologies, in this project, we aim to develop a fully integrated ferrofluidic microchip to magnetically manipulate and enrich cells inside bio-compatible ferrofluids in a label-free manner by combining microfluidics and dynamically-reconfigurable wire-mesh coils. We will test the chip with non-magnetic particles varying in size, shape and elasticity.

1.1.2 Ferrofluids

Ferrofluids are stable colloidal suspensions of permanently magnetized nanoparticles in a carrier liquid like water or oil. Each particle is typically made from magnetite (Fe_3O_4) coated with a monolayer of surfactant to prevent the particles from agglomerating under van der Waals attraction forces. Furthermore, the ~10 nanometer particle diameter is small enough to ensure that the particles remain dispersed by Brownian motion and do not agglomerate under gravity and magnetic interactions (Rosensweig et al., 1985, Odenbach et al., 2009, 2002). Therefore, ferrofluids are stable suspensions that exhibit superparamagnetic susceptibilities with suspended magnetic particles constituting typically up to 10% of the total fluid volume.

Ferrofluids exhibit a rich set of flow patterns and instabilities in the presence of DC, AC and rotating magnetic fields. Magnetic-field-based micro-electromechanical (MEMS) and nano-electromechanical system (NEMS) that use ferrofluids offer a potentially more reliable and compact alternative technology to existing electric-field-based devices.

Particle manipulation in microfluidic devices has drawn a lot of attention recently

(Li et al., 2002, Toner et al., 2005, Easley et al., 2006, Nagrath et al., 2007, Cho et al,. 2007, Pamme et al., 2007, Tsutsui et al., 2009, Yung et al., 2009). By applying a magnetic buoyancy force to microparticles inside ferrofluids, it becomes possible to manipulate the particles. Microparticles in ferrofluids experience a force which is proportional to their volume and which also depends on the shape and elasticity of the particle in a nonlinear manner. In order to achieve fast cell manipulation in a microfluidic environment, approximately tens of picoNewtons (pN) force needs to be exerted on a micron-sized particle, which can be achieved with a moderate (~100 mT) magnetic field (Zhu et al., 2010, 2011). It has been demonstrated that an integrated electrode-based microfluidic platform can be used for controlled sorting of cells within a ferrofluids based on their size, shape and elasticity in static flow conditions (Kose et al., 2009). For example, it is possible to separate red blood cells from E. coli bacteria with 94% efficiency on the basis of size differences (Kose et al., 2009). Kose et al. (2009) were also able to separate normal red blood cells from sickle cells using their shape and elasticity differences with 75% efficiency. Zhu et al. (2010) developed another separation scheme based on size only in a microfluidic device incorporating a simple hand-held permanent magnet. This device had a higher efficiency, higher throughput and continuous flow compared to Kose's work. In Zhu's experiment, particles with 1 μm diameter and 9.9 μm diameter, respectively, were observed to flow together before the application of a non-uniform magnetic field, as shown in Figure 1a. Once a magnetic field was applied, magnetic buoyancy forces deflected the particles from their flow paths, as shown in Figure 1d, resulting in the spatial separation of particles. Zhu et al. were able to separate ~105 9.9 μm particles from ~105 1 μm particles per hour with the a flow rates of 3 μl/min.

Separation throughput can be further increased by tuning the experimental parameters (increasing the flow rates of the particles/ferrofluids mixture and magnetic field strength, gradient) (Zhu, 2010). Separation 3.1 μm diameter and 9.9 μm diameter particles was also achieved as shown in Figure 1, and 97.2 – 100% separation efficiency was reached.

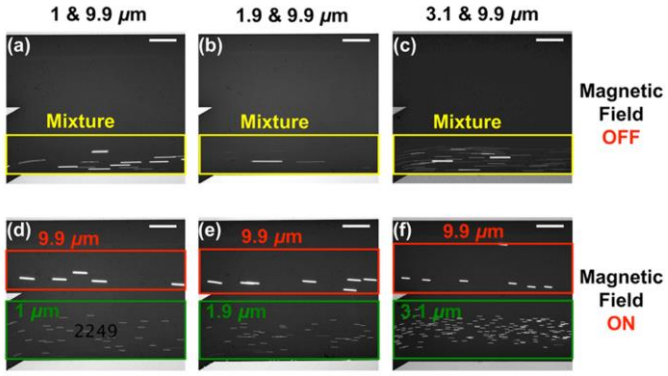

Figure 1: Images of particles separation. (a) – (c) Images before magnetic field is applied; (d) – (f) Images after the magnetic field is applied. Scale bar is 300 μm. Cited from Zhu T. 2010).

In a typical method, ferrofluids were synthesized by chemical co-precipitation. Then nanoparticles were coated with surfactant (PEG). In Zhu's experiment, a commercially-available water-based magnetic ferrofluids (EMG 408) was used. The volume fraction of the magnetite particles for this particular ferrofluids is 1.1%. The mean diameter of nano magnetic particles has been determined from transmission electron microscopy (TEM) images to be 10.2 nm with a standard deviation of 1.25 nm.

1.2 Research Objective

The research described here is part of a larger project, aimed at developing a low-cost microfluidic chip for cell enrichment and manipulation. The proposed system uses water based bio-compatible ferrofluids as a uniform magnetic environment that surrounds the non-magnetic (cancer) cells within a set of microfluidic channels and reservoirs. By

applying an external magnetic field, the non-magnetic objects can be pushed away, and these objects (including cancer cells) can be potentially trapped, manipulated and directed towards a specific location. Key to this system is the ability to deliver dynamically-reconfigurable magnetic field patterns, and the objective of the research described here is to develop a system to produce such fields.

The objectives of my research are:

1. Develop a dynamically-reconfigurable wire-mesh coil capable of delivering magnetic fields of sufficient strengths to manipulate suspended (micro) objects.
    a. The initial design will be based on a rectangular mesh of wires. Each wire is 100 μm in width, 5 mm in length and 30 μm in thickness. A combination of simulation and bench experiments will be conducted to arrive at the final design. We will need approximately tens of piconewtons force to manipulate the micron-sized particles.
    b. If necessary, a method to dissipate excessive heat will be designed.
2. Develop the electronic circuitry and software control system of dynamically alter the magnetic field in a pre-determined order.
3. Test the system. Initial testing will be done with magnetic micro particles of various sizes suspended in water. These particles must be moved successfully to specified locations in a reservoir with a resolution of 1000 μm, which is the distance between two neighboring wires, and kept there for a given amount of time.

1.3 Research Significance

This project develops a ferrofluidic microchip as a general cell manipulation

platform for biomedical research. It will achieve a low-coat front-end separation mechanism to enrich cervical abnormal cells for increased reproducibility reduced screening time, and improved screening accuracy.

The novelty of the project is the application of a versatile wire-mesh coil which is capable of delivering different patterns of magnetic fields in multiple sites in any temporal order.

1.4 Dissertation Outline

Chapter 2 presents a review of previous work done on non-magnetic particle manipulation by electric field and magnetic field caused by permanent magnets. Chapter 3 presents the basic idea of our wire-mesh coil micro-fluidic device, the problems we will encounter and how to solve them and the implementation of the device. Chapter 4 presents the bench experiments to test the performance of the proposed device. Results of the experiments will be discussed based on each of the objectives mentioned in Chapter 3. Chapter 5 summarizes the experiment results and the major findings of this study, also contains suggestions for future research.

Chapter 2 Literature Review

This chapter reviews the literature pertinent to cell enrichment technologies. Some typical existing methods and their limitations are discussed. The recently developed microfluidic chip for efficient particle and droplet manipulation with dielectophoresis is also presented. Alternative electric field tends to polarize cells' membrane, to settle this problem, cell manipulation methods based on non-uniform magnetic fields have been developed.

2.1 Review of Current Cell Enrichment Technologies

Existing cytology screening methods require expensive infrastructure and highly-trained cytotechnologists, which limit their application in low resource settings with the highest burden of disease (Kitchener et al., 2006) . The sensitivity of screening has been increased by high-risk human papillomavirus (HR-HPV) testing, but specificity remains relatively low, especially among younger women with high HPV prevalence (Mayrand, 2007). Recently developed prophylactic HPV vaccines has promise to solve the problem, but its high cost hampered its implementation (Cronje, 2004). Therefore, easy to use objective screening tests are needed to improve the efficiency of cell screening (Massad, 2009). Since abnormal cells comprise (Cronje, 2004)e a very small portion of the total, cancer cell screening would greatly benefit from enrichment of abnormal cells. As mentioned in Chapter 1, current cell enrichment technologies cannot be widely adopted because of their limitations.

Magnetic bead manipulation is a practical alternative to the method mentioned above. (Rida, 2004, Pamme. 2004, 2006, Lee, 2007, Liu, 2009) The downside of this is

that it is manually intensive and time-consuming. Further more, the scaling of this method is difficult (Hafeli, 1997, Rife, 2003, Miller, 2001, Mihajlovic, 2007, Shevkoplyas, 2007) because the magnetic moments of these beads often vary due to the manufacturing procedure. Automation-assisted cytology is no better or even less sensitive than manual reading (Nieminen, 2005, Kitchener, 2011, Anttila, 2011).

2.2 Hybrid Integrated Circuits and Microfluidics

Automated handling of fluid and biological samples has played an important role in cell sorting and biomedical studies (Tabeling, 2005). The demand of manipulating increasingly large sets of diminishingly small objects calls for miniaturization and automation of the system (Lee et al., 2007). Dielectrophoresis (DEP) has been used to manipulate nano-particles, viruses and single molecules (Green et al., 1997). The Westervelt Group at Harvard University has developed coaxial and triaxial atomic force microscopy (AFM) probes that create strong localized electric fields at their tip (Westervelt et al., 2011). These probes can be used to image and manipulate materials with dielectrophoresis. Many applications have been developed with the combination of integrated circuit and microfluidics (Westervelt K. B., 2011) such as systems for magnetic manipulation, recording and stimulating electrogenic cells, dielectric manipulation and sensing and DNA detection. The Westervelt Group at Harvard University has also presented an integrated circuit/ microfluidid chip that traps and moves individual living biological sells and chemical droplets along programmable paths using dielectrophoresis (DEP) (Caspar et al., 2012), a 320 x 320 array of electrodes was implemented, with each electrode 20 x 20 mm in size, to dynamically generate an electric field. Electric field gradients were created by applying an actuation voltage of up to 5 V

between neighboring electrodes. Particles in the microfluidic channel were exposed to a maximum electric field of around 50 kV/m. Thomas et al. achieved manipulation of droplets and yeast at speed up to 30 mm/s.. However, the alternating electric fields tend to polarize the cells' membrane and disrupt normal metabolism function (Voldman et al., 2006, Vernhes et al., 1999, Muller et al., 2003). As a result, magnetic buoyancy force is a better method for cell manipulation.

2.3 Separation of Non-magnetic Particles Inside Ferrofluids

When a non-uniform magnetic field is applied to ferrofluids, a magnetic pressure distribution is created in the ferrofluids. The fluid will act as if its density is variable with height. This phenomenon forms the foundation of the magnetic-hydrostatic separation of ores (Rosensweig 1985; Rosenweig et al. 1987). Particle sorting based on magnetic buoyancy force has multiple advantages including high throughput and high accuracy. Manipulation of synthetic microparticles has been realized inside ferrofluids through magnetic buoyancy force (Kose et al., 2009). Motion of non-magnetic particles inside ferrofluids is dominated by the magnetic buoyancy force and the hydrodynamic drag force. Based on this, a series of techniques have been developed to manipulate particles based on their intrinsic physical properties (e.g., size, shape, density) in microfluidic devices (Gossett et al., 2010). These label-free microfluidic techniques are sometimes preferred over conventional ones such as the fluorescence-activated cell sorter (FACS) (Bonner et al., 1972) and the magnetically-activated cell sorter (MACS) (Miltenyi et al., 1990) because they are cost-effective and do not require much user training for operation. A label-free continuous flow non-magnetic particle separation scheme in a microfluidic device under static magnetic fields has been presented by Zhu et al. (2010). An analytical

model of the transport of non-magnetic spherical micro-particles in ferrofluids in a microchannel using a permanent magnet has been designed by Zhu et al. (2011) and experimentally verified (Zhu et al., 2010). It was demonstrated that the force on a micro-particle under a moderate magnetic field (~100 mT) is in the order of tens of piconewtons (pN), which is sufficient for effective cell manipulation in a microfluidic environment. Zhu et al. also demonstrated an on-chip microparticle focusing technique using stable magnetic nanoparticles suspensions (ferrofluids) in 2011. The principle of focusing is based on magnetic buoyancy forces exerted on non-magnetic particles within ferrofluids under a non-uniform magnetic field. Most current technologies to deliver magnetic fields in microfluidic devices are focused on using arrays of electrodes (Gijs et al., 2010). A downside of this approach is that the electrode design lacks flexibility and the pattern of the magnetic field is usually unalterable. A two-dimensional wire-mesh coil can produce reconfigurable and dynamic magnetic fields, which would make the system versatile (Ruoli et al., 2013).

Chapter 3 Methods

3.1 Outline of the Device

The proposed micro particle manipulation device is composed of two parts: 1) a reconfigurable coil system capable of continuously generating magnetic fields, and 2) a chamber which contains the mixture of ferrofluids (magnetic nano particles) and non-magnetic micro particles. The basic idea of this device is to manipulate micro-particles by forces applied to them through externally-generated, time-varying magnetic fields. The magnetic field gradient thus obtained will exert a translational force on magnetic particles. In contrast, a uniform field would give rise to a torque, but no translational action. We envision that the magnetic fields are produced by a set of cross-wires under the container holding the particles suspended in a liquid. By varying the current flow through each cross-wire in a controlled manner, magnetic fields with desired gradient characteristics can be obtained resulting in the desired movement of the suspended particles. For example, sequentially applying a brief current pulse to a number of parallel cross-wire will result in a motion perpendicular to the cross-wires. Particles may be trapped by applying steady currents to two sets of neighboring *x*-directional and *y*-directional wires.

In order to effectively control the non-magnetic particles, the following problems need to be solved:

1) How large is the current required to generate enough force to move the non-magnetic particle? Non-magnetic particles should be accelerated to a given velocity in a short time interval (much shorter than the time it takes to move the

particle over 1 mm). The desired velocity will be decided based on the effectiveness and safety of the device.

2) The wire-mesh coil system should manipulate the particles with a resolution of 1 mm because adjacent wires are 1 mm apart from each other.
3) We need to analyze the heat generation of the wire, find a stimulus pattern that can move the particles effectively while preventing the wire from burning out. Also, the heat needs to remain small enough to keep the cells alive in practical use.

The solutions to these problems are discussed in the following sections.

3.1.1 Current Required to Generate Sufficient Forces on Non-magnetic Particles

When an external magnetic field is applied, the non-magnetic particles suspended in a ferrofluids experience both magnetic buoyancy and hydrodynamic drag forces, referred to as $\overrightarrow{F_m}$ and $\overrightarrow{F_d}$, respectively. In the case of diluted ferrofluids or when a non-uniform magnetic field is applied, as shown in Figure 2, a magnetic pressure distribution is created in the ferrofluids, resulting in the fluid acting as if it has variable density with height.

The magnetic buoyancy force on a non-magnetic particle inside ferrofluids can be expressed as (Rosensweig 1966) using

$$\overrightarrow{F_m} = -V\mu_0(\overrightarrow{M}\cdot\nabla)\overrightarrow{H}, \quad (1)$$

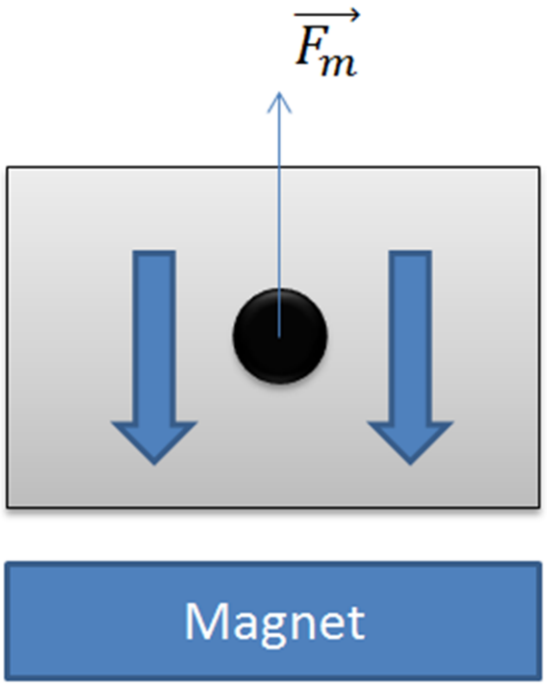

Figure 2: Schematic view of magnetic buoyancy force on non-magnetic particle caused by non-uniform magnetic field.

where V is the volume of the non-magnetic particle, μ_0 is the permeability of free space, $\overrightarrow{M}$ is the effective magnetization of ferrofluids, and $\overrightarrow{H}$ is the externally- applied magnetic field. The minus sign in front of the term indicates that the non-magnetic particles tend to move towards where the magnetic field is weaker. The ferrofluids used in our experiment are very diluted, therefore, we assume that the demagnetization field is small enough so that the effective magnetization $\overrightarrow{M}$ equals to the magnetization of ferrofluids $\overrightarrow{M_f}$.

Magnetization of ferrofluids varies with the magnetic field $\overrightarrow{H}$. When H is small, the ferrofluids is linearly magnetized by the field. When the magnetic field is high, the magnetization of the ferrofluids is saturated. A function describing the whole magnetized

region is called the Langevin curve, described by

$$\frac{M(H)}{\phi M_d} = L(\kappa) = \coth(\kappa) - \frac{1}{\kappa}, \tag{2}$$

where

$$\kappa = \frac{\mu_0 \pi M_d d^3 H}{6 k_B T}.$$

Here M_d (equal to 4.46×10^5 A/m) is the bulk magnetization of magnetic nanoparticles of diameter d (10 nm) suspended in carrier medium of ferrofluids with volume fraction ϕ (0.01). The Boltzmann constant is k_B and T is the temperature (in Kelvin). The value of the Bolzmann constant is

$$k_b = 1.38\times10^{-23} \text{ J/K}.$$

We assume room temperature during the experiment, i.e., $T = 293$ K. The magnetization of ferrofluids follows the graph shown in Figure 3.

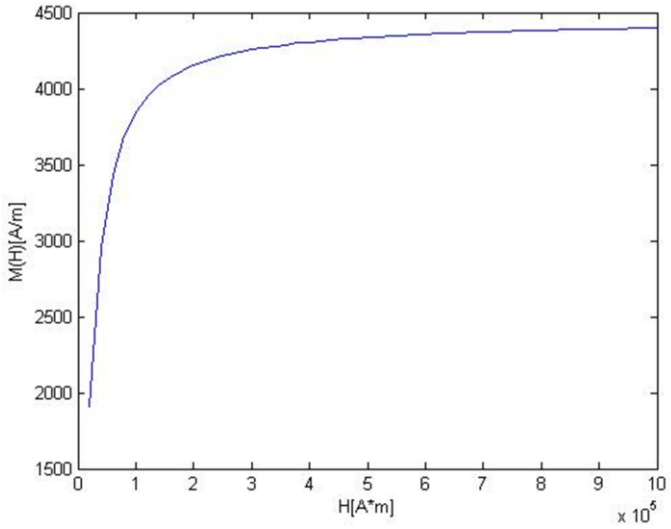

Figure 3: Langevin curve that describes the magnetization of ferrofluids. When the applied magnetic field is low, the curve rises approximately linearly, as H grows larger, the curve becomes flat and tends to saturate.

In our project, the applied magnetic field is relatively small and falls into the linear region of the Langevin curve. Magnetization of ferrofluids $\overrightarrow{M_f}$ is related to the external magnetic field $\overrightarrow{H}$ by the magnetic susceptibility χ_m, which is a dimensionless property determined by the material. According to the linear part of the curve in Figure 3, magnetic susceptibility of ferrofluids χ_m is around 0.05. As discussed above, we can assume that the effective magnetization of ferrofluids rises linearly with the external applied magnetic field. The linear approximation of effective magnetization is given by

$$\overrightarrow{M_f} = \frac{\vec{B}}{\mu_0} - \overrightarrow{H} = (\mu_r - 1)\overrightarrow{H} = \chi_m \overrightarrow{H} \quad . \tag{3}$$

The magnetic buoyancy force on non-magnetic particles becomes

$$\overrightarrow{F_m} = -\frac{V\chi_m}{\mu_0 \mu_r^{\,2}} (\vec{B} \cdot \nabla)\vec{B} \, . \tag{4}$$

Considering non-magnetic particles that are constrained to move in a chamber in the *x*-*y* plane, both the magnitude of the magnetic field and the field gradient need to be large enough to exert a significant magnetic buoyance force. From Equation (4), we can obtain the expressions for the *x*, *y* and *z* components of the magnetic buoyancy force, resulting in

$$\begin{aligned} F_{m,x} &= -\frac{V\chi_m}{\mu_0 \mu_r^{\,2}} \left(B_x \frac{\partial}{\partial x} + B_y \frac{\partial}{\partial y} + B_z \frac{\partial}{\partial z}\right) B_x \\ F_{m,y} &= -\frac{V\chi_m}{\mu_0 \mu_r^{\,2}} \left(B_x \frac{\partial}{\partial x} + B_y \frac{\partial}{\partial y} + B_z \frac{\partial}{\partial z}\right) B_y \quad . \\ F_{m,z} &= -\frac{V\chi_m}{\mu_0 \mu_r^{\,2}} \left(B_x \frac{\partial}{\partial x} + B_y \frac{\partial}{\partial y} + B_z \frac{\partial}{\partial z}\right) B_z \end{aligned} \tag{5}$$

Assuming that a wire parallel to the chamber is conducting current *I*, as illustrated in Figure 4, and that the wire is oriented in the *y*-direction and generates a steady

magnetic field in the *x*-*z* plane, then thenon-magnetic micro particles in the chamber will be driven by a force in the *x* direction. The gradient of the magnetic field is zero along the *y* direction, so $F_{m,y}$=0. The non-magnetic particles also experience gravity and buoyancy forces in the *z*-direction. For micron-sized particles in ferrofluids, only the magnetic and viscous forces are dominant (Zhu et al., 2011).

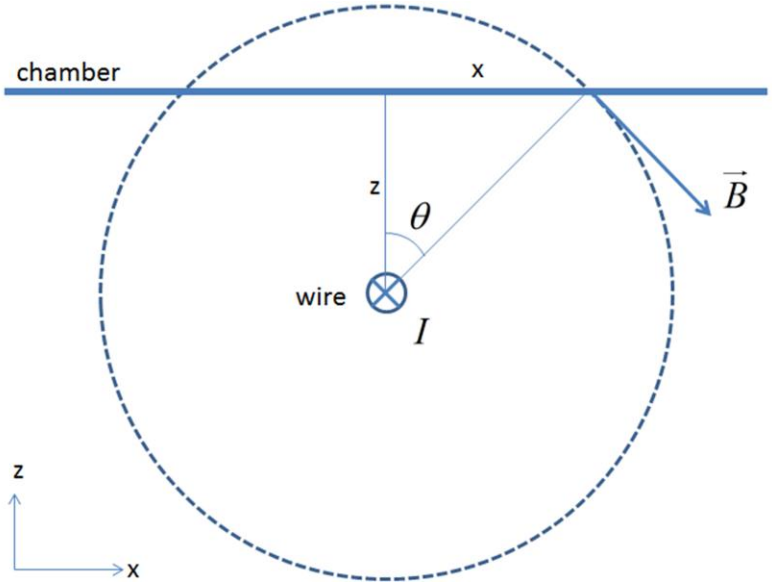

Figure 4: A wire conduction current *I* is placed below a chamber which is set in the *x*-*y* plane.

The magnetic field inside the ferrofluids depends on the magnetization of ferrofluids and the geometry of the chamber. The ferrofluids will not be uniformly magnetized in response to the non-uniform magnetic field generated by the single wire. As a result, there is no analytical solution to the magnetic field in the chamber. However, the ferrofluid is a diluted suspension of ferromagnetic particles and its magnetic susceptibility is relatively small (χ_m =0.05). For qualitative analysis, we use the magnetic field in vacuum to approximate the magnetic field in ferrofluids. This approximation will introduce errors, and we will compare our calculations with the simulation results

obtained through the finite element method. From Figure 4, and assuming a vacuum medium, we have

$$B_x = \left|\vec{B}\right| \cos\theta = \frac{\mu_0 I}{2\pi} \frac{z}{x^2 + z^2}$$
$$B_y = 0$$
$$B_z = -\left|\vec{B}\right| \sin\theta = -\frac{\mu_0 I}{2\pi} \frac{x}{x^2 + z^2}$$

$$\frac{\partial B_x}{\partial x} = -\frac{\mu_0 I}{2\pi} \frac{2xz}{(x^2 + z^2)^2}$$
$$\frac{\partial B_x}{\partial y} = 0$$
$$\frac{\partial B_x}{\partial z} = \frac{\mu_0 I}{2\pi} \frac{x^2 - z^2}{(x^2 + z^2)^2}$$
$$\frac{\partial B_z}{\partial x} = \frac{\mu_0 I}{2\pi} \frac{z^2 - x^2}{(x^2 + z^2)^2}$$
$$\frac{\partial B_z}{\partial y} = 0$$
$$\frac{\partial B_z}{\partial z} = \frac{\mu_0 I}{2\pi} \frac{2xz}{(x^2 + z^2)^2} .$$

The x component of the magnetic buoyancy force becomes

$$F_{m,x} = \frac{V \chi_m I^2 \mu_0}{4\pi^2 \mu_r{}^2} \frac{x^3 + xz^2}{(x^2 + z^2)^3}$$
$$F_{m,z} = \frac{V \chi_m I^2 \mu_0}{4\pi^2 \mu_r{}^2} \frac{z^3 + x^2 z}{(x^2 + z^2)^3} . \quad (6)$$

The position of the chamber is fixed, so that z can be treated as a constant. $F_{m,x}$ is an odd function of x and $F_{m,z}$ is an even function of x. In the proposed wire-mesh design, the distance between adjacent wires is 1 mm.

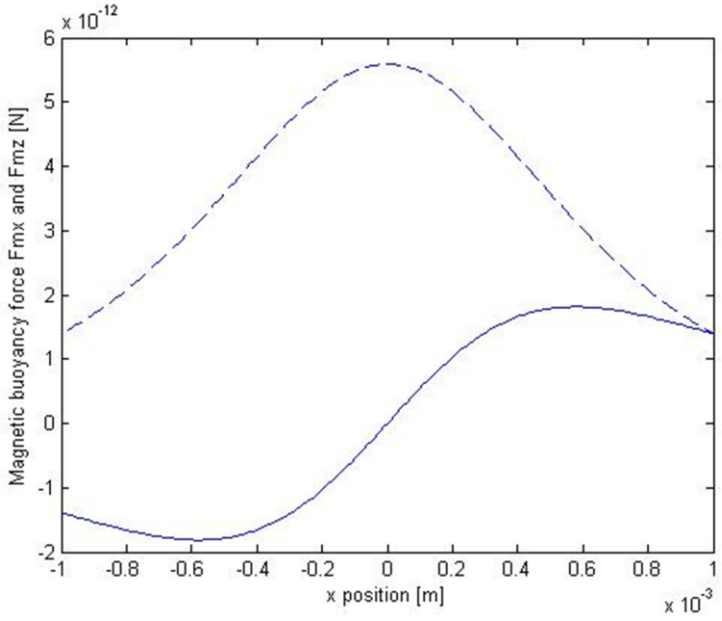

z = 1 mm

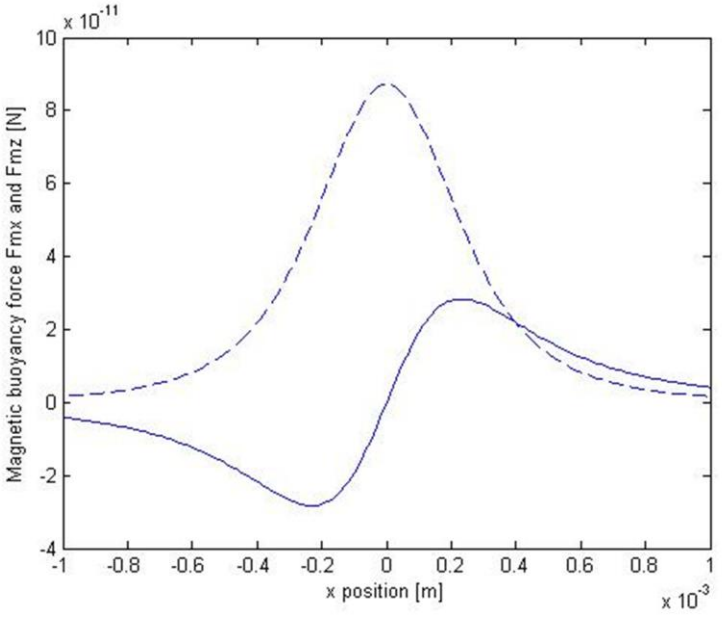

z = 400 μm

Figure 5: The *x*-directional and *z*-directional magnetic buoyancy force on 15.7 μm non-magnetic particles, depicted by solid and dashed line respectively. Range from -1 mm to 1 mm. Current in the single wire is set to be 30 A.

Figure 5 shows the *x* and *z* directional magnetic buoyancy forces on a non-

magnetic particle. The location $x = 0$ on the horizontal axis marks the spot where a single, current-carrying wire is located under the chamber. Since $F_{m,x}$ is an odd function of x and thus negative for $x<0$, the non-magnetic particles will be driven to the left, while for $x > 0$, the particles will be driven to the right. For particles close to $x = 0$, the magnetic buoyance force will approach zero. In this case, we need to send current to an adjacent wire to get sufficient force. $F_{m,z}$ is a positive even function of x, which implies that the non-magnetic particles will always experience an upward magnetic buoyancy force.

Movements of particles in a fluid will cause a hydrodynamic drag force, which tends to hinder the motion, and is given by

$$\overrightarrow{F_d} = -6\pi\eta r\vec{v}, \tag{7}$$

where η is the dynamic viscosity of the surrounding fluid and r is the radius of the particle. The speed of the bead relative to the surrounding fluid (assumed to be static) is given by $\vec{v}$. Movement of non-magnetic particles in the ferrofluids is dominated by magnetic buoyance force and hydrodynamic drag force, which can be represented by

$$\frac{d\vec{v}}{dt}m = \overrightarrow{F_m} + \overrightarrow{F_d}. \tag{8}$$

Equation (8) is a differential equation of relative velocity $\vec{v}$. The particle has reached maximum velocity $\overrightarrow{v_m}$ when

$$\overrightarrow{F_m} + \overrightarrow{F_d} = 0. \tag{9}$$

Substituting the top part of Equation (6) and Equation (7) into Equation (9), the current needed to drive the non-magnetic particle to such velocity is obtained as

$$I = \sqrt{\frac{18 v_m \pi^2 \eta}{r^2 \chi_m \mu_0 \frac{x^3 + 3xz^2}{(x^2 + z^2)^3}}} . \quad (10)$$

Manipulating non-magnetic particles efficiently requires rapid particle movement. As indicated by Equation (10), the maximum velocity v_m is proportional to the square of current I, but using a large current means more heat generation and power consumption, potentially killing the cells to be manipulated. We need to draw a balance between these two aspects. Thomas et al. (2007) presented an integrated circuit/ microfluidic chip that traps and moves individual living biological sells and chemical droplets along programmable paths using dielectrophoresis (DEP). They have been able to move yeast and mammalian cells through a microfluidic chamber at speeds up to 30 μm/s. Yeast cells typically measure 3-4 μm in diameter, which is about 5 times smaller than the non-magnetic particles in our experiment (15 μm in diameter). Based on this, we propose to move the non-magnetic particles with top speed v_m = 50 μm/s. Assuming that the non-magnetic particles move with uniform speed during the current conduction period (the acceleration and deceleration of non-magnetic particles in response to externally applied magnetic fields will be discussed later), it will take 20 s to move particles 1 mm. . According to Equation (10), the current required to accelerate non-magnetic particles to such a speed is I = 30.3 A.

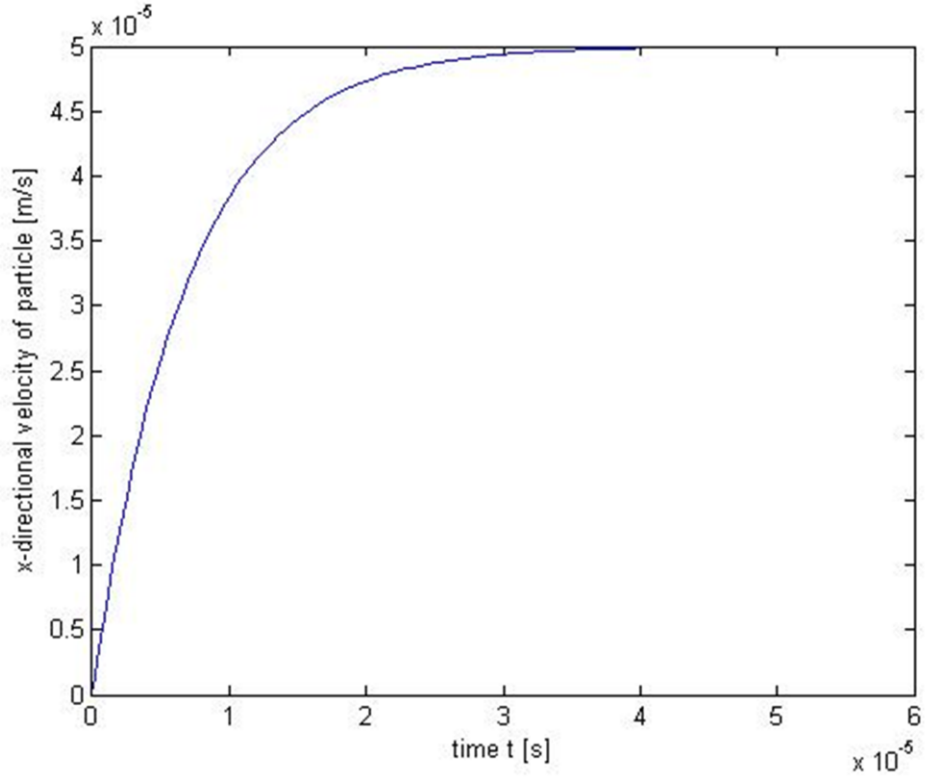

Figure 6: Acceleration of 15.7 μm non-magnetic particles, x = -500 μm, z = 400 μm.

According to Figure 6, the non-magnetic particle, starting from zero motion, reaches its maximum speed V_m = 50 μm/s in about 0.03 ms, which is far shorter than 1s. As long as the current is on, the non-magnetic particle will keep moving with speed V_m. When the current is off, the particle will decelerate due to the fluid drag force $\overrightarrow{F_d}$ and finally settle down. This procedure can be described by

$$\overrightarrow{F_d} = m\frac{d\vec{v}}{dt} \quad \text{and} \tag{11}$$

$$-6\pi\eta r\vec{v} = m\frac{d\vec{v}}{dt} \quad . \tag{12}$$

Solving this differential equation by assuming v_m = 50 μm/s as initial condition,

we get

$$v = 5\times10^{-5} e^{-\frac{6\pi\eta r}{m}t} \tag{13}$$

which is graphed in Figure 7.

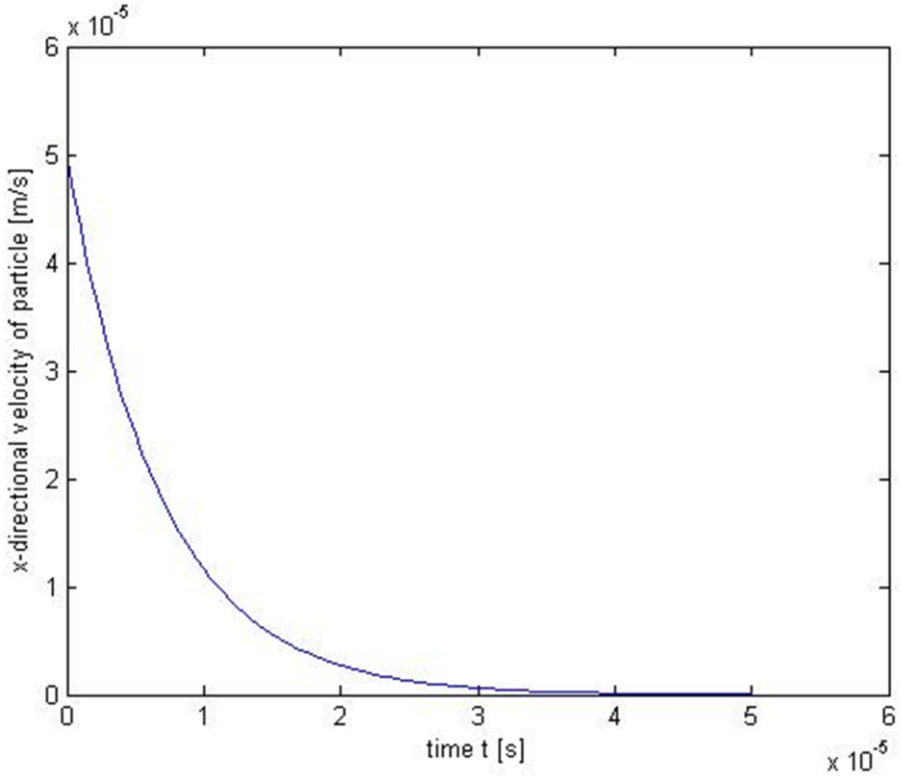

Figure 7: Deceleration of a non-magnetic particle after the current is turned off.

The deceleration procedure takes about 0.03 ms, and the motion of the non-magnetic particle during this phase is negligible. As a result, the motion of micro non-magnetic particles in ferrofluids can be treated as uniform motion. Inertial effects can be neglected and Stoke's flow equations dominate hydrodynamics.

A particle with velocity 50 μm/s, takes 20 second to move 1 'pixel' (i.e., the distance between two adjacent wires). Applying this speed to Equation (10), and assuming that the chamber is 400 μm apart from the wire-mesh coil (z = 400 μm), and x

= -0.5 mm (i.e., the horizontal position of the non-magnetic particle is right in the middle between two adjacent single wires), the current required to accelerate the non-magnetic particle to the proposed speed is $I = 30.3$ A.

COMSOL multi-physics was used to simulate the motion of non-magnetic particles in ferrofluids in response to an external magnetic field and to numerically calculate the magnetic field distribution inside the ferrofluids. The simulation will take the non-uniform magnetization of ferrofluids into consideration and will be more accurate than the theoretical calculations presented earlier. The particle tracing module in Comsol provides a Lagrangian solution of a problem by solving ordinary differential equations using Newton's law of motion and computes the trajectories of particles through a geometry, where geometry refers to an area with specific shape and physical characteristic used for finite element analysis. The forces acting on particles are divided into two categories; those due to external fields and those due to interactions between particles. Forces due to external fields are computed from a finite element model. In our simulation, the magnetic field distribution generated by the wire-mesh coil is determined in the first step. Next, the magnetic buoyancy forces exerted on non-magnetic particles by the magnetic field are obtained. As those particles start to move, their motion is hampered by the fluidic drag force, which is determined by the viscosity of ferrofluids.

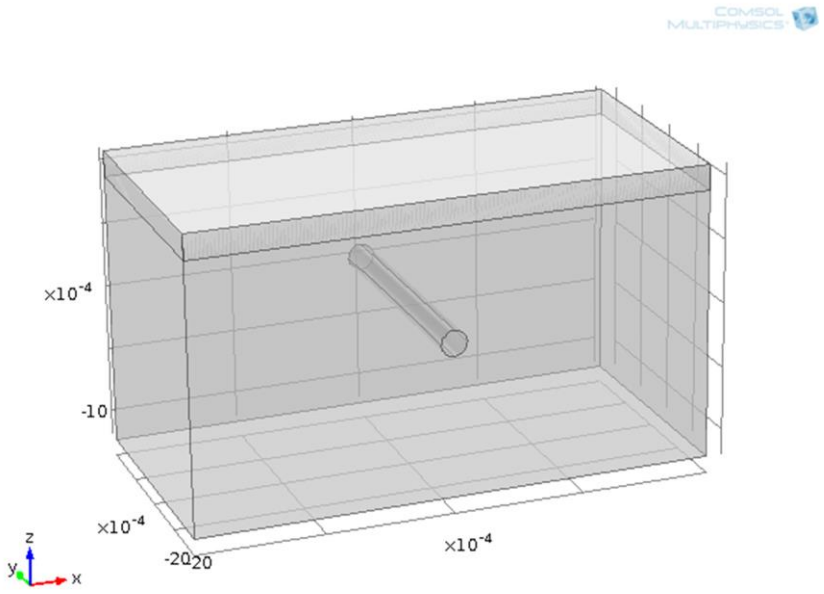

Figure 8: Geometry of simulation for the motion of non-magnetic particles. The thin box on the top is the chamber filled with ferrofluids and non-magnetic particles to be manipulated.

The simulation model is shown in Figure 8. The *y*-directional cylinder is a segment of copper wire, conducting a 30 A steady current. The remaining area is filled with air. The chamber is placed 1 mm above the copper wire. The width (*x* direction) of the model is 4 mm, so that we are simulating the motion of non-magnetic particles within ± 2 mm of the copper wire. Assuming that the copper wire is long, we can just simulate a 2-D section in the *x*-*z* plane.

In the simulation, magnetic buoyancy force is defined by Equation (4), which is proportional to the gradient and the magnitude of the magnetic field. Figure 9 compares the *x*-directional magnetic buoyancy force in the chamber filled with ferrofluids obtained through the simulation and theory. We can see that the two have slightly different distributions, and that the peak value of the simulation result is about 3.4 times greater than that shown by the theoretical calculation.

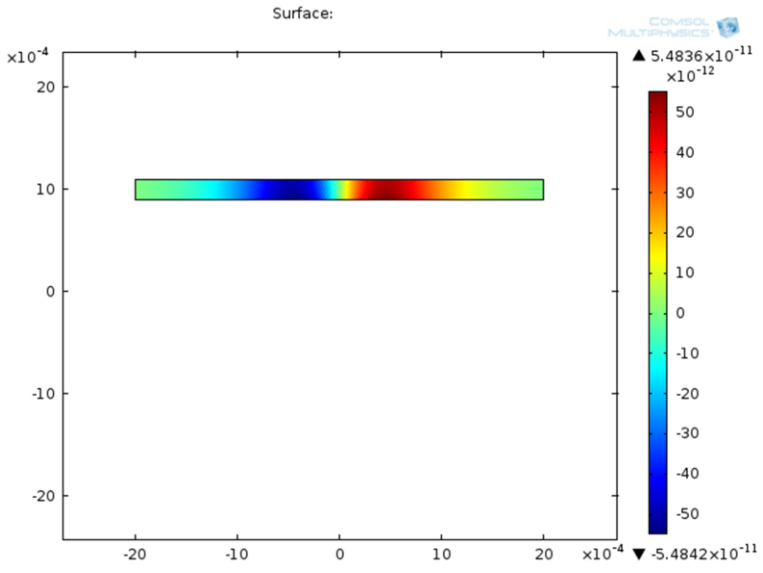

(a)

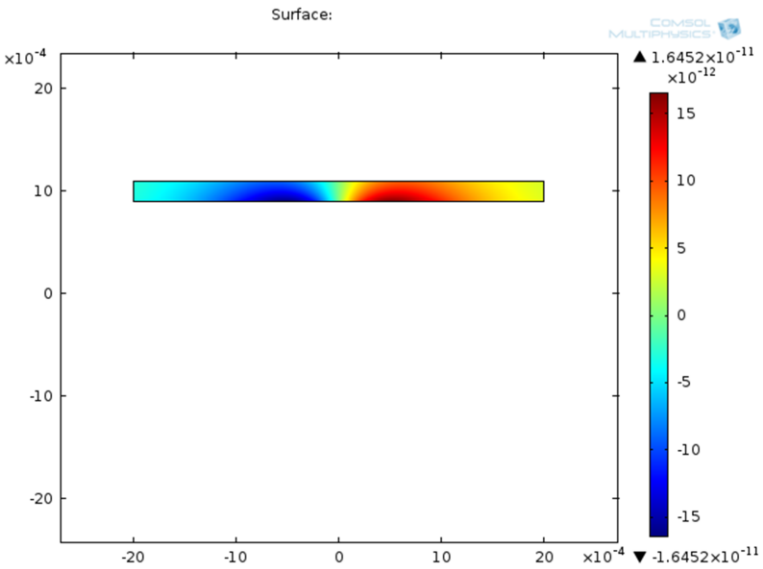

(b)

Figure 9: Distribution of *x*-directional magnetic buoyancy force in the chamber. Part (a) shows the simulation result, Part (b) is from the theoretical calculation.

Now that we have the magnetic buoyancy force distribution inside the chamber, we need to determine the fluid drag force exerted on non-magnetic particles as they move. We take the fluid drag on non-magnetic particles in ferrofluids to be the Stokes

drag

$$\overrightarrow{F_d} = -6\pi\eta r\vec{v}f_D, \tag{14}$$

where f_D is the hydrodynamic drag force coefficient. It indicates that the non-magnetic particles experience an increment in fluid viscosity as they move closer to the surface of the chamber (Ganatos et al., 1980; Krishnan and Leighton 1995; Staben et al., 2003). The factor f_D is expressed by Equation (15):

$$f_D = [1 - 0.6526(\frac{r}{r+z}) + 0.1475(\frac{r}{r+z})^3 - 0.131(\frac{r}{r+z})^4 - 0.0644(\frac{r}{r+z})^5]^{-1}, \tag{15}$$

where z is the distance between the bottom of the particle and the channel surface.

A time-dependent simulation was conducted to track the motion of non-magnetic particles in ferrofluids. At time t = 0, 1208 non-magnetic particles were uniformly dispersed in the ferrofluids. Their initial velocity was zero and they started to move due to the magnetic buoyancy force and fluid drag force. Figure 10 shows the magnetic buoyancy force versus the x-position, dashed curve depicts the theoretical analysis result, solid curve is for COMSOL simulation result, dashed curve shows the mathematically calculated magnetic buoyancy force described by Equation (6). The distance between the chamber and the wire was set to be 400 μm, with a single copper wire at position x = 0 conducting a steady current of 30.3 Amps. The magnetic field distribution caused by the current flow has been simulated and plotted. The magnetic buoyancy force was calculated based on the magnetic field inside the chamber.

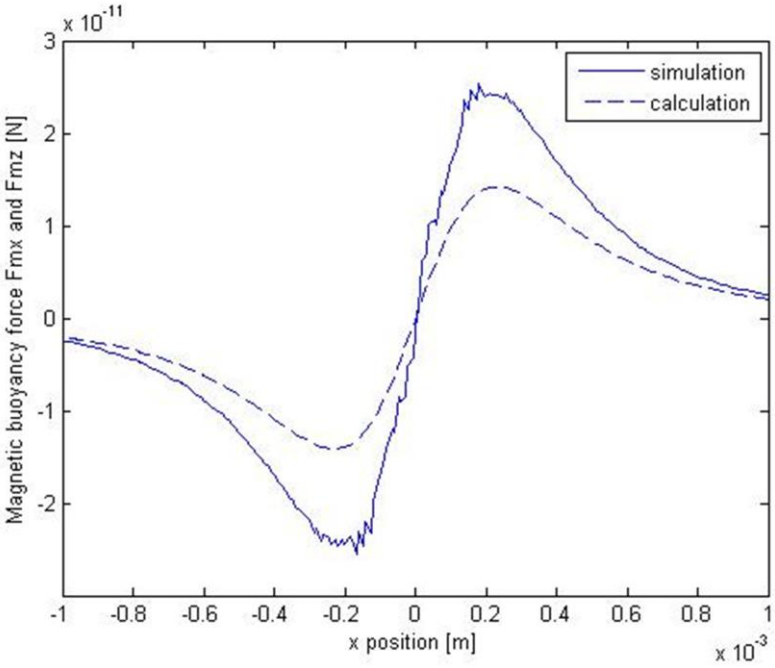

Figure 10: Comparison between the simulation result and theoretic calculation of the *x*-directional magnetic buoyancy force generated by a single wire conducting a 30.3 Amps current.

The two curves are similar in shape, but the magnitude of the simulation result is about 1.9 time greater than that obtained from theoretical analysis. The simulation result is closer to reality because the non-uniform magnetization of ferrofluids, which helps to increase the magnetic buoyancy force, in response to externally applied magnetic field has no analytical solution, and was not considered in our theoretical calculations. In contrast, the finite element analysis has taken the non-uniform magnetization of ferrofluids into account.

We simulated the motion of the non-magnetic particles from 0 to 10 s with COMSOL Multi-physics, with Figure 11 depicting the motion of non-magnetic particles at time 0s, 2s, 4s, 6s, 8s and 10s.

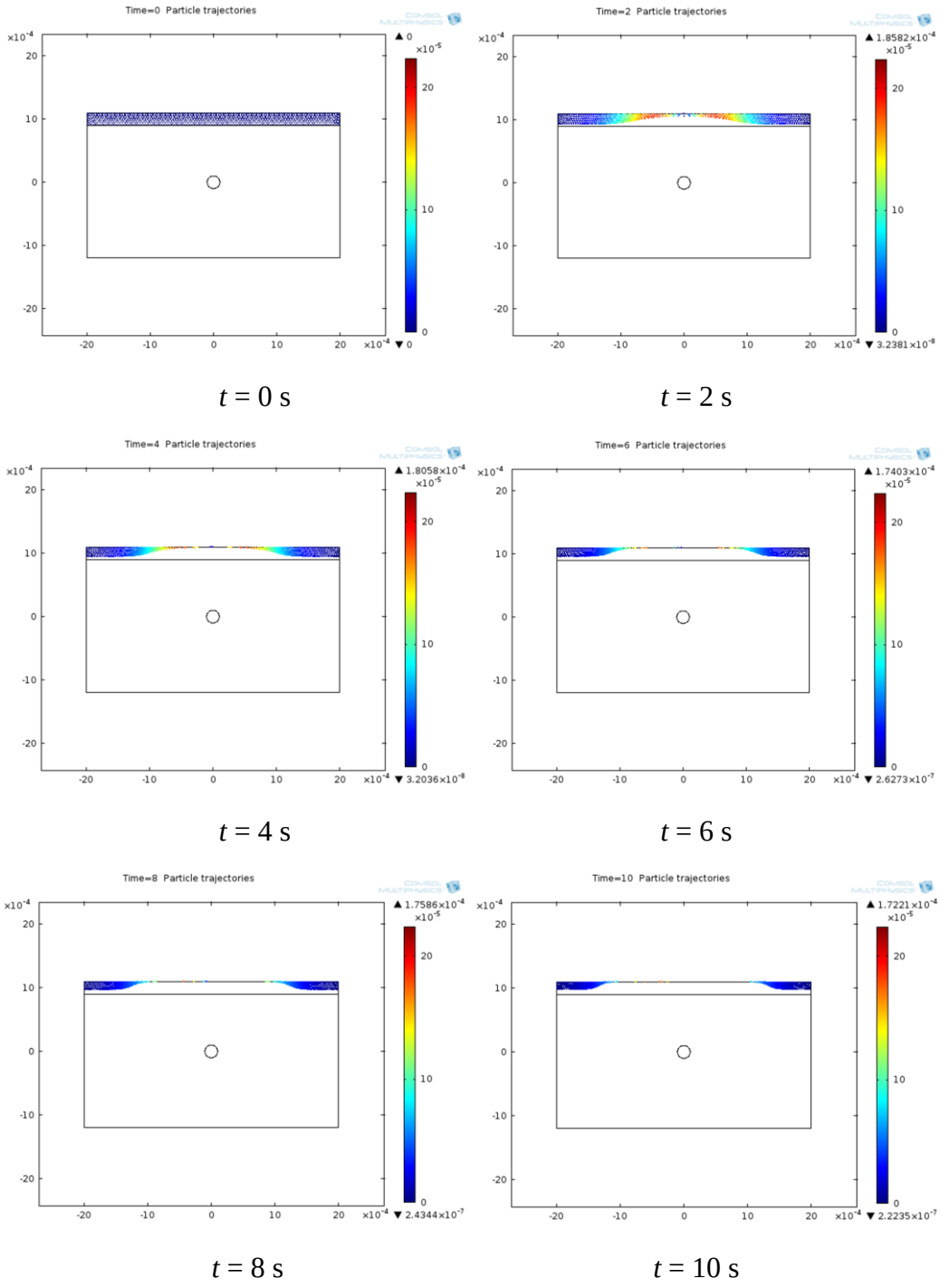

t = 0 s t = 2 s

t = 4 s t = 6 s

t = 8 s t = 10 s

Figure 11: Distribution of non-magnetic particles over 10 seconds. The motion of non-magnetic particles at 0s, 2s, 4s, 6s, 8s and 10s is shown.

We can see that the particles are horizontally pushed away from the copper wire

as intended. The particles have also been pushed to the top of the chamber, making them more easily observable from the top. The peak value of the *x*-directional velocity of the particles is around 170 μm/s, which is more than three times faster than our expectation. This can be explained by Figure 10, where the simulation result shows a greater magnetic buoyancy force due to the non-uniform magnetization of ferrofluids. As a result, less current is needed to achieve the 50 μm/s velocity of non-magnetic particles.

Figure 12 shows the displacement of each non-magnetic particle in the *x* direction over 10 seconds. The *x* axis shows the initial *x*-directional position of the particle inside the chamber.

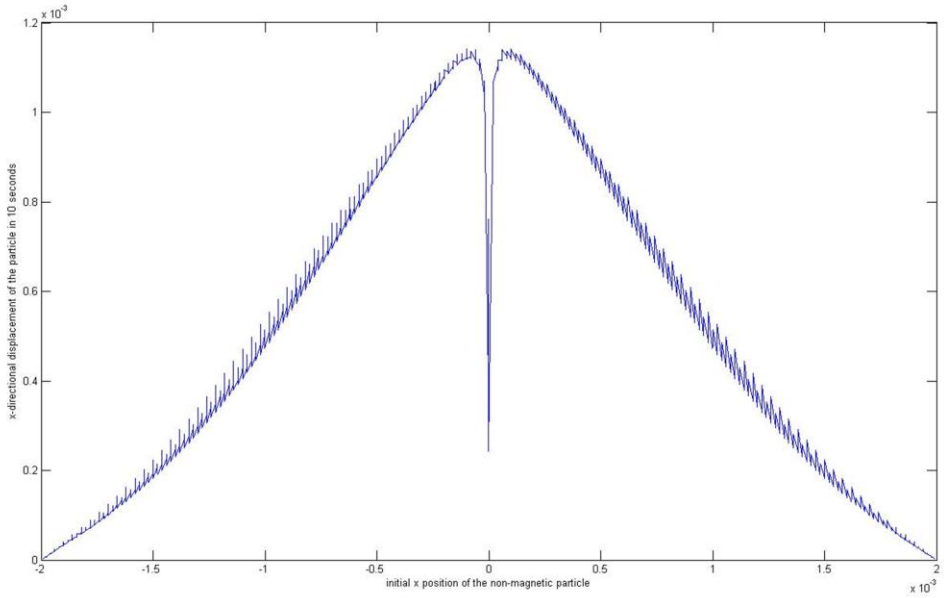

Figure 12: The *x*-directional displacements of the non-magnetic particles over 10 seconds.

In Figure 12, the displacement of particles near $x = 0$ is small because the *x*-direction of the magnetic field gradient is small there. For particles far from zero, the

displacement approaches zero because, for the simulation model, there are walls at $x = \pm 2mm$. The curve is not smooth because of the influence of the initial z position for each particle.

3.1.2 Resolution of Particle Manipulation

The wire-mesh coil system should manipulate the particles with a proper resolution. As discussed in Section 3.1.1, according to Equation (6), the magnetic buoyancy force is a function of horizontal position x and vertical position z. The magnetic buoyancy force generated by a single wire always tends to push the non-magnetic particle away from the wire. Non-magnetic particles right above the single wire experience no magnetic buoyancy force because the gradient of the magnetic field is zero there, in this case, we will need to send current to an adjacent wire to get sufficient force.

If two adjacent wires are conducting current simultaneously, the magnetic fields generated by these wires will superimpose and influence the motion of non-magnetic particles in ferrofluids. Consider the case shown in Figure 13, where two adjacent wires conduct current I simultaneously, with the wires located at $-x_0$ and x_0 along the x-axis, respectively. Conducting same direction current and opposite direction currents into the two parallel wires will result in different distributions of magnetic fields, which have different effects on particle motion.

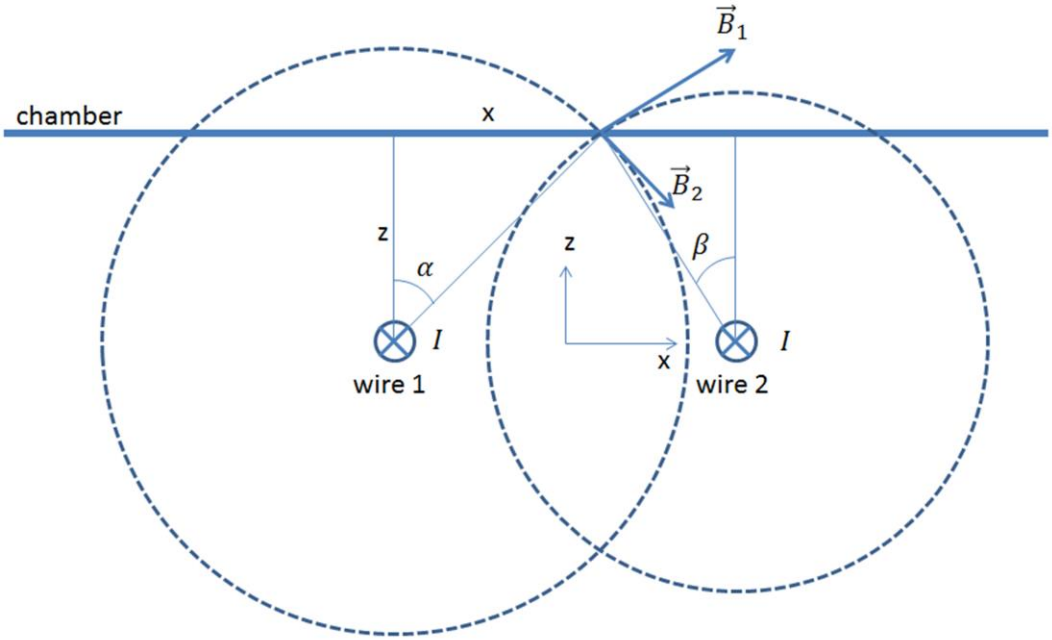

Figure 13: Two adjacent wires simultaneously conducting current *I*.

The magnetic field at a point in the chamber is the vector sum of the magnetic field generated by each wire, and since we are concerned about the *x*-directional magnetic field: $B_x = B_{x1} + B_{x2}$. The magnetic fields generated by the two wires are given by

$$B_{x1} = \left|\vec{B}\right| \cos\alpha = \frac{\mu I}{2\pi} \frac{z}{(x + x_0)^2 + z^2}$$
$$B_{y1} = 0$$
$$B_{z1} = -\left|\vec{B}\right| \sin\alpha = -\frac{\mu I}{2\pi} \frac{x + x_0}{(x + x_0)^2 + z^2}$$

$$B_{x2} = \left|\vec{B}\right| \cos\beta = \frac{\mu I}{2\pi} \frac{z}{(x - x_0)^2 + z^2}$$
$$B_{y2} = 0 \quad ,$$
$$B_{z2} = -\left|\vec{B}\right| \sin\beta = -\frac{\mu I}{2\pi} \frac{x - x_0}{(x - x_0)^2 + z^2}$$

where $\mu = \mu_0 \mu_r$ is the permeability of the ferrofluids. According to Equation (5), the *x*-directional magnetic buoyancy force is given by

$$F_{m,x} = -\frac{V\chi_m}{\mu_0 \mu_r^2}((B_{x1} + B_{x2})\frac{\partial(B_{x1} + B_{x2})}{\partial x} + (B_{z1} + B_{z2})\frac{\partial(B_{x1} + B_{x2})}{\partial z})$$

The motion of non-magnetic particles in response to two parallel currents also depends on the distance between the ferrofluids-filled chamber and the wires carrying the currents. The magnetic buoyance force for the case where the two adjacent wires conduct 30.3 A with opposite direction was simulated by COMSOL Multi-Physics and the results are shown in Figure 14. As shown in Figure 14, the magnitude of the magnetic buoyancy force is close to the case of a single wire (see Figure 10) for distances of 1 mm and 0.4 mm, and the non-magnetic particles within a range of -0.25 mm to 1.25 mm are driven to the center (x = 0.5 mm). Comparing the two parts of Figure 14, we can see that as the distance decreases, the magnetic buoyancy force increases. In Part (a) of Figure 14, the peak value of magnetic buoyancy force is around 5.2×10^{-12} N when distance z = 1 mm. While in Part (b), for z = 0.4 mm, the peak value of the magnetic buoyancy force is around 1.0×10^{-10} N, which is 19.23 times greater than that of the case for z = 1 mm. According to Equation (6), the magnetic buoyancy force is inversely proportional to the distance z. The cube of the distance ratio is 15.66. As a result, the simulation result fits the theoretical analysis. The configuration with two opposite parallel currents can be used for particle trapping.

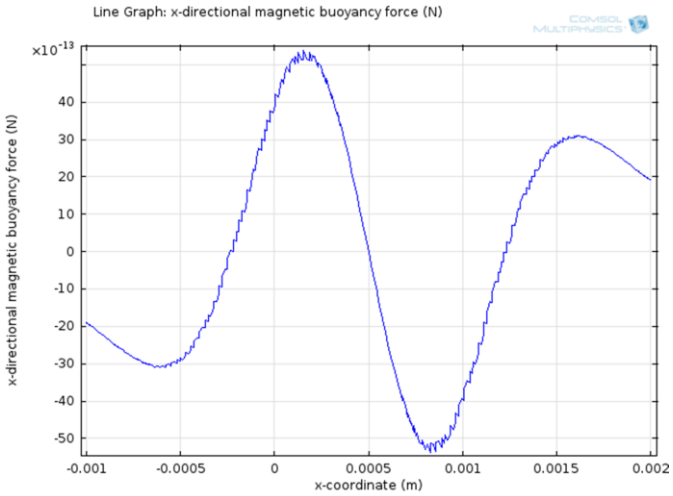

(a)

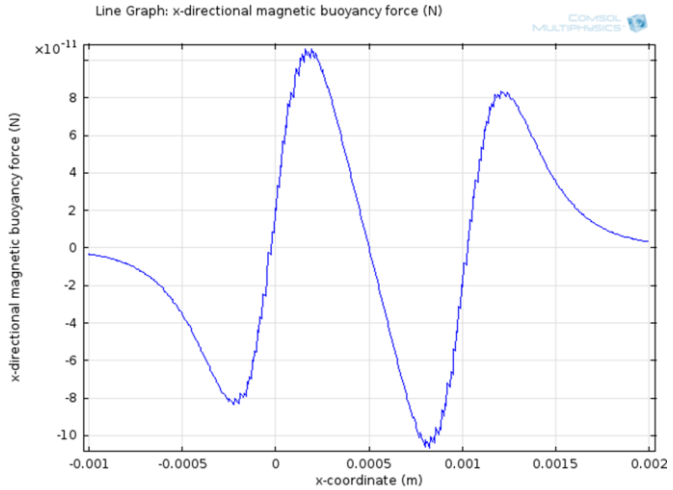

(b)

Figure 14: Simulation result for magnetic buoyancy force along a horizontal line cut through the chamber for the case of two single wires conducting 30.3 A with opposite directions current.

For the case that the two wires are conducting 30.3 A in the same direction, the simulation results are shown in Figure 15. Again, the distribution of the *x*-directional magnetic buoyancy force is similar to the case of a single wire when the distance between the chamber and the wire-mesh coil z = 1 mm. The zero force occurs at the middle point

of the two wires. The peak value of the magnitude of the *x*-directional magnetic buoyancy force is around 1.6×10^{-11} N, which is more than triple that achieved with the previous configurations. Particles right above the wires experience a magnetic buoyancy force approximately equal to 1.2×10^{-11} N. This configuration can efficiently move particles right above the wires. In Figure 15 (b), when the distance between the chamber and wire-mesh coil is decreased to 0.4 mm, the shape of curve for *x* between range 0 and 1 mm changes from a monotonous shape to a fluctuating shape. We can see that the particles between the two wires tend to move towards the center point ($x = 0$). As a result, the effect of two parallel wires with same direction current can be varied as a function of the distance between the chamber and wire-mesh. When distance *z* is large, the two wires case is equivalent to the single wire case. This configuration can also be applied to trap non-magnetic particles when distance *z* is short enough.

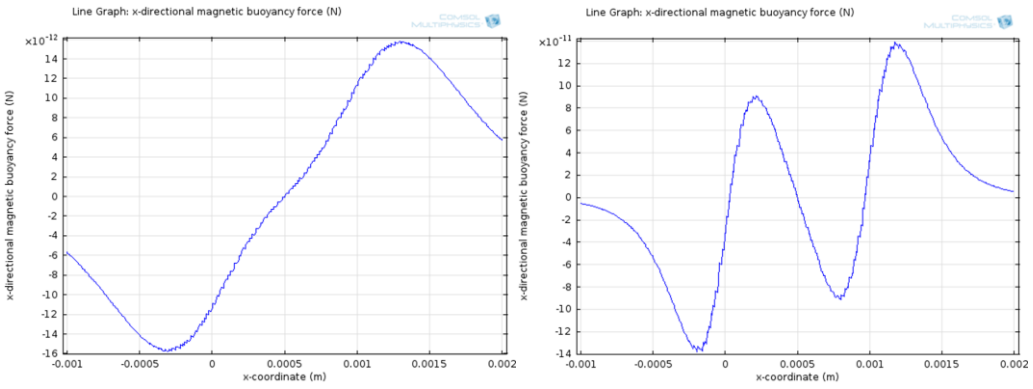

(a) (b)

Figure 15: Simulation results for magnetic buoyancy force along a horizontal line cut through the chamber, for the case of two single wires conducting 30.3 A with the same direction.

3.1.3 Wire Heating

The temperature of a wire conducting a current, and its immediate environment, will increase through the Joule heating effect. The Joule heating effect follows Joule's First Law, stating that the amount of heat (Q) released is proportional to the square of the current I and the resistance R of the conductor:

$$Q = I^2 Rt\,, \tag{15}$$

and t is the length of time that the current has been applied. The increase of temperature of the wire is given by

$$\Delta T = \frac{Q}{mC}\,, \tag{16}$$

where C is the heat capacity of the wire, and m is the mass of the wire. By combining Equation (16) and Equation (15), we can plot the increase of temperature as a function of time. For a segment of copper wire with length L, cross-sectional area A = 203 μm x 178 μm, the increase in temperature is

$$\Delta T = \frac{I^2 Rt}{mC} = \frac{I^2 \dfrac{\mathrm{L}}{\sigma A} t}{LA\rho C} = \frac{I^2 t}{\sigma A^2 \rho C}\,. \tag{17}$$

Copper has conductivity $\sigma = 5.998\times10^7$ S/m, density $\rho = 8700$ kg/m^3 and heat capacity $C = 385$ J/(kg·K), resulting in a temperature increment $\Delta T = 3430$ K within 1 s.

This temperature rise will burn the copper wire, and we will need a way to reduce the heat generated by the wire, and/or consider convective cooling of the wire-mesh coil. One approach is to deliver the current in the form of a series of pulses instead of a steady current. The duration of each current pulse is t_1, and adjacent pulses are set to be t_2 apart. On the appearance of a current pulse, the non-magnetic particle will be accelerated

and the wire will heat up. Following the current pulse, the motion of the particle will be hampered by the fluid drag force and the wire will cool down to some degree. At the end of each current pulse, the particle will reach some maximum speed. Then its speed will drop to some minimum value before the occurrence of the next pulse. We can expect that the speed will increase in a zig-zag manner during the next few cycles. But since the fluid drag force is proportional to the speed of the particle, the acceleration and deceleration process will reach a steady state, which means the velocity curve will become periodic with peak value v_u and valley value v_l. This steady state can be found by an iterative algorithm, i.e., starting with an initial velocity, perform simulations for a series of acceleration-deceleration cycles until two successive cycles have almost the same peak and valley velocities.

Figure 16 shows the velocity profile for a series of six 30.3 A current pulses of 5 ms each, separated by 5 ms. The horizontal axis represents time in seconds, and the vertical axis represents the instantaneous speed of a non-magnetic particle. For the case shown in Figure 16, v_u and v_l were found to be v_u = 50 μm/s, v_l = 0 μm/s using the iterative algorithm proposed in the previous paragraph. We can see that the acceleration and deceleration time of the non-magnnetic particle is far shorter than the duration of the current pulse, so that the motion of the particle can be assumed to be uniform during the appearance of current pulse.

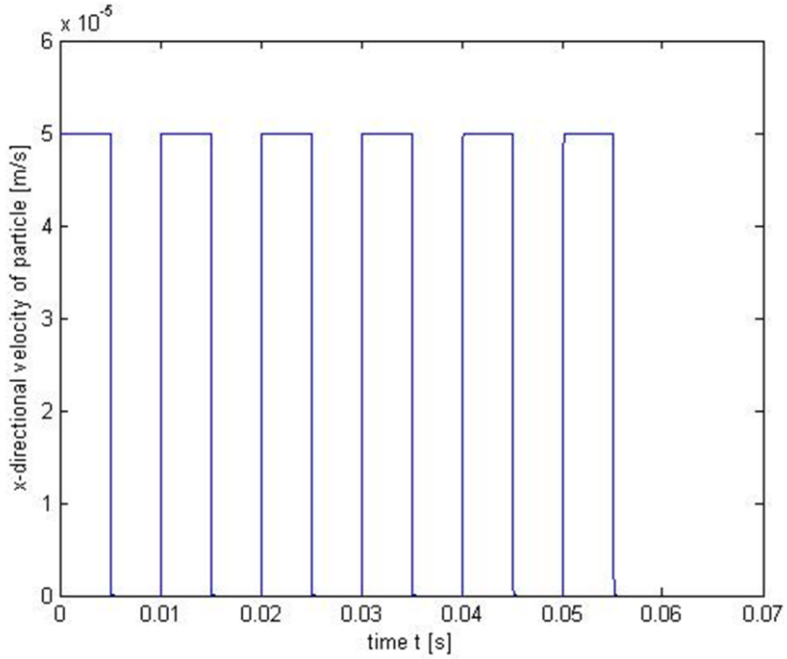

Figure 16: The acceleration and deceleration of non-magnetic particle in response to a series of 6 current pulses with 5 ms duration and 5 ms between pulses. Each pulse was 30.3 A.

The average speed of the non-magnetic particle is the definite integral of one period of the velocity-time curve divided by the period, which is 2.52×10^{-5} m/s for this case. In other words, the time required to move a non-magnetic particle over a certain distance using a series of current pulses has almost doubled compared to using a steady current. The non-magnetic particles will be moved with speed v_m during the current pulse and stop whtn the current is off. The time gap t_2 allows the wire coll down, but reduces the manipulation efficiency. It is clear that t_1 and t_2 need to be optimized to find an acceptable solution.

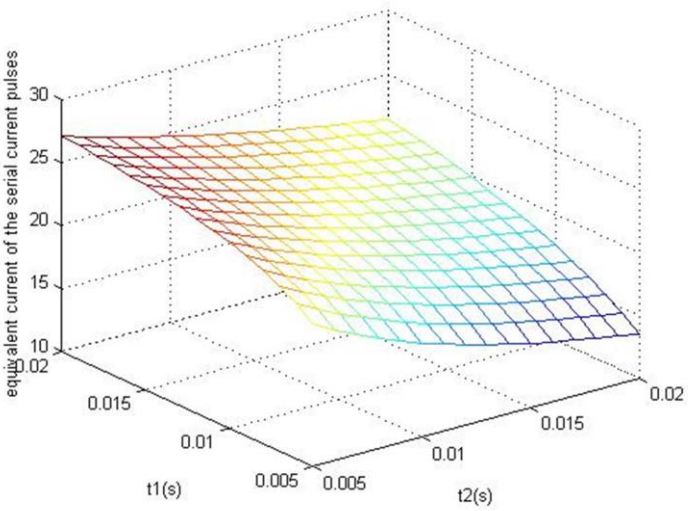

(a)

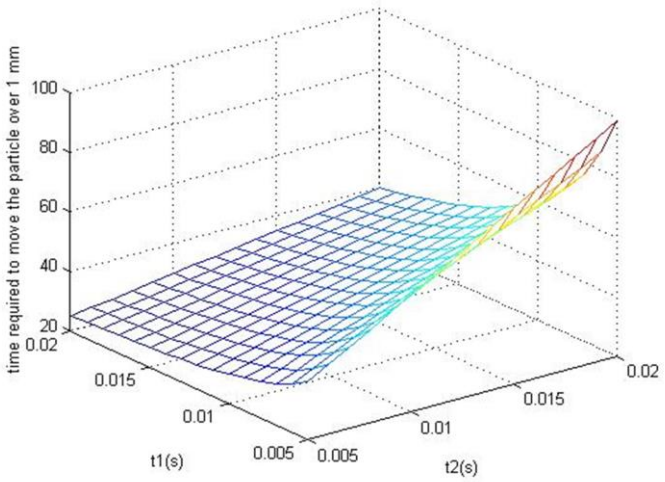

(b)

Figure 17: (a) The effective current in response to current pulses with different duration and interval. (b) Time required to move the particle over a certain distance (1 mm).

As shown in 17, as t_1 increases and t_2 decreases, the average speed of the non-magnetic particle increases, and it will take less time to move the particle over a certain distance. However, shorter t_2 allows less time for the wire to cool down, so there is a

tradeoff between manipulation speed and heat dissipation.

In order to find a balance between the two, the electromagnetic Joule Heating model and Heat Transfer model were applied to simulate the heat generation and dissipation of a section of copper wire inside a certain environment using COMSOL Multi-Physics. In our case, the wire-mesh coil is laid down on a Printed Circuit Board (PCB) and the single wires are embedded into a non-conductive substrate (see Figure 18). The gray region surrounding the wire is the non-conductive substrate of the PCB (PVC 10% plasticizer). A cooling device consisting of an aluminum plate with scale 150 mm x 150 mm x 10 mm with an embedded u-shaped copper tube was used. A pump drives water through the copper tube to cool down the aluminum plate. The temperature of the water was set to 4 degrees Celsius. The wire-mesh coil is indirectly in contact with the aluminum plate through thermally conductive silicone paste, OMEGATHERM-201, which has high thermal conductivity (8.5464 W/mK), coupled with high insulation resistance and high dielectric strength.

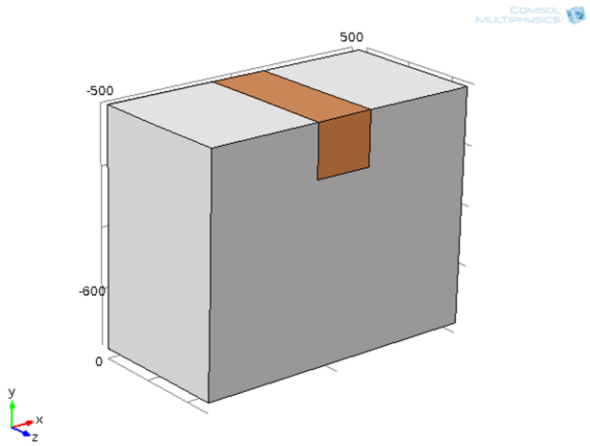

Figure 18: Model of a segment of the single copper wire and the non-conductive substrate. The orange block in the top middle is the copper wire (203 μm x 178 μm in cross-sectional dimension).

Assuming that the model in Figure 18 is homogeneous in the *z*-direction, a 2-D model in the *x*-*y* plane was used for simulation. When conducting current into the wire, the wire can be modeled as a heat source with heat density

$$\rho_h = \frac{I^2 R}{V} = \frac{I^2 \frac{l}{\sigma A}}{Al} = \frac{I^2}{A^2 \sigma}, \tag{18}$$

since we are conducting a serials of current pulses through the wire, we will assume that the duration of each pulse is t_1, that the distance between adjacent pulses is t_2, and that a long series of pulses are used so that we can treat the current pulses as a periodic pattern. The series of pulses is equivalent to an effective steady current I_e, generating the same heat as a single current pulse. The equivalent steady current can be determined by solving the equation $Q = I_e{}^2 R(t_1 + t_2) = I^2 R t_1$ resulting in

$$I_e = I\sqrt{\frac{t_1}{t_1 + t_2}}, \tag{19}$$

for the case mentioned in Section 3.1.1, $t_1 = t_2$, hence $I_e = \frac{\sqrt{2}}{2} I$.

The cooling liquid is set into motion in the *x*-direction (Figure 18) and flows over the top of the wire. For simplification, we will assume that the flow of the liquid is fast enough so that the temperature of the liquid will remain at room temperature all the time.

We first explored the effect of convective cooling, and the results are shown in Figure 19. The temperature rise at the center of wire is constrained to 100 K with convective cooling, while the temperature rise at the center of the wire is up to 450 K without convective cooling. Also, with cooling (see Figure 19-a), the temperature saturates at 100 K, but the temperature continues to rise without convective cooling

(Figure 19-c). In conclusion, convective cooling significantly cools down the wire.

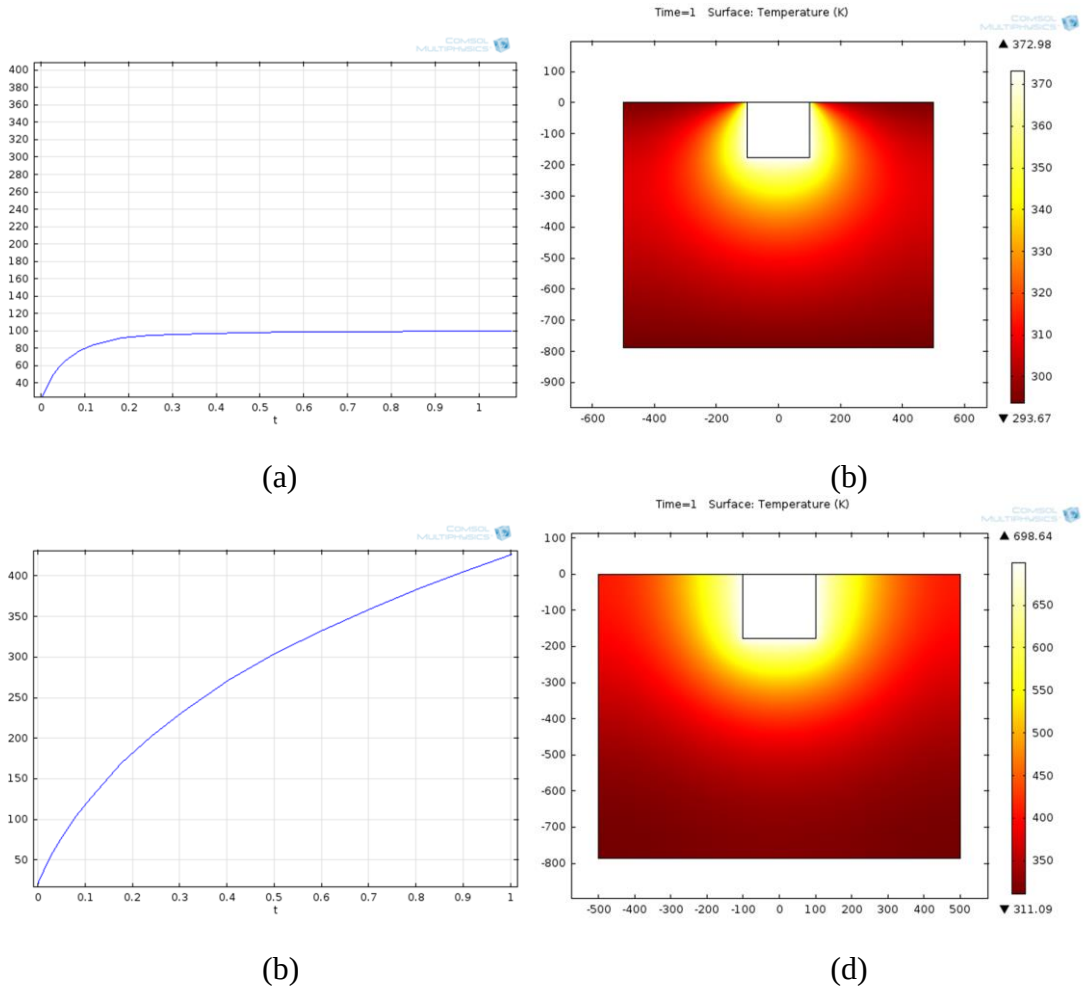

Figure 19: Simulation for convective cooling for the single wire, with $t_1 = 5$ ms, $t_2 = 5$ ms. (a) the change of temperature at the center of the wire in one second with convective cooling; (b) the distribution of the temperature among the single wire and the non-conductive substrate with convective cooling; (c) the change of temperature at the center of the single wire in one second without convective cooling; (d) the distribution of the temperature along the single wire and the non-conductive substrate without convective cooling.

Next, we explored the effects of changing t_1 and t_2. The input current pulses in the simulations were configured by selecting different combinations of t_1 and t_2 drawn from a range of 5 ms to 20 ms. This range was decided on using the fact that the switching component of the device has a delay from 0.5 ms to 1 ms. For each combination

considered, the effective current and time required to move the particle over a distance of 1 mm were calculated by MATLAB and imported to COMSOL Multi-physics to perform a parameter sweep simulation. Sixteen values were selected for t_1 and t_2, respectively, for a total of 256 combinations.

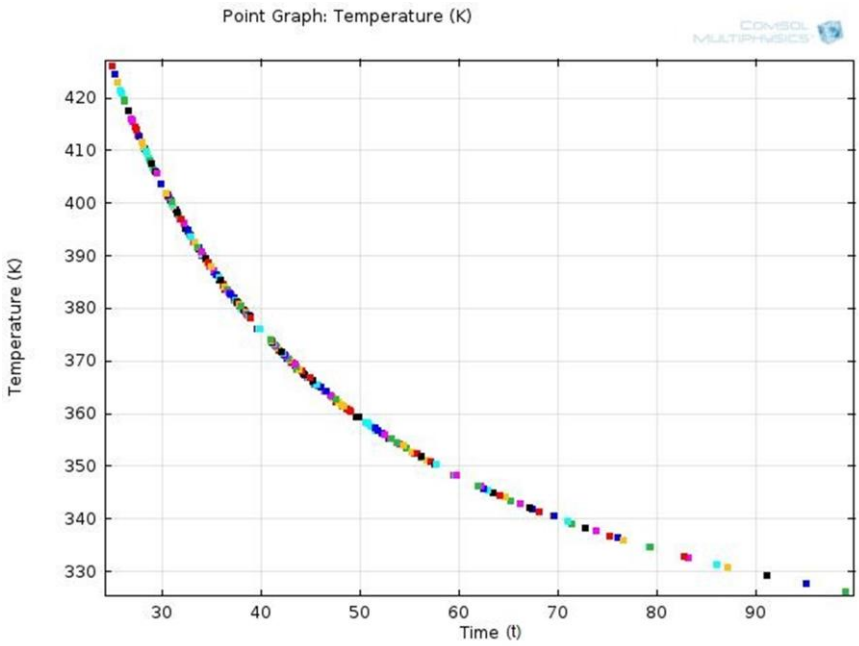

Figure 20: Temperature at the center of the single wire as a function of the time required to move the particle 1 mm. Each measurement point represents one unique combination of t_1 and t_2.

For each combination, the temperature at the center of a single wire at the end of the stimulus interval was generated, and this temperature is graphed in Figure 20, where the *x*-axis is the time required to move the particle over 1 mm, and the *y*-axis is the temperature at the center of the wire after such time.

The living cell will survive if we limit the temperature of the wire to less than 350 K. To choose a reasonable timing for the current pulse, we need to limit the temperature below 350 K while minimizing the time needed to move the particles over a certain distance. Figure 20 shows that the temperature does not exceed 350 K if $t \leq 59.56$s.

Selecting the final temperature T = 350 K and total time to move the particle t = 59.56 s and by going back to the simulation data, we see that this operating point corresponds to an equivalent current I = 17.32 A. Using Figure 17,we can then determine that. t_1 = 6 ms, and t_2 =12 ms.

3.2 Development of the Electronic Circuitry and Software System

3.2.1 Fabrication of Wire-mesh Coil

A wire-mesh coil reconfigurable coil prototype, with 10 wires in both x and y direction, each 10 mm in length, 203 μm wide and 178 μm in thick, was fabricated (see Figure 21). The spacing between two neighboring wires was 1 mm. The twenty wires terminate to 40 pins, acting as input ports of the prototype and these pins are connected to a control unit. The printed circuit board has two sides, represented by different colors of the wire. By pre-storing a sequence of excitation patterns inside the control unit, one can dynamically alter the magnetic field generated by the wire-mesh coil.

The PCB was manufactured by Sunstone PCB123. In order to dynamically deliver the excitation patterns to the wire-mesh coil in any temporal order, we need to pre-define these patterns and store them in a memory unit. Then transform these digital signals to analog signals and distribute them to the pins of our wire-mesh coil prototype.

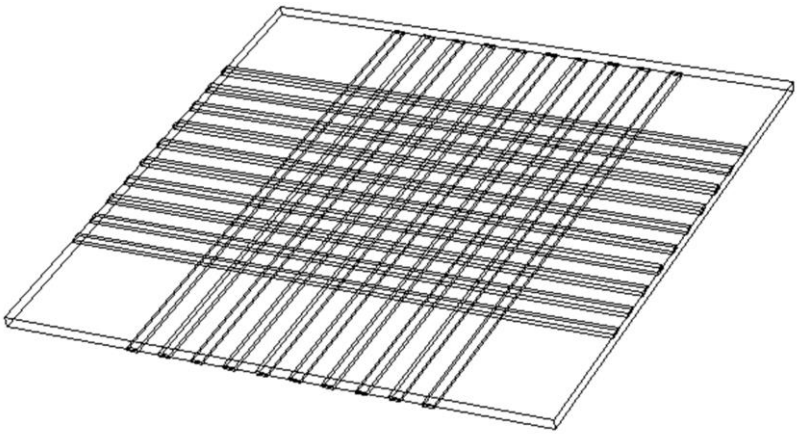

(a)

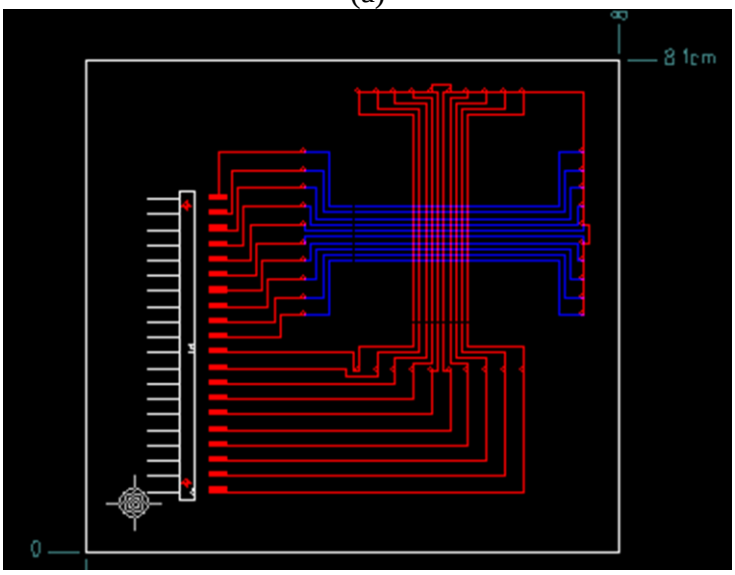

(b)

Figure 21: (a) Prototype of the wire-mesh reconfigurable coil. Two layers of 20 wires each are etched on a double-sided printed circuit board. (b) Layout of the wire-mesh coil circuit by Sunstone PCB123.

3.2.2 Development of the Switching Unit and Power Supply

The control system for delivering input waveforms to the wire-mesh coil is based on a DE2 Field-programmable gate array (FPGA) board. Input patterns are pre-stored into the Read Only Memory (ROM) unit of DE2 board. These input patterns are sent out through the GPIO port of DE2 board with 0/3.3 volts.

We expect to conduct up to 30 Amps current into the wire-mesh coil. However our control unit, a DE2 FPGA board, cannot deliver such high current. As a result, we need a switching unit between the control unit and the wire-mesh coil prototype to control the open and close status of each channel in accordance with the control signal.

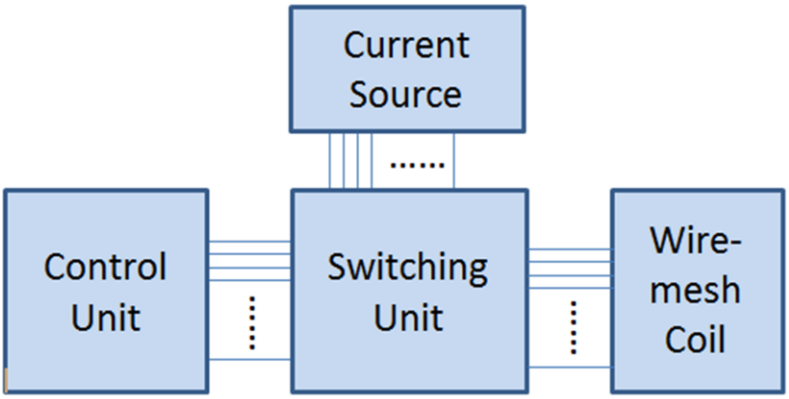

Figure 22: Layout of the device. Current source is capable of delivering multi-channel high current to the wire-mesh coil. The open and close status of each channel is controlled by the switching unit according to the signal from the control unit.

To switch big currents using small signals, we need relays. Relays come in a variety of factors, styles, and technologies. Depending on the application, only one relay type may be suitable. The traditional electromechanical relays can support a wide range of signal characteristics, from low voltage/current to high voltage/current and from DC to

GHz frequencies. But one important limitation is the speed of switching; electromechanical relays are relatively slow devices. Solid State Relays (SSRs) are a faster alternative to electromechanical relays because their switching time is dependent on the time required to power the LED on and off – approximately 1 ms and 0.5 ms, respectively because there are no mechanical parts.

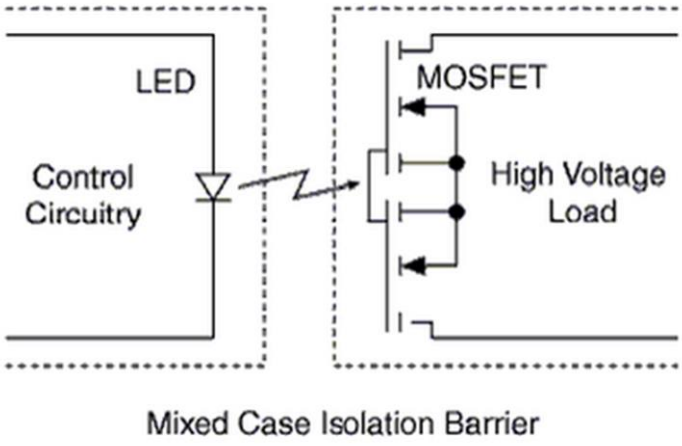

Figure 23: Solid State Relay (SSR): Light from the encapsulated LED actuates the photo-sensitive MOSFET and allows current to flow through it.

In this experiment, we need to control up to 30 A current for each channel of the wire-mesh coil by the 3.3 volt output of DE2 board. This can be accomplished by a Magnecraft 6210AXXSZS-DC3 solid state relay (see Figure 24), which accepts a 3V-32V DC signal as input and delivers 24V-280V AC output. The switching unit is composed of 20 such Solid State Relays.

Figure 24: Magnecraft 6210AXXSZS-DC3 Input: 3V - 32V DC Output: 24V - 280V AC.

Unlike mechanical relays, the output of a SSR contains no moving parts. Instead, two silicon-controlled rectifiers (SCRs) in inverse parallel are used to switch load current (see Figure 25 for a circuit diagram). When an input signal is on, a small amount of current (150 mA typically) flows from the power source, through the optical isolator and into the gate of the forward-biased SCR. This turns on the SCR and allows the load current to flow.

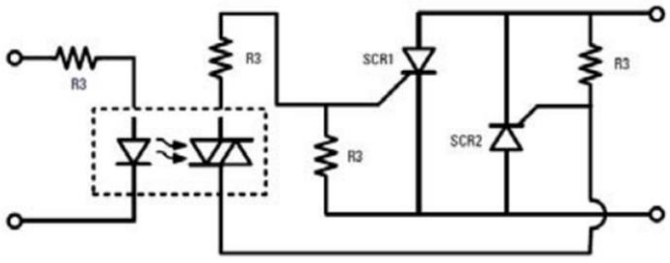

Figure 25: Simplified solid state relay schematic.

A solid state relay cannot be bench tested with a multimeter because the multimeter cannot provide sufficient current to turn on the SCRs (Crydom, 2010). The resistance of the SCR is approximately zero in conduction mode. To deliver around 30 A current pulse to the single copper wire, a 60Hz AC source with 120 V effective voltage was applied. Each channel of the wire-mesh coil consists of a single copper wire in series with a solid state relay. These channels are connected in parallel and driven by the AC source. As shown in Figure 26, when any one of the SSRs is set into conduction mode, current will flow through the corresponding channel. The amplitude of the current mainly depends on the resistance of the channel.

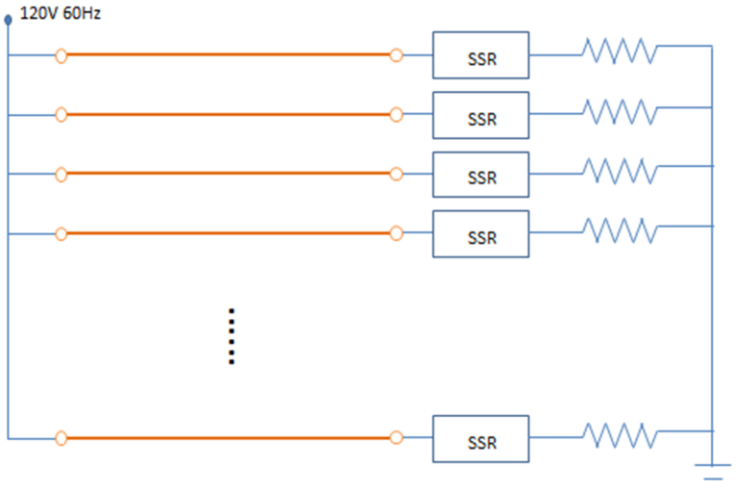

Figure 26: Schematic view of the circuit to deliver current pulses to the wire-mesh coil.

As proposed in Section 3.1.2, the serial current pulses being delivered to the single wire have a duration of 6 ms, and 12 ms between adjacent pulses. The voltage supplied by the AC power source is: $V_{AC}(t) = 120\sqrt{2}\sin(2\pi f \cdot t)$, where f = 60 Hz is the frequency of the AC source. The digital control signal delivered by the FPGA DE2 board

can be represented as $V_p = u(t - t_d) - u(t - t_d - 0.006)$, where t_d is the delay of the positive edge of the signal with respect to the power source. The temporal relationship between the AC power waveform and the control signal is shown in Figure 27.

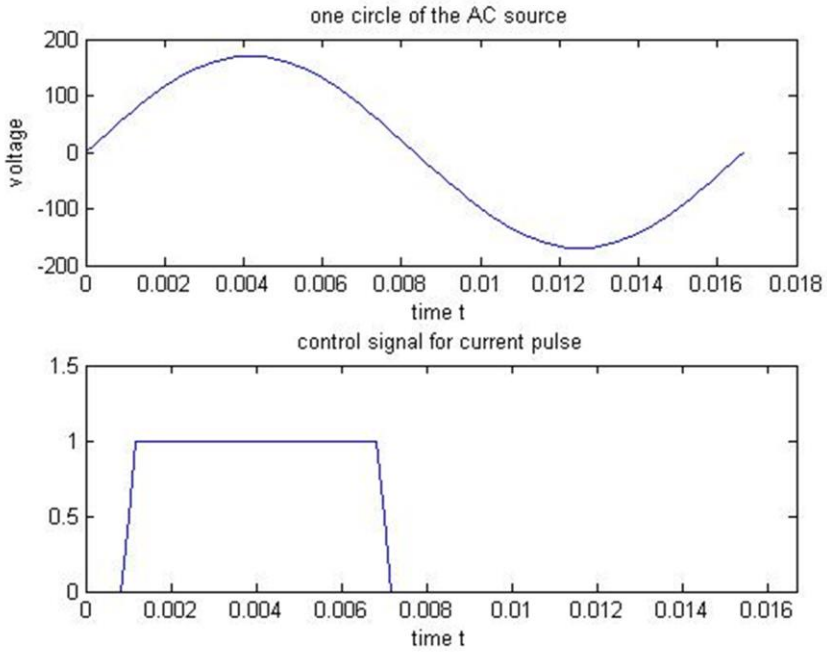

Figure 27: Voltage of the AC power source and control signal.

The SSR is turned into the 'on' mode when the control signal is logical 1. The actual voltage applied to the channel can be expressed as

$$V = 120\sqrt{2}\sin(2\pi f \cdot t) \cdot (u(t - t_d) - u(t - t_d - 0.006)).$$

Since t_d is unknown, the positive edge of the control signal may occur at any time among one period of the AC power source. This will make the amplitude of the serial current source variable and unpredictable. The magnitude of the current is proportional to the voltage applied to the circuit, while the magnetic buoyancy force is proportional to the square of the current (Eq. 6). When the peak or valley of the AC curve is right at the

middle of the control pulse, the effect of moving the non-magnetic particle is maximized. When the zero point of the curve meets the middle point of the control signal, this effect is minimized.

To achieve stable and effective manipulation of the non-magnetic particle, two approaches can be taken into consideration. One approach is to synchronize the 120V AC waveform with the control signal, which sets up a certain relative temporal position between the AC waveform and the control signal, so that each current pulse delivers the maximum effect for particle manipulation.

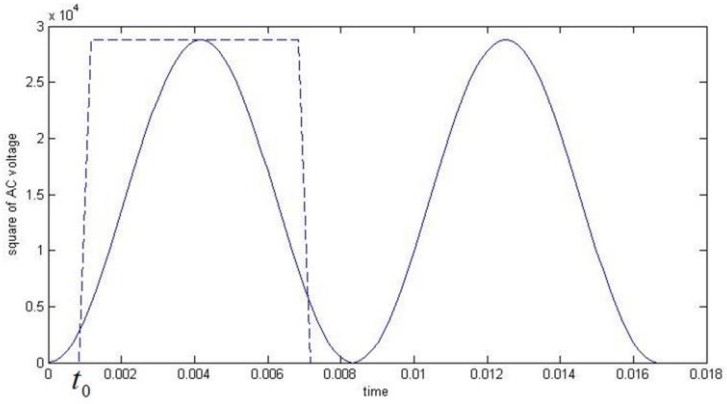

Figure 28: Relative temporal position between the square of AC source waveform and the control signal.

As shown in Figure 28, the solid curve depicts the square of the AC voltage, which is proportional to the magnetic buoyancy force. The dashed line is the control signal and starts at t_0. The control signal pulse should maximally cover the AC voltage-squared curve. Thus, assuming that $V_{AC}(0) = 0$, we need to maximize

$$A = \int_{t_0}^{t_0+0.006} {V_{AC}}^2 dt = 28800 \int_{t_0}^{t_0+0.006} \sin^2(2\pi f \cdot t) dt = 28800 \left(\frac{t}{2} - \frac{\sin(4\pi f \cdot t)}{8\pi f} \right) \Bigg|_{t_0}^{t_0+0.006}.$$

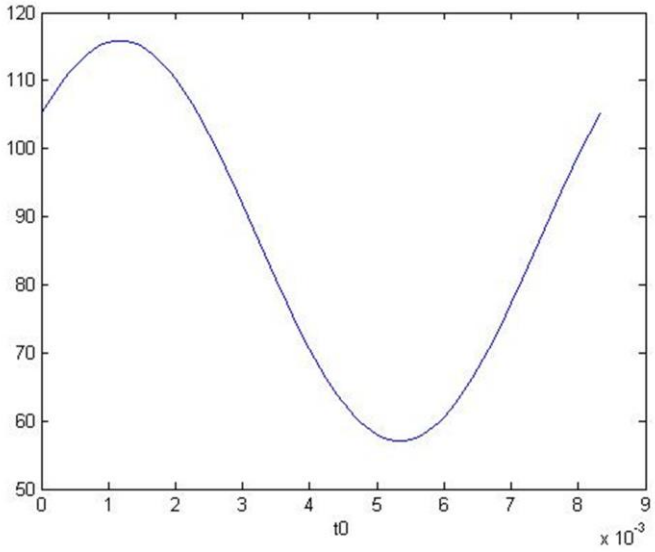

Figure 29: Variation of A with respect to t_0.

Figure 29 shows the value of A as a function of t_0 over one cycle. The definite integral reaches its maximum when t_0 = 1.167 ms. In conclusion, the control pulse needs to be fine-tuned to occur 1.167 ms after each zero crossing of the AC waveform's upper (or lower) half. This can be achieved, as shown in Figure 30, by applying a sensor to the AC power source. When the AC voltage reaches $V_{AC}(0.001167)$ = 72.28 V, an enable signal will be sent to the GPIO port of the DE2 board. Then the board will deliver the control signal to the solid state relay.

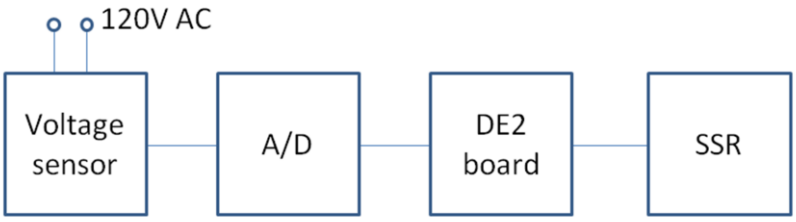

Figure 30: Schematic view of the synchronization mechanism.

3.2.3 Development of Control Unit with FPGA

For the purpose of dynamically delivering the excitation patterns to the wire-mesh coil in any temporal order, we pre-define the control signal patterns with a Memory Initialization File (MIF) and pre-store them into the Read Only Memory (ROM) of the DE2 FPGA board. Then these digital signals are transformed to analog signals and distributed to the pins of our wire-mesh coil prototype.

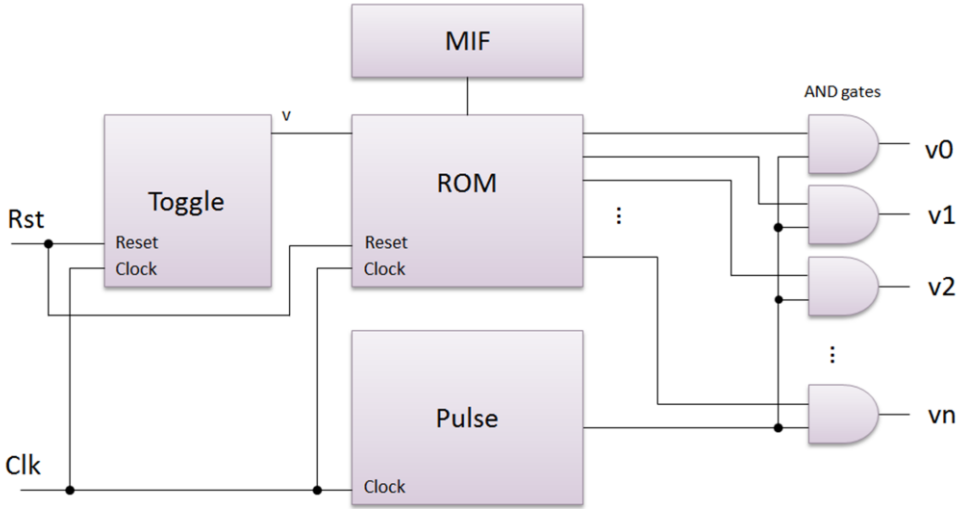

Figure 31: Schematic view of control system in DE2 FPGA board.

As shown in Figure 31, the ROM module reads the control signal patterns from memory and outputs them as a vector register. The Pulse module generates pulses with arbitrary durations and gaps, which decides the current pulse pattern in the wire-mesh coil. The outputs of the ROM and Pulse modules are combined through an array of logic AND gates, and delivered to the switching unit of the control system.

The MIF (memory initialization file) is an ASCII text file that specifies the initial

content of a memory block, that is, the initial values for each address. A sample code for defining the address in memory and the data in each address is

00 : 100000;

01 : 010000;

02 : 001000;

03 : 000100;

04 : 000010;

05 : 000001;

The left column specifies the address, and the right column is the data. When the ROM module gets access to an address, the data in this address will be read and delivered to the output. The data in the sample code is a set of 6-bit digits, which correspond to 6 channels of the wire-mesh coil. Digit 1 means the channel is on, digit 0 means off. When toggling between different addresses, the on/off status of each channel will be modified. In Figure 33, v is the signal that controls the address toggle of module ROM. At the positive edge of v, ROM will access the next address. The timing of signal v is pre-stored in the Toggle module and can be modified accordingly.

Chapter 4 Bench Experiments

Experimental investigations have been performed to validate the proposed approach. For the first experiment, we measured the magnetic field generated by a single copper wire with a searching coil. Next we implemented a single channel circuit of the device to verify the logic of the control/switching unit and measured the current conducted into the single copper wire. In the third experiment, we built a simplified three-by-three wire-mesh coil device to test its performance in manipulating and trapping non-magnetic particles.

4.1 Measurement of Current in one Channel

In this experiment, we investigate two questions:

1. Whether we can deliver a current pulse of 28.9 A to a channel.
2. Whether the copper wire in the wire-mesh coil can sustain such current pulse.

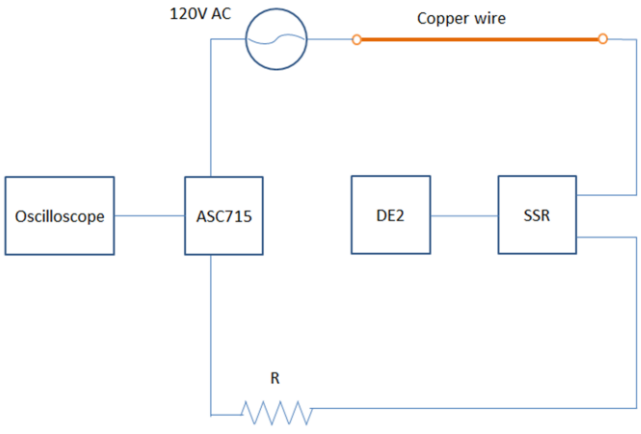

Figure 32: Schematic view for the experiment measuring the amplitude of the current pulse conducted through a single copper wire.

Figure 32 shows the setup of the experiment. To avoid burning out the wire-mesh coil fabricated by PCB, we used a segment of enameled copper wire with diameter 0.2 mm for testing, which has sectional area $A = 3.14 \times 10^{-8}$ m^2, which is comparable to the PCB wire, which has an area of 203 μm x 178 μm= 3.61×10^{-8} m^2. The enameled copper wire's cross-sectional area is 13% smaller than the wire-mesh coil, thus if it can sustain the current pulse, the wire-mesh coil will also be able to endure.

A resistor was connected in series with the copper wire to limit the current in the circuit. The value of the resistor was either 10 ohms, 8.2 ohms or 5.6 ohms. Since the other parts of the circuit had really low resistance, the peak value of the 120 V AC source is close to 170 V. Thus we expect to produce current pulses with maximum value 10 A, 20.7 A and 30.3 A for the three resistors, respectively. To measure the amplitude of the current pulse with 6 ms duration, we used an ASC715 Hall effect-based linear current sensor IC.

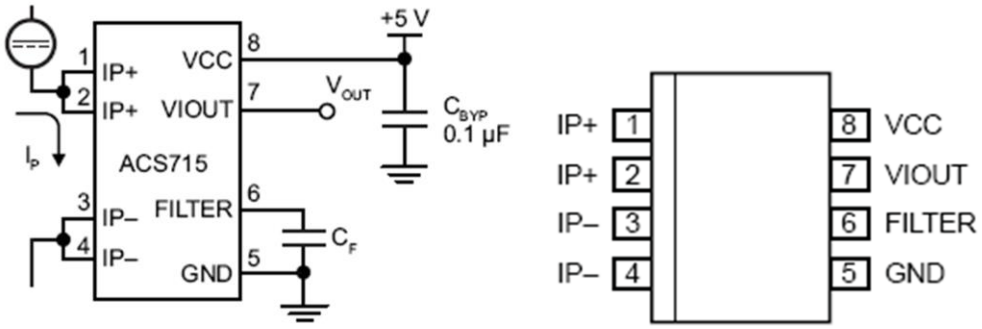

Figure 33: Pin-out diagram of ASC715 hall effect-based current sensor IC.

As shown in Figure 33, the applied current flowing through the copper conduction

path from pin 1 to pin 3 generates a magnetic field which the Hall IC converts into a proportional voltage. This voltage can be measured from pin 7, the output of the IC. When supplied by 5 V DC voltage, the characteristic performance of the sensor is shown in Figure 34. The output voltage rises linearly as the current flows through the sensor changes, and the sensitivity is around 133 mV/A.

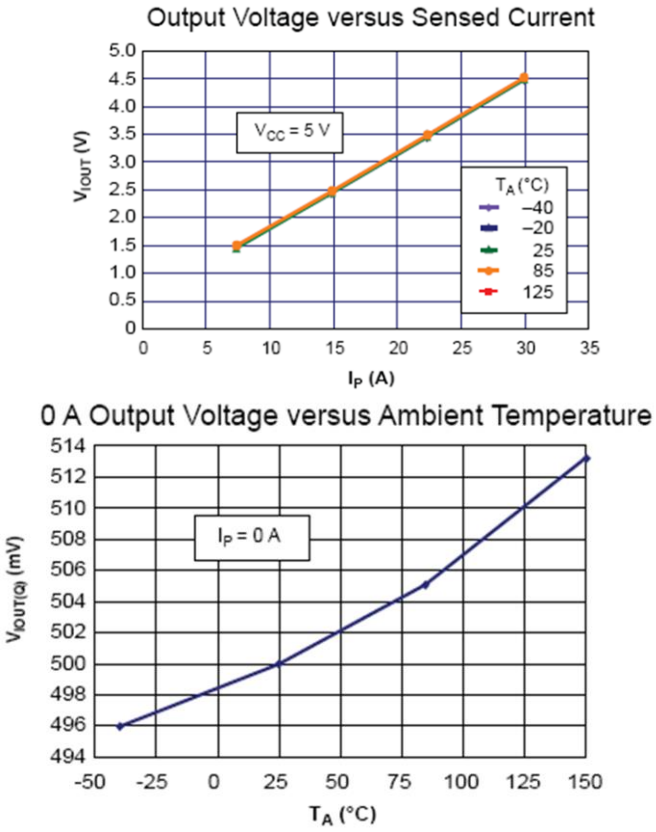

Figure 34: Characteristic performance of ACS715 Hall effect-based linear current sensor.

At room temperature, with no current flowing through the sensor, the output voltage was measured to be 0.5 V, which is consistent with the data shown in the bottom panel of Figure 34. The output pin of the current sensor was connected to the Tektronics oscilloscope. A current pulse in the circuit will cause a sudden output voltage change in

the sensor. This voltage change will be captured by the oscilloscope in trigger mode. For this experiment, The DE2 board sends a control signal with 6 ms duration to the SSR so that the circuit will be set into conduction for 6 ms. Theoretically there will be a 6 ms current pulse flow through the current sensor, resulting in a waveform captured by the oscilloscope.

Table 1: Peak values of output voltage (*V*) in response to a single current pulse with 6 ms duration.

10 Ohms		8.2 Ohms		5.6 Ohms	
2.24	0	2.6	0	0	0
2.28	2.28	0	0	3.52	3.52
2.28	0	2.6	2.64	0	3.52
0	0	0	0	0	3.52
0	2.24	0	2.64	0	0
0	2.28	0	0	3.52	3.52
2.2	0	0	0	0	3.52
0	0	0	0	0	0
0	0	2.64	0	0	3.52
0	0	0	2.64	3.52	0
2.24	2.28	2.64	0	3.52	0
0	2.28	2.64	0	3.52	0
2.2	2.24	2.64	2.64	0	0
0	0	2.64	0	0	0
2.28	2.24	2.64	2.64	3.52	0

A typical voltage change captured by the oscilloscope, when a 10 Ω resistor is used, is shown in Figure 35. The peak-to-peak value of the pulse is 2.28 V, which corresponds to approximately 14 A current pulse flow in the loop. The duration of the pulse is around 8 ms, which is 2 ms longer than the control signal sent by the control unit.

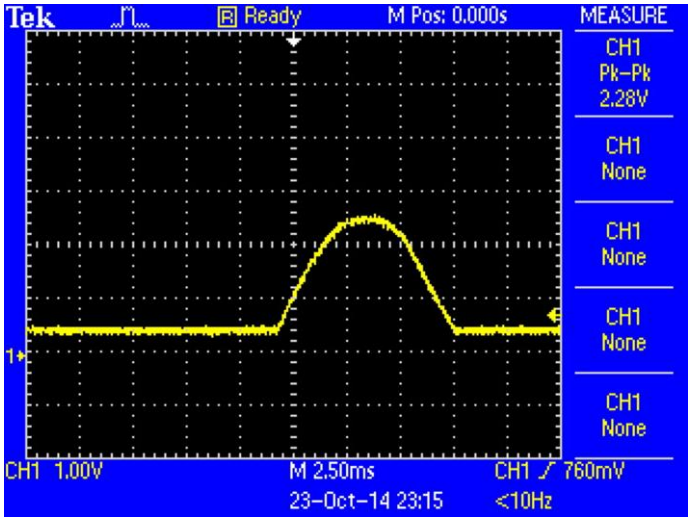

Figure 35: Output of the ASC715 Hall effect-based linear current sensor in response to the current pulse flows through the circuit.

Table 2 shows the recorded voltage change at the output port of the current sensor in response to the current pulse. The experiment was repeated 30 times for each of the three resistors. According to Table 2, only 43.3% of the measured values are non-zero. The zeros can be caused by two reasons. First, the ACS 715 current sensor is unipolar and can only measure current in one direction. Since the control signal is not synchronized with the AC power waveform, if the control signal meets the lower half of the AC current, the current sensor will not be able to detect the current. Second, the control signal does not cover the peak value of the AC waveform, as a result, the current pulse may not be able to reach the threshold to trigger the oscilloscope. To explore this hypothesis, a

second experiment was conducted where we programmed the DE2 board to send two successive pulses as control signals to the SSR. If the Hall effect sensor captures either one of the pulses, there will a peak shown on the oscilloscope. As a result, for the second experiment we expect a better chance to observe current pulse from the oscilloscope. The two successive control signals are 12 ms apart and each signal has a duration of 6 ms.

Table 2: Peak value of output voltage (V) in response to a two current pulses with 6 ms durations and set to 12 ms apart.

10 Ohms		8.2 Ohms		5.6 Ohms	
2.28	2.2	2.64	2.64	3.48	3.52
2.28	2.24	2.64	2.64	0	3.52
2.2	2.28	2.6	2.64	3.52	0
2.28	2.2	0	0	3.52	3.52
2.24	0	2.6	2.6	0	3.56
2.24	0	2.64	0	3.52	3.52
2.28	2.28	2.56	2.64	0	3.52
2.24	2.24	2.64	2.64	3.52	3.52
2.24	2.28	2.64	0	3.52	0
0	0	2.64	2.64	3.48	3.48
0	0	0	2.6	3.52	0
2.2	2.24	2.64	2.64	3.48	0
2.24	2.24	0	0	3.52	0
0	2.24	0	2.6	3.52	3.52
2.24	2.24	2.64	2.64	3.56	3.52

By applying two control signals to the SSR, the resultant two current pulses flowing though the circuit have more opportunities to trigger the oscilloscope. The percentage of non-zero measurements was increased to 74.4%. As discussed in Section 3.1.1, the magnetic buoyancy force is independent of the direction of the magnetic field and the direction of the current passing through the wire, but depends on the gradient of the magnetic field. We expect a significant motion of non-magnetic particles in response to AC current pulses. If it doesn't work well, we will try to synchronize the control signal with the AC source or apply a DC power source as proposed in Section 3.2 so that unidirectional current pulses will be obtained.

The peak value of current pulse in the circuit can be obtained by referring to the datasheet of the ACS715 current sensor IC, which is shown in Table 3.

Table 3: Current measured by ACS715 Hall effect current sensor.

Resistor	Average voltage	Current
10 Ohms	2.25 V	13 A
8.2 Ohms	2.63 V	16 A
5.6 Ohms	3.52 V	23.5 A

In conclusion to the experiment, we achieved up to 23.5 A current pulses without burning out the copper wire in single channel test. Next we will decrease the resistance to see whether the circuit can support 28.9 A, which is our objective value. In the next experiment, we will conduct current to multiple channels to examine how well the wire mesh coil can manipulate and trap non-magnetic particles.

4.2 Wire-mesh Coil Testbench

This experiment aims at testing the performance of wire-mesh coil in manipulating and trapping non-magnetic particles. For manipulation purpose, as discussed in Section 3.1, we will conduct current to one single copper wire of the wire-mesh coil each time and observe the motion of non-magnetic particles adjacent to the wire by microscope. For trapping purposes, we will need to form a single loop or figure-eight pattern of current.

The testbench prototype was simplified to a three-by-three wire-mesh coil composed of six copper wires as shown in Figure 36. The on and off state of each channel was controlled by an AC solid state relay. Control signal patterns were pre-stored into the Read Only Memory of the FPGA board and delivered to the SSR array through the GPIO ports. The wire-mesh coil was connected in series with a power resistor R, of 2.5 ohms resistance and 2816 Watts rated power. When supplied with 120 V AC power, the current flowing through the copper wire was around 50 A and the power resistor consumed about 2880 Watts of power. The wire-mesh coil shown in Figure 36 was composed of 3 horizontal and 3 vertical copper wires. The six copper wires shared a common ground at one end and were connected to six SSRs at the other end. For this configuration, the current directions in the parallel wires were always the same, and the mesh can only be used to transport non-magnetic particles. The current in the wire-mesh coil was measured by a Hall Effect current sensor and observed by an oscilloscope.

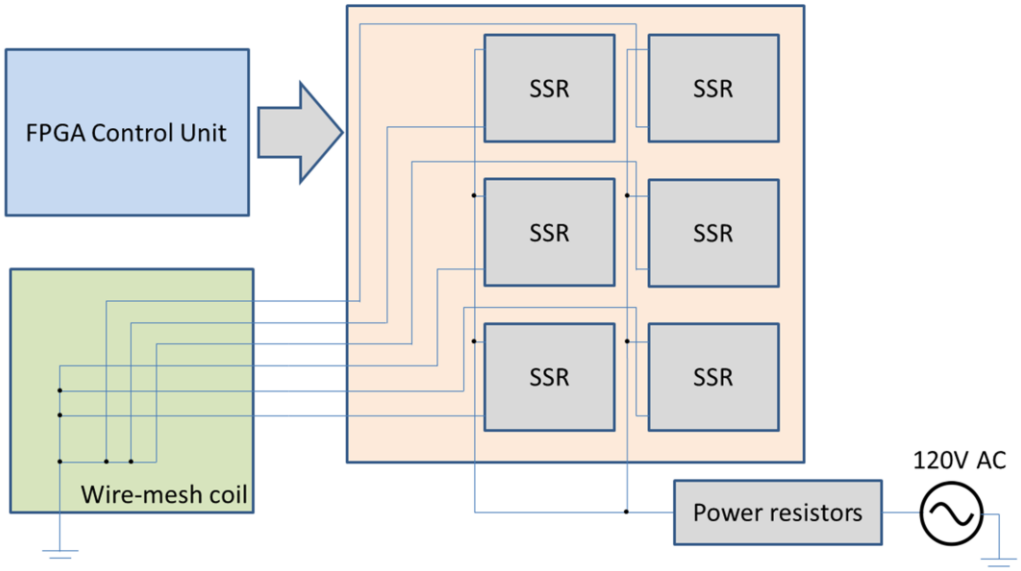

Figure 36: Schematic view of the experiment prototype.

As discussed in Section 3.1, non-magnetic particles can be trapped between two wires conducting opposite-direction currents.

A second wire-mesh coil was fabricated to form a figure-eight pattern when conducting current to trap non-magnetic particles within each branch of the figure-eight pattern.

The micro-fluidic chamber was fabricated from Polydimethylsiloxane (PDMS) on a thin glass flake with 100 μm in thickness. The chamber was filled with ferrofluids and non-magnetic particles 15.7 μm in diameter, and the depth of the ferrofluids-particles mixture was 50 μm.

The chamber was placed onto the wire-mesh coil and observed from the top with a microscope. The volume fraction of the magnetic particles in the ferrofluids is 1.1%. The diameter of the magnetic particles was 10.2 nm with a standard deviation of 1.25 nm.

The magnetic susceptibility of the ferrofluids is 0.05. The non-magnetic particles were spheres with a diameter of 15.7 μm.

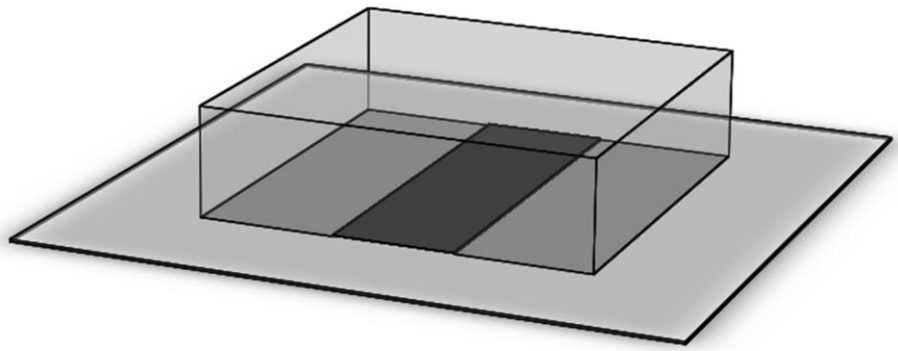

Figure 37: PDMS device for particle motion observation.

The PDMS device shown in Figure 37 was based on a coverslip with thickness 100 μm. A PDMS chamber was stuck on top of the coverslip and filled with the mixture of ferrofluids and non-magnetic particles. The thickness of the chamber was 50 μm. The radius of copper wires in the wire-mesh coil prototype was around 250 μm, so the *z*-directional distance between the current flow and the non-magnetic particles was about 400 μm. The chamber was placed on top of the wire-mesh coil, which was filled with a mixture of ferrofluids and non-magnetic particles. For this experiment, commercial water-based ferrofluids EMG 408 and EMG 605 were used to investigate the influence of magnetic flux density. EMG 605 contains more concentrated ferrous nano particles than EMG 408, as a result, the initial susceptibility and saturated magnetization of EMG 605 is higher than EMG 408. Higher magnetization will result in greater magnetic buoyancy force exerted on non-magnetic particles. However, the viscosity of EMG 605 is 2.5 times

bigger than EMG 408, thus particles in EMG 605 experience greater fluidic drag forces. The motion of non-magnetic particles was observed and recorded by a microscope from the top view.

We tested how well non-magnetic particles could be manipulated with single wire configuration, two parallel wires configuration, three parallel wires configuration, and figure eight coil configuration.

4.2.1 Single Wire Configuration with EMG 408 Ferrofluids

In this experiment, the current conducted through the wire consisted of a series of pulses that were presented repeatedly. Each series was composed of current pulses with 51.2 A in amplitude, 6 ms in duration and a 16.7 ms cycle and each series was presented for 3.6 seconds, after which the wires were allowed to cool down for 2 s. The current flow in the single wire was measured by a Hall Effect current sensor and shown on an oscilloscope while the experiment was conducted.

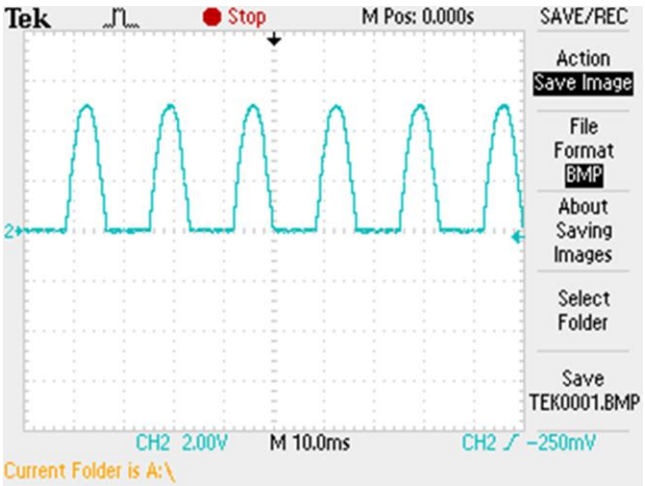

Figure 38: Waveform of serial current pulses conducted to the wire-mesh coil.

The waveform of current pulses captured by Hall Effect current sensor is shown in Figure 38.

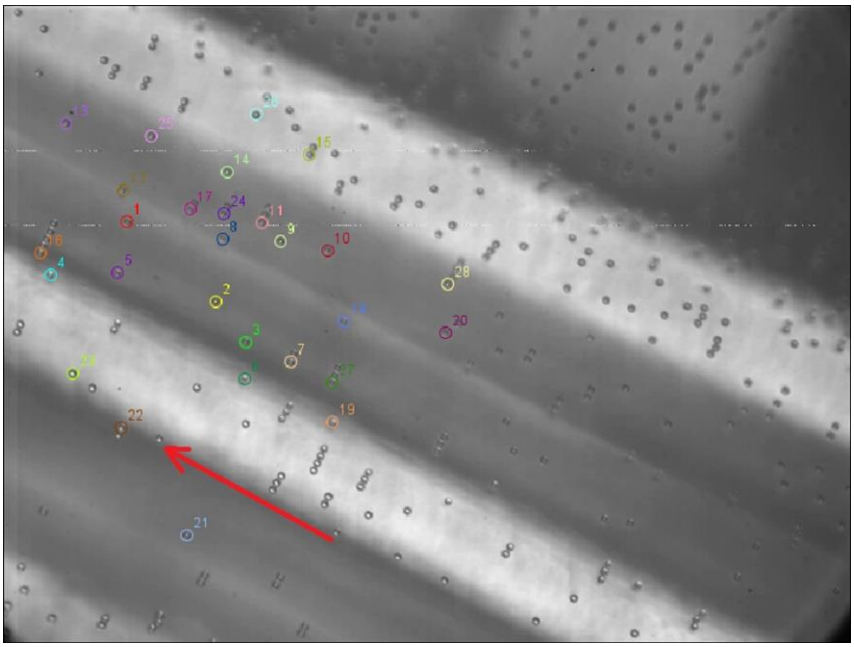

(a)

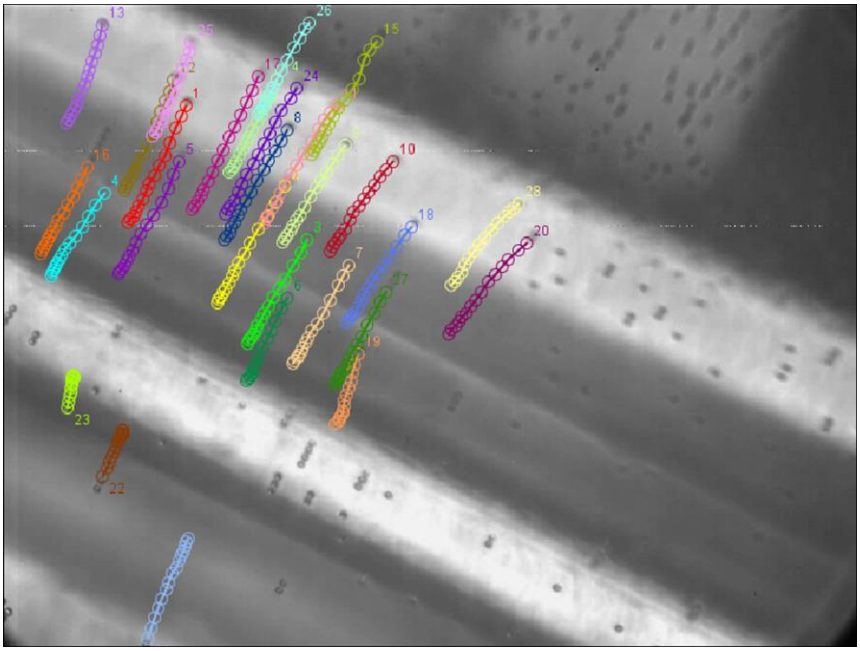

(b)

Figure 39: Motion of non-magnetic particles in single wire configuration.

For the single wire configuration, according to the theoretical analysis and simulation presented previously (see Section 3.1.1), the non-magnetic particles will be pushed away from the single wire. Snapshots of video captured by microscope with 10 time magnification are shown in Figure 39. Part (a) shows the status of non-magnetic particles when we start to conduct current through the single wire (t = 0 s), and the direction of the current is denoted by the red arrow. Twenty-eight particles with different distances from the single wire were marked and tracked. Part (b) shows the motion paths of these 28 particles at the end of the video (t = 3.5 s). From Part (b) of Figure 39 we can see that the non-magnetic particles can be driven to travel across the adjacent wire, so that continuous particle manipulation can be achieved by conducting current through the next wire.

The video was captured at 20 frames/second, thus the duration between two successive frames is 0.05 s. The position of each particle in each frame was captured to calculate the displacements and average velocities of these particles. Motion capture was done using ImageJ, a public domain, Java-based image processing program developed at the National Institutes of Health(http://imagej.nih.gov/ij/). Figure 40 shows a quantitative representation of the motion of the 28 marked non-magnetic particles. The current pulse train starts at t = 0 s and the current train lasts for 3.5 s. The vertical axis of Figure 40 is the distance between the particle and the single wire. From the plot we can see that all particles tend to move away from the wire when the current is on.

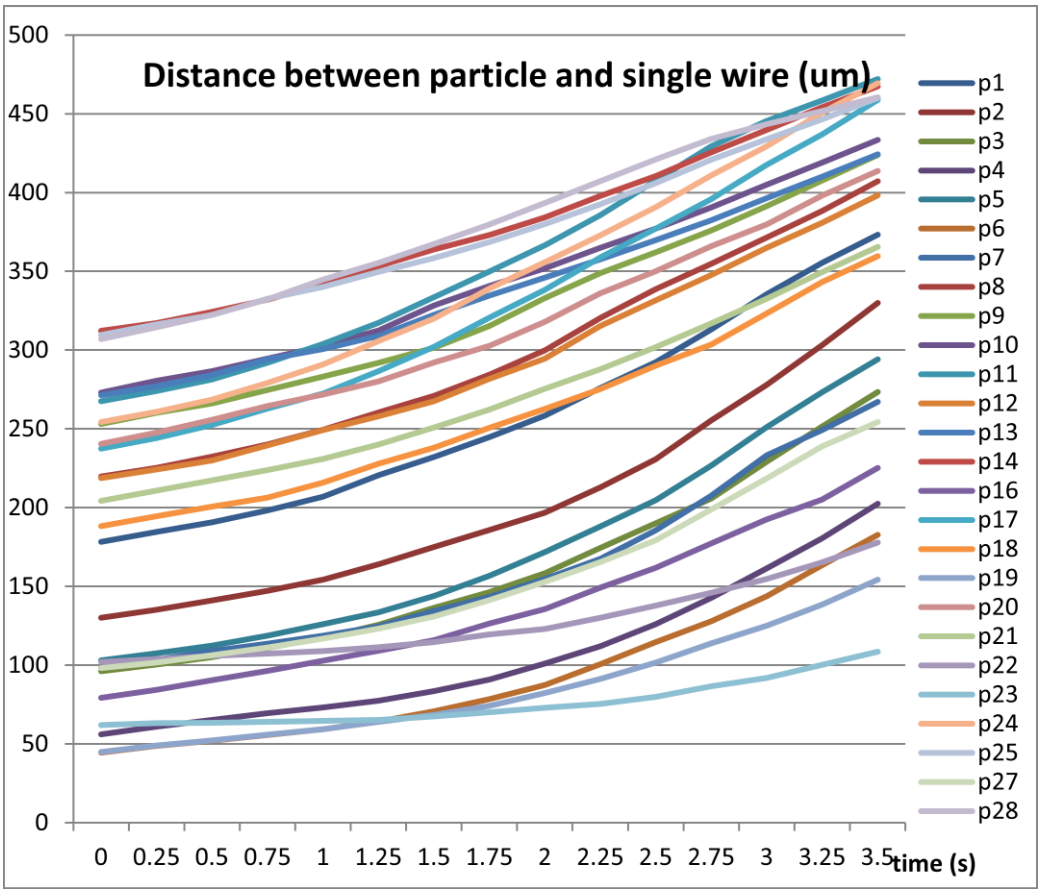

Figure 40: Distance between non-magnetic particles in EMG 408 ferrofluids and a single wire conducting pulsatile current as a function of time.

The total displacement of a particle during the 3.5 s interval depends on its initial position, as shown in Figure 41. The horizontal axis shows the initial distance between the non-magnetic particle and the single wire which conducts current, the vertical axis shows the displacement of non-magnetic particle during the 3.5 s.

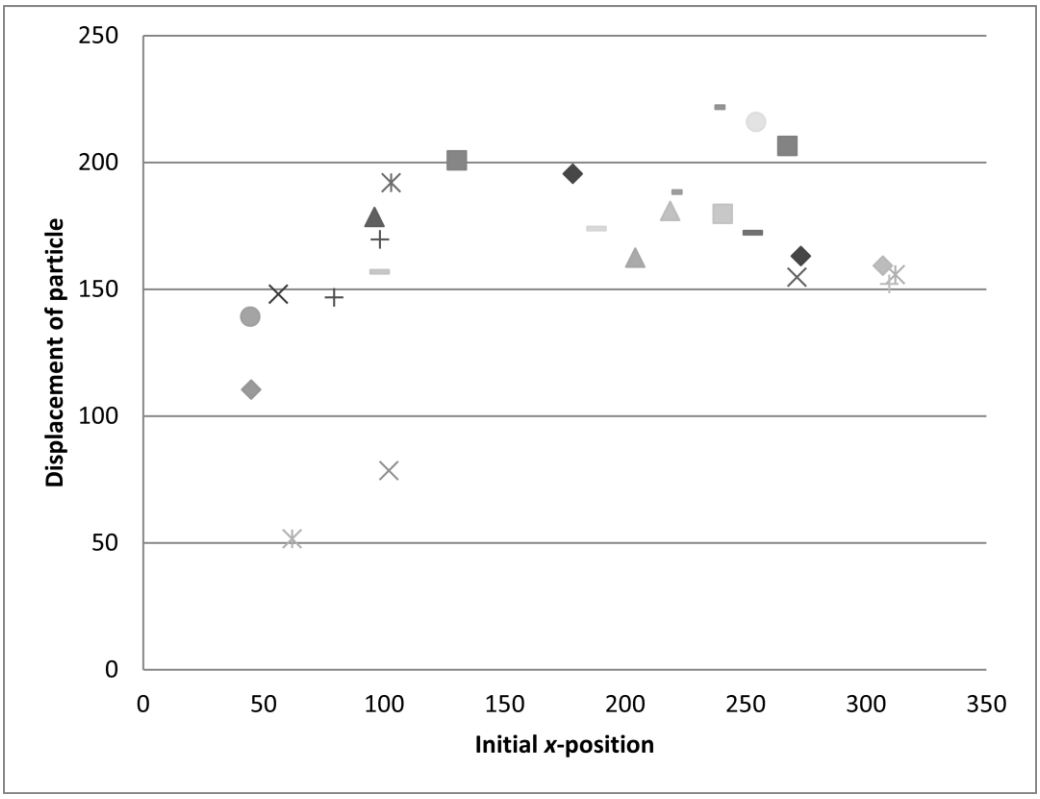

Figure 41: Displacement of non-magnetic particles in 3.6 seconds in response to the serial current pulses.

As discussed in Chapter 3, the magnetic buoyancy force is different for different spatial locations with particles right above ($x = 0$) the single wire experiencing zero force. As the x position of the particle increases, the magnetic buoyancy force exerted on the particle will increase until reaching a maximum value Figure 41 shows that such an effect was observed in practice. The horizontal axis in Figure 41 denotes the initial x-positions of particles relative to the single wire, and the vertical axis shows the displacement of the particles during the 3.6 s that the current pulse train was on. We can see that particles initially in the range from $x = 150$ μm to 250 μm tend to move faster than particles that are initially too close or too far away from the single wire.

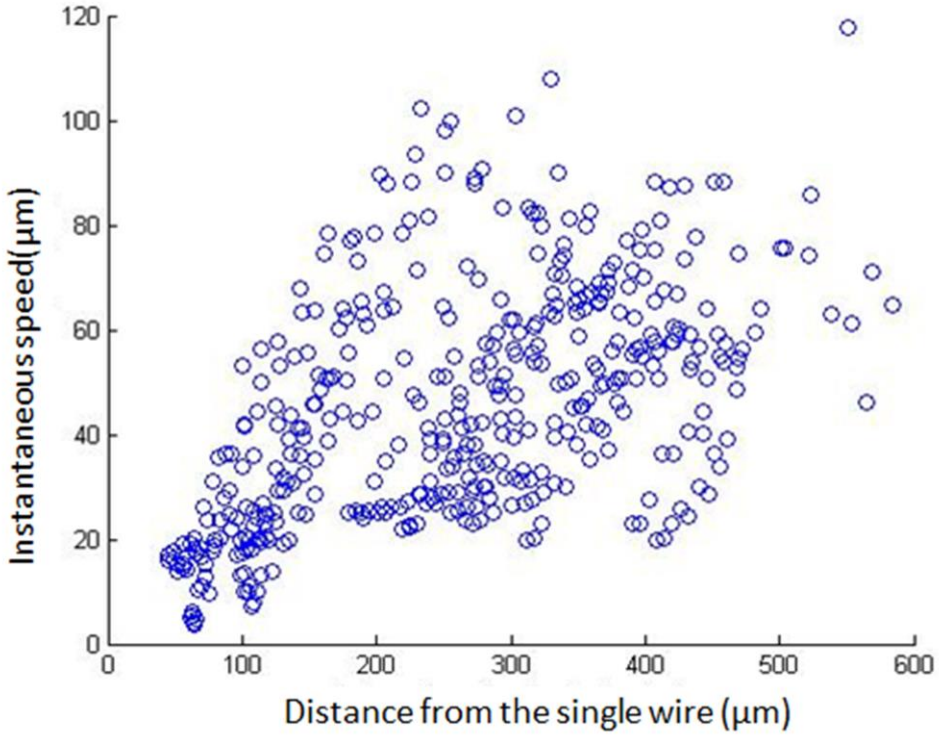

Figure 42: Speed of particles versus *x*-directional location of the particle.

As shown in Figure 42, the speed of non-magnetic particles 100 μm to 600 μm apart from the single wire tends to increase.

4.2.2 Single Wire Configuration with EMG 605 Ferrofluids

In this experiment, the chamber was filled with a mixture of non-magnetic particles and EMG 605 ferrofluids, which has higher saturated magnetization and higher viscosity than EMG 408 ferrofluids. The other experimental conditions remained the same as in Section 4.2.1.

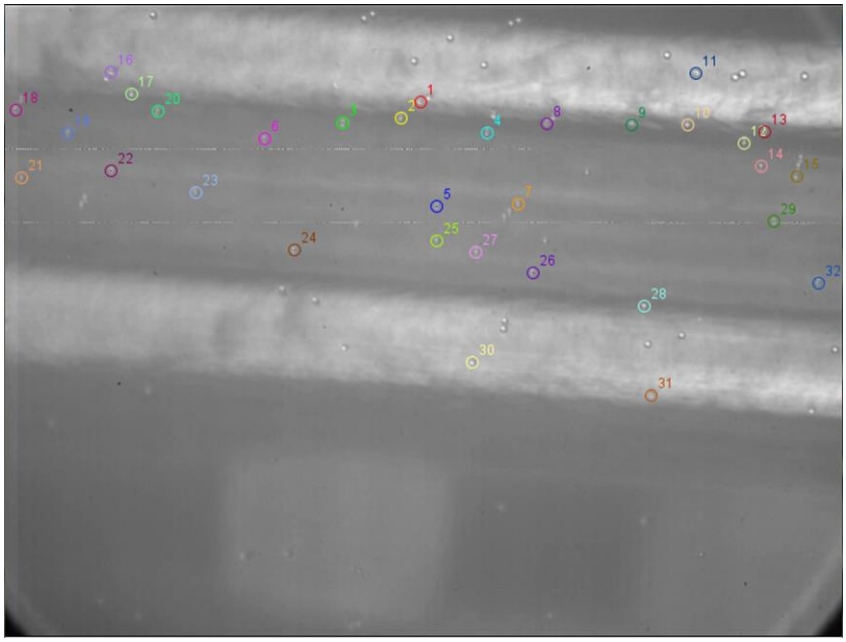

(a)

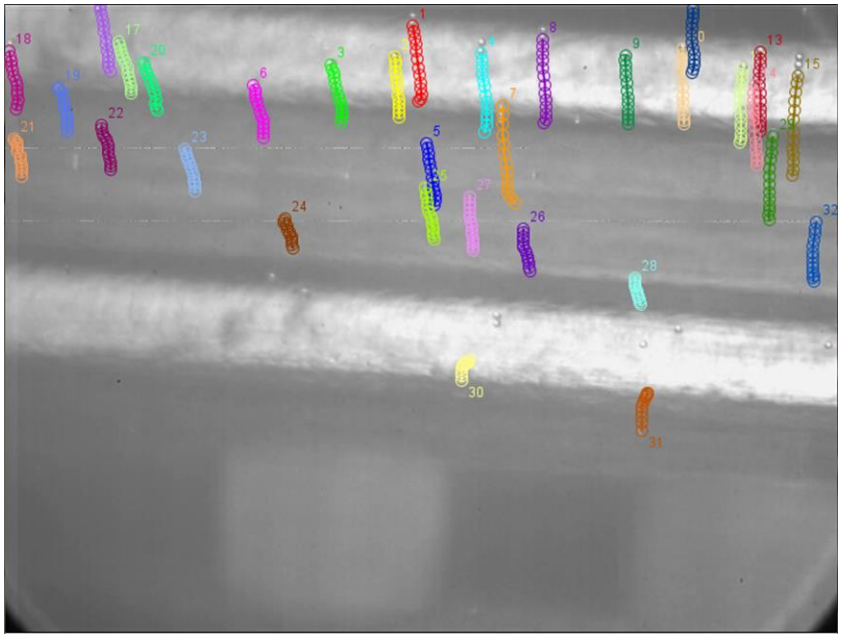

(b)

Figure 43: Motions of non-magnetic particles mixed with EMG 605 ferrofluids in single wire configuration.

Figure 43 shows the motions of 32 non-magnetic particles with different initial

locations as tracked by ImageJ. The positions of these particles were recorded every 5 frames. Figure 44 shows the distance traveled by the non-magnetic particles in EMG 605 ferrofluids during the 3 s while conducting 51 A serial current pulses through a single wire.

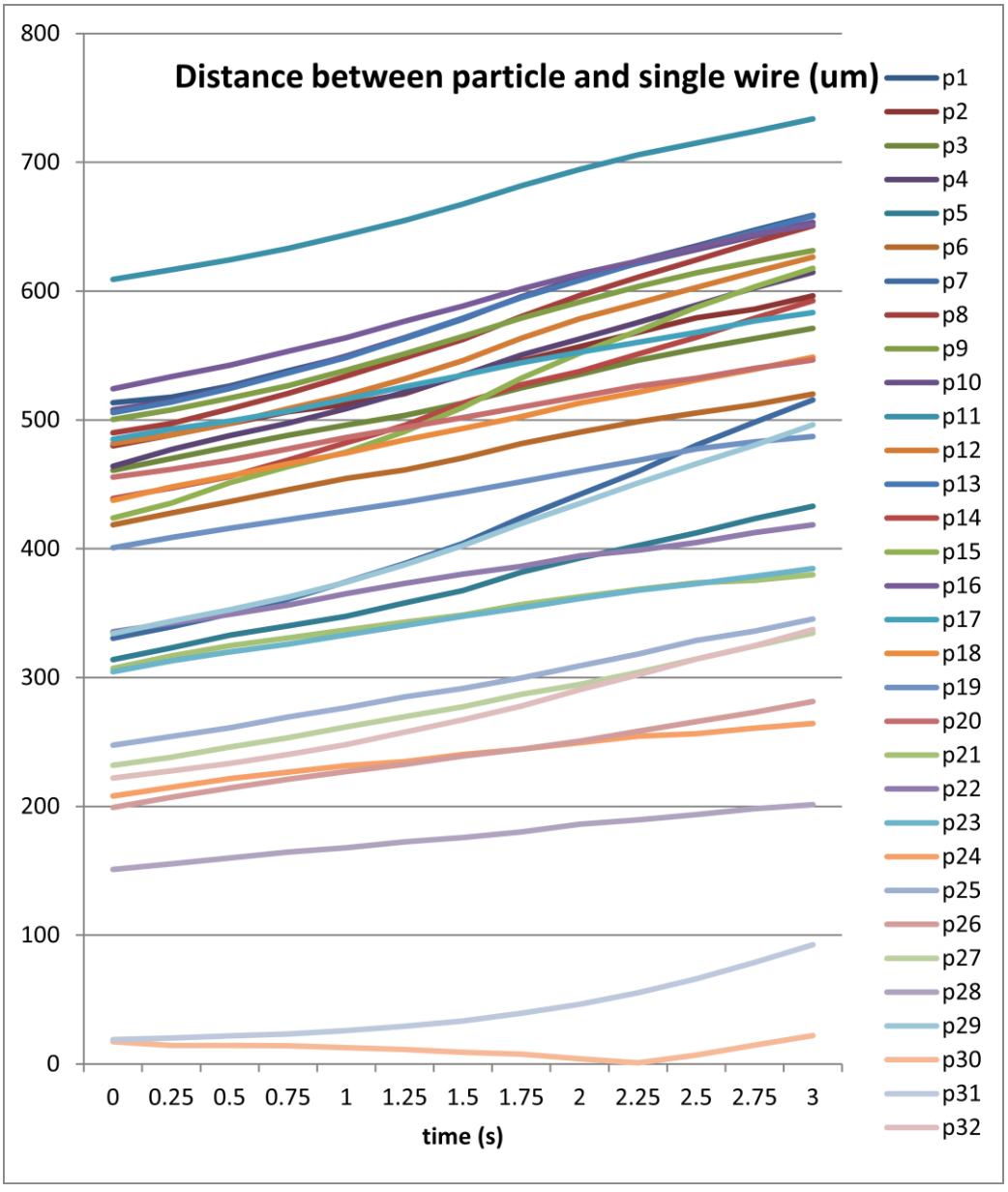

Figure 44: Distance between non-magnetic particles and the single wire in EMG 605 ferrofluids.

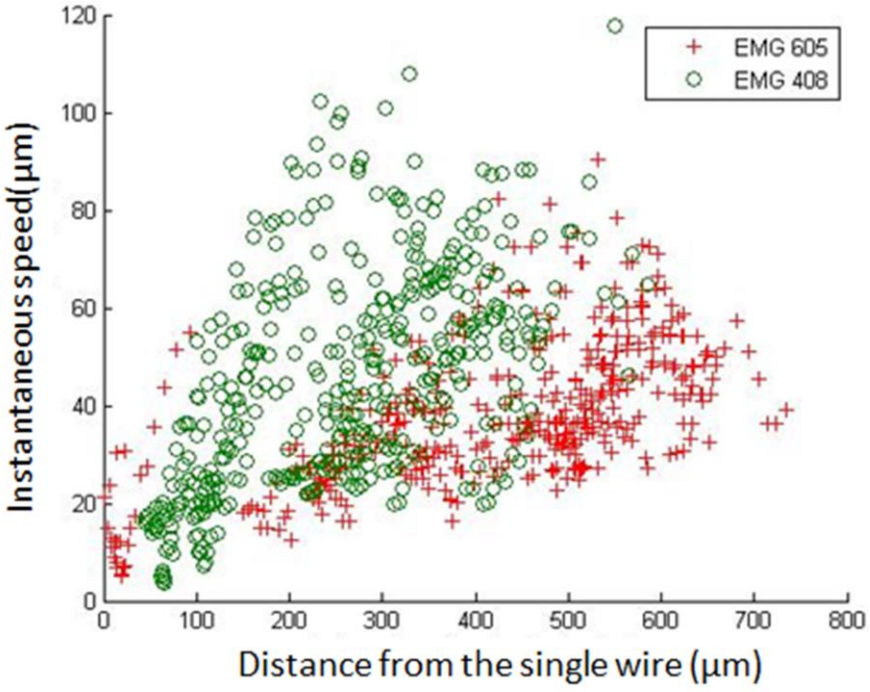

Figure 45: Speeds of non-magnetic particles versus *x*-directional location for EMG 408 and EMG 605 ferrofluids.

The relationship between particle-wire distance and particle's instantaneous speed are plotted in Figure 45 for both EMG 408 and EMG 605. For the same distance from the single wire, particles in EMG 408 ferrofluids move faster than particles in EMG 605 ferrofluids. From the experiment we conclude that EMG 408 ferrofluids shows better performance in particle manipulation.

We also observed that neighboring non-magnetic particles tend to cluster and align during the conducting of current.

4.2.3 Two Parallel Wires Configuration

In this experiment, we conducted current through two adjacent wires in the three–

by-three wire-mesh prototype.

According to the simulation results by COMSOL, the motion of non-magnetic particles depends on the relative directions of the currents in the two wires. The distance between the chamber and wire-mesh coil also affects the ability to manipulate non-magnetic particles. In our experiment, the distance between ferrofluids filled chamber and the wire-mesh coil was 400 μm. According to the simulation result shown in Section 3.1.2, non-magnetic particles between these two wires conducting with opposite directions currents will always be trapped. If the two wires are conducting same direction current, the movement of non-magnetic particles depends on the distance between the chamber and the wire-mesh coil. At distance z = 400 μm, non-magnetic particles will be trapped, but at distance z = 1000 μm, the two parallel wires with same direction currents behaves equivalently to a single wire configuration. Figure 48 shows the motions of non-magnetic particles mixed with EMG 408 ferrofluids in response to two parallel wires conducted with opposite currents. In Part (a) of Figure 46, the vertical white strips are the two copper wires. A series of current pulses with peak amplitude 51.2 Amps were conducted through the two wires with opposite directions for 3 s. Part (b) shows the movement path of the 37 marked non-magnetic particles. We can see that particles between the two wires basically remained stationary during the current conduction phase, while particles outside the wires were moved away.

In conclusion, the two parallel wires configuration does trap the non-magnetic particles as expected.

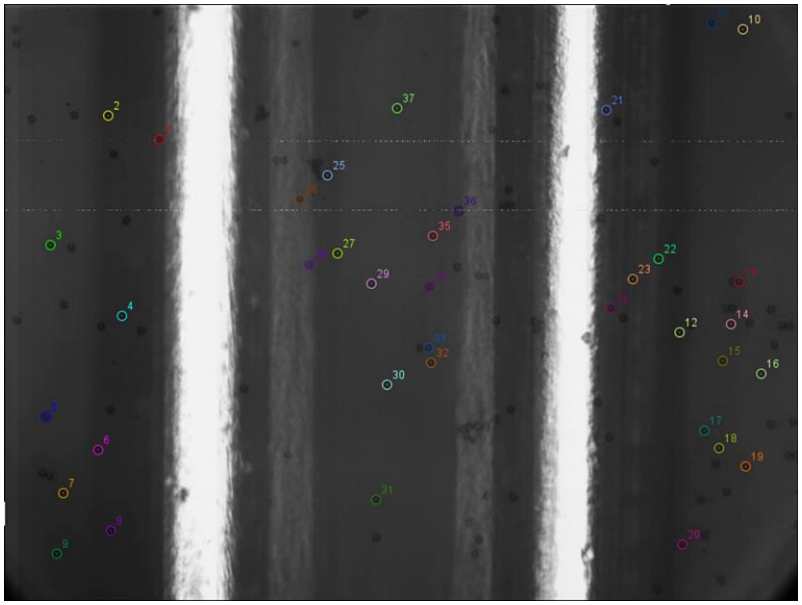

(a)

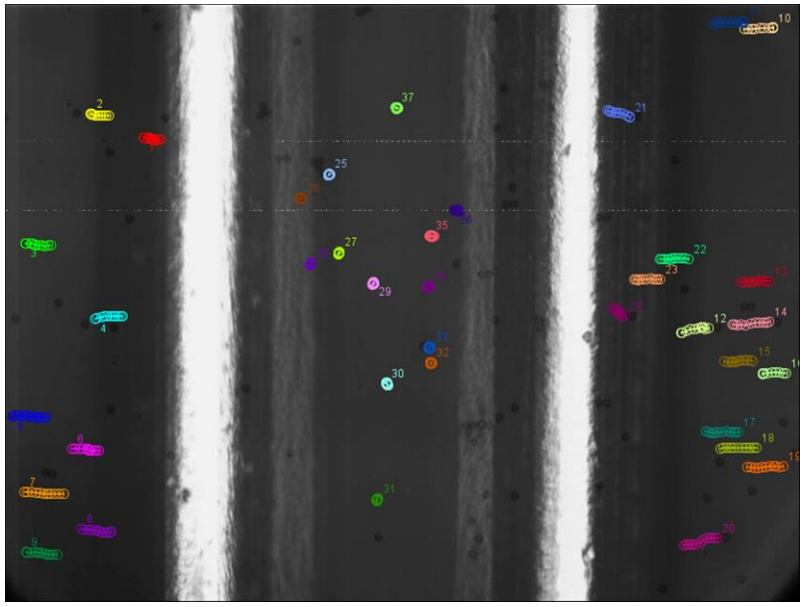

(b)

Figure 46: Motions of non-magnetic particles mixed with EMG 408 ferrofluids in two parallel wires configuration.

4.2.4 Figure-eight Configuration

In this experiment, we conducted currents to three *x*-directional wires and three *y*-directional wires simultaneously with proper direction to form a figure-eight pattern.

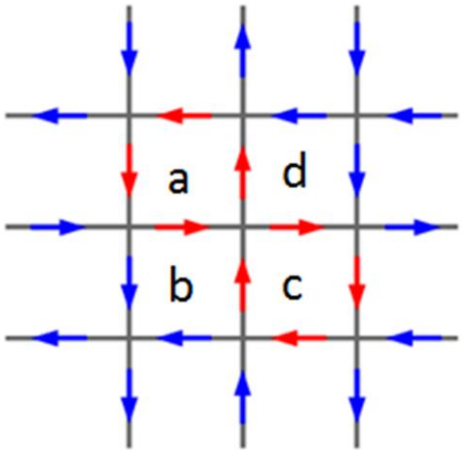

Figure 47: Schematic view of the figure-eight configuration.

Figure 47 depicts the current flow in each channel of the wire-mesh coil, where red arrows form the figure-eight pattern. In the wire-mesh coil prototype, the *y*-directional wires were positioned on top of the *x*-directional wires. According to simulations, non-magnetic particles are supposed to move from grid a, c to grid b, d.

Figure 48 is the x10 microscopic top view of the chamber. The three light grey strips are the three *y*-directional copper wires sitting on the top layer of the wire-mesh coil. The three *x*-directional coppers at the bottom layer are not shown in the picture because they were out of focus.

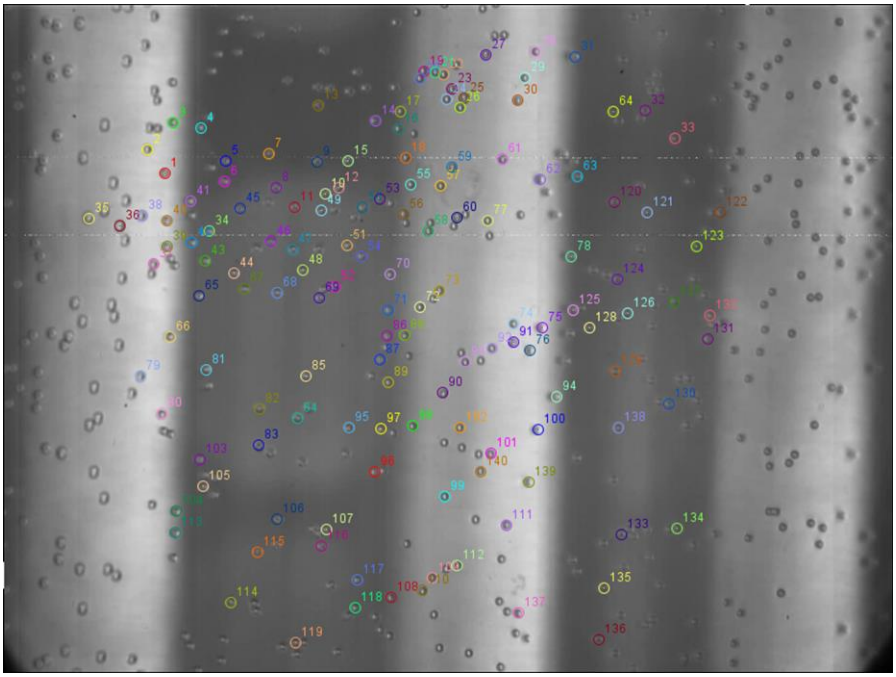

Figure 48: Initial distributions of non-magnetic particles in EMG 408 ferrofluids.

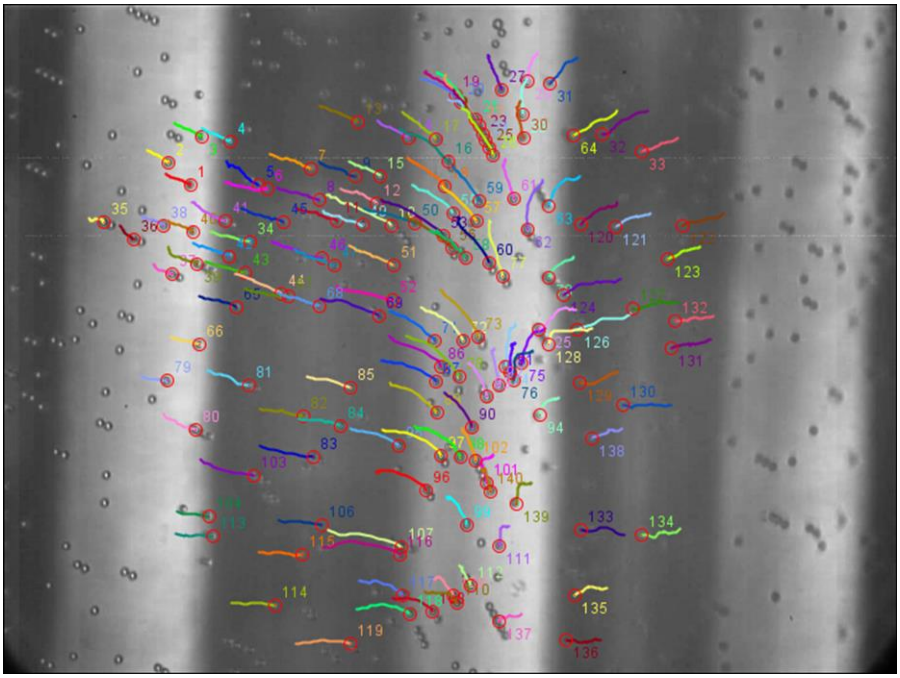

Figure 49: Motion of non-magnetic particles during the 3.6 seconds of current conduction.

We conducted a series of current pulses through the figure-eight wire-mesh coil, with direction of the currents as depicted in Figure 47. From Figure 49 we can see the motion path of the non-magnetic particles during the 3.6 s that current was applied. The colored lines show the path of each particle, the red circles denote the position of particles at the end of the motion, thus we can see that the particles tend to move towards the central wire running in the *y*-direction. Figure 50 shows the distribution of non-magnetic particles in EMG 408 ferrofluids after conducting four series of current pulse, with each pulse train lasting 3.6 s, and around 2 s between successive trains. We can see that, after conducting current pulses for 14.4 s in total, the non-magnetic particles were moved to the center of the *y*-directional wire and were lined up in a slightly oblique pattern along the middle wire.

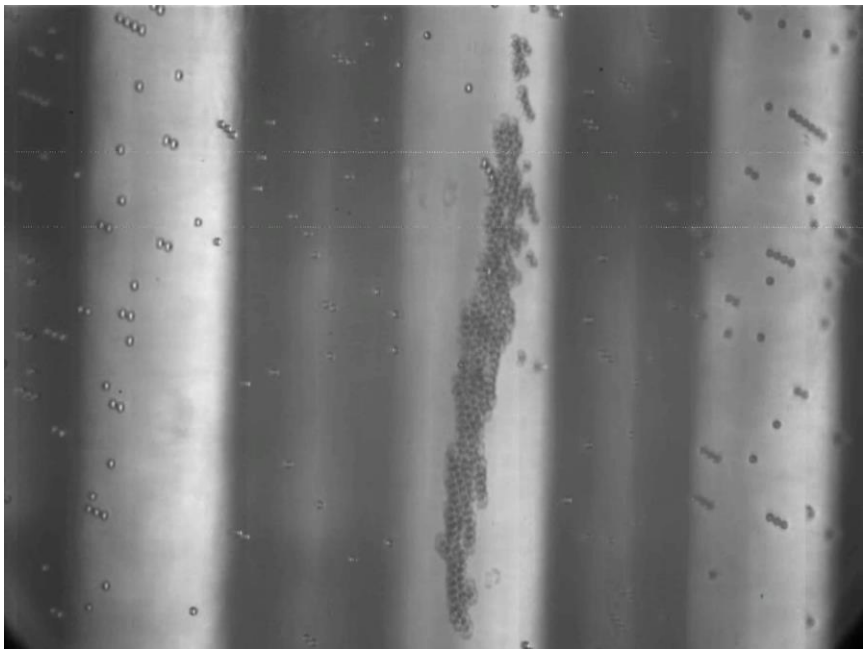

Figure 50: Distribution of non-magnetic particles after conducting serial current pulses for 14.4 s

4.2.5 Ten-by-ten Wire-mesh Testbench

We tested the ten-by-ten wire-mesh coil system as shown in Figure 21, where the copper wire has a cross section of 203 μm x 178 μm. The distance between the chamber and the top layer wire was around 200 μm. A serial current pulse with amplitude 12.8 A was conducted through a single wire of the ten-by-ten wire-mesh coil for 3.6 s. The motion of non-magnetic particles in EMG 408 ferrofluids is shown in Figure 51.

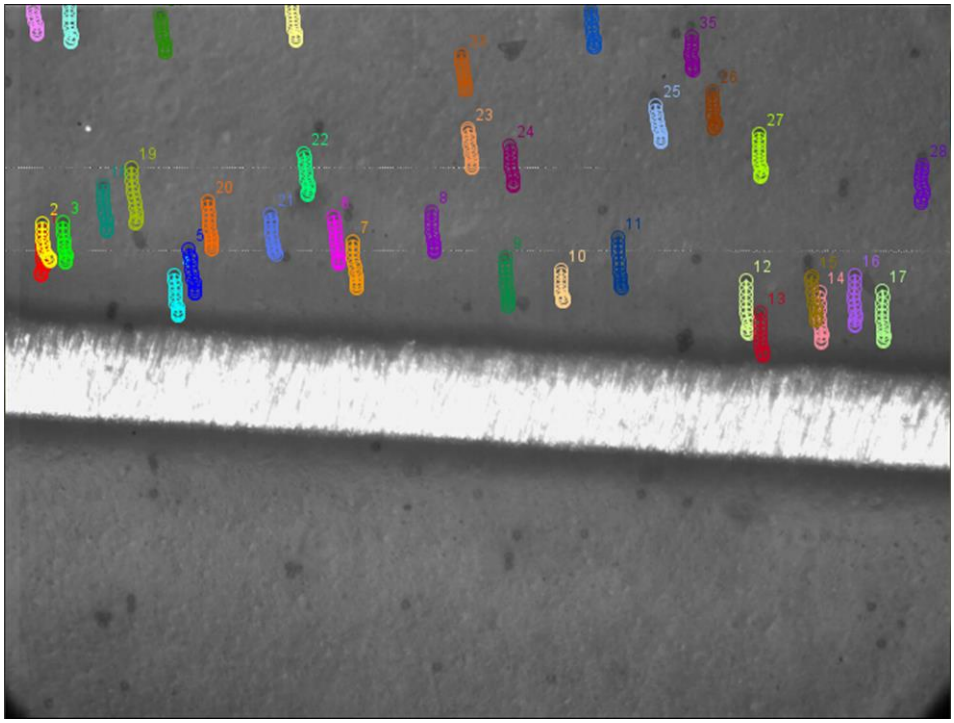

Figure 51: Motion of non-magnetic particles in EMG 408 ferrofluids for ten-by-ten wire-mesh coil testbench during the 3.6 seconds of current conduction.

In contrast to the single wire configuration presented in Section 4.2.1, where the current amplitude I_1 = 51.2 A and distance between chamber and wire z_1 = 400 μm, the current amplitude for the ten-by-ten testbench was I_2 = 12.8 A (four times smaller than I_1), and the distance between chamber and wire was z_2 = 200 μm (half of z_1). The velocity

of the particles in Figure 55 was measured to be around 40 μm/s, which is close to the experimental result of Section 4.2.1. According of Equation (10), non-magnetic particle motion speed is proportional to $\frac{I^2}{z^4}$, in this case, we have $\frac{I_1^2}{z_1^4} = \frac{I_2^2}{z_2^4}$. The experiment result is reasonable.

4.3 Conclusions

In this chapter, we examined the performance of the microfluidic device in manipulating and trapping non-magnetic particles. According to the experimental result, when conducting 51.2 A serial current pulses through the wire mesh coil, we achieved manipulation of non-magnetic particles with the single wire configuration. The non-magnetic particles mixed with EMG 408 ferrofluids were accelerated to speeds within a range from 20 to 100 μm/s, which met our expectation. Then we tried EMG 605 ferrofluids as the media, which has higher saturation magnetization and higher viscosity than EMG 408 ferrofluids. The motion speed of non-magnetic particles in EMG 605 ferrofluids ranged from 20 to 60 μm/s. As a result, EMG 408 ferrofluids is a better choice for particle manipulation.

For two parallel wires experiment, the distance between adjacent wires is 1 mm and the particle filled chamber is put 0.4 mm above the wire-mesh coil. We achieved particle trapping with such configuration.

For figure-eight coil configuration, the particles tend to be attracted to the middle wire of the top layer. Due to the thickness of copper wire, copper wire at the bottom layer of the wire-mesh coil has less effect on the non-magnetic particles. The motion of the particles is dominated by the current in the top layer.

Chapter 5 Discussion and Future Work

5.1 Discussion

The main goal of this research was to achieve particle manipulation and particle trapping with a microfluidic wire-mesh coil system and performing quantitative analysis of the experimental result.

We started with defining the specification of the device such as the scale of the wire-mesh coil, the microfluidic chamber, and set an objective rate for particle manipulation. Secondly we built a mathematical model for the magnetic field generated by the wire-mesh coil and motion of non-magnetic particles driven by magnetic buoyancy force and fluidic drag force. With this theoretical analysis we verified the feasibility of the design. Then we performed finite element method simulation on particle motion and wire heat dissipation. The simulation results turn out to be matched to the theoretical analysis. Based on this, we designed and implemented the electrical circuits for switching current pulses to each channel of the wire-mesh coil system. Bench experiments were performed to test the performance the microfluidic device for manipulating non-magnetic particles. While no tests with actual cells were conducted, cancer cells tend to be spherical in shape when they are suspended in a bio-compatible medium (Zhu et al., 2011), just like the non-magnetic particles we used in experiment. However, when contacting the surface of the chamber, cancer cells become flat. To minimize this, the chamber is pre-processed to increase its hydrophilic property to prevent cells from sticking to the surface of the chamber.

Several phenomena about the movement of non-magnetic particles were observed

and are discussed next.

Consider the magnetic buoyancy force for the single coil configuration shown by Equation (6). The horizontal component of the force will reach a maximum at position $x = x_m$. The value of x_m can be determined by finding the zeros of the partial derivative of Equation (6) with respect to x, which is:

$$\frac{\partial F_{m,x}}{\partial x} = \frac{V\chi_m I^2 \mu_0}{4\pi^2 \mu_r{}^2} \frac{(x^2+z^2)^3(z^2-3x^2)}{(x^2+z^2)^6}.$$

By setting the partial derivative of horizontal magnetic buoyancy force to be zero, we can get the position of maximum force $x_m = \frac{\sqrt{3}}{3} z$, where z is the distance between the single copper wire and the chamber. As a result, the horizontal position of the maximum magnetic buoyancy force varies linearly with z. This result can be applied to determine the optimal size of the wire-mesh coil system and the distance between the chamber and the wires. Assuming that the chamber is z. = 400 μm away from the wire-mesh coil, the optimal distance between adjacent wires is $d = x_m \approx 231\mu m$. Because a single wire exerts zero x-directional magnetic buoyancy force to the particle right above it, this blind spot can be compensated by the adjacent wires.

In Section 3.1.3, the RMS value of the current pulses train shown by Equation (19) was used to determine the amount of heating. Consider two different current pulses, $i_1(t)$ and $i_2(t)$, with the same RMS value, i.e., $\int_0^T i_1{}^2(t)dt = \int_0^T i_2{}^2(t)dt$, where T is the cycle of the current pulses train. According to Equation (10), the speed reached by a non-magnetic particle is proportional to the square of current. Since the acceleration and de-acceleration period are much shorter than the duration of the pulse, we can assume that

different current pulses with same RMS will have the same effect on particle motion.

For the three-by-three prototype testbench, we used copper wires with section radius 250 μm. Without applying cooling system to the wire-mesh coil, the wires can tolerate 4 successive 51.2 A current pulses trains, 3.6 s each, without burning out. When two adjacent wires are conducting current simultaneously, there will be Ampere forces between the two wires to make them either attract or repel each other. As a result, the wires need to be fixed to the substrate to avoid them from bending during the experiment.

During the particle manipulation process, about 10% of the non-magnetic particles remained stationary. These particles were mostly located near the current flow. This phenomenon is caused by the *z*-directional magnetic buoyancy force, which pushes the non-magnetic particles upward to the top of the chamber. As particles move near the chamber's surface, they experience increased fluid viscosity (Equation 15), which impedes their motion in the *x*-direction. Although the chamber was pre-processed by plasma before use to reduce the interaction between the particle and the wall, this phenomenon still occurred.

When the wire-mesh coil is conducting current, neighboring non-magnetic particles in the chamber tend to agglomerate and align to a direction which is perpendicular to the current flow. Non-magnetic particles confined in ferrofluids are denoted by magnetic holes, they agglomerate due to dipolar interactions when an external magnetic field is exerted (Geir et al., 2004). As show in Figure 51, the movement path of non-magnetic particles marked with number 20 and 24 were deflected due to their nearby particles. They approached and stuck to another particle and continued to move as a group.

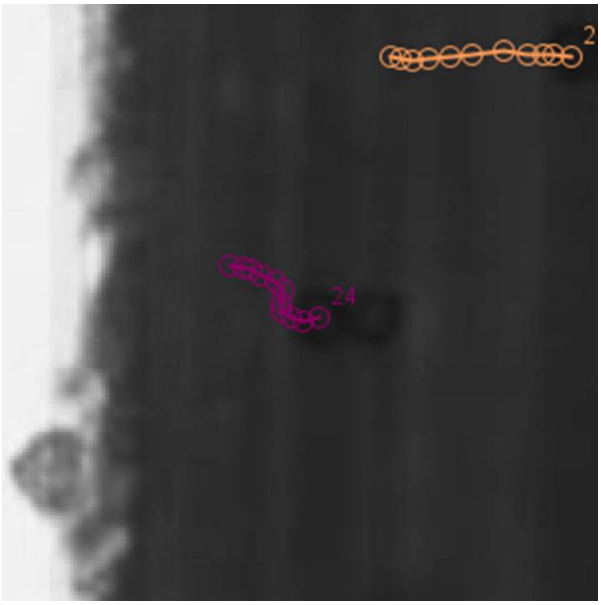

(a)

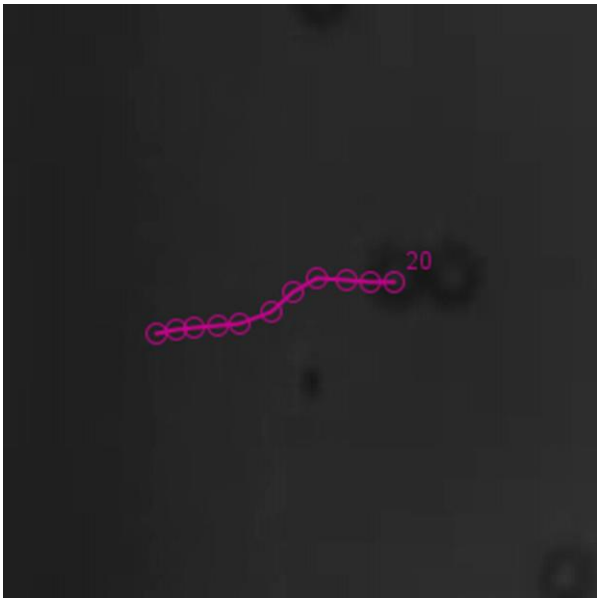

(b)

Figure 52: Agglomeration of non-magnetic particles during the motion.

It was also observed that when several particles align as a column and move together, their motion will be faster than that of single particles when other conditions are the same.

(a)

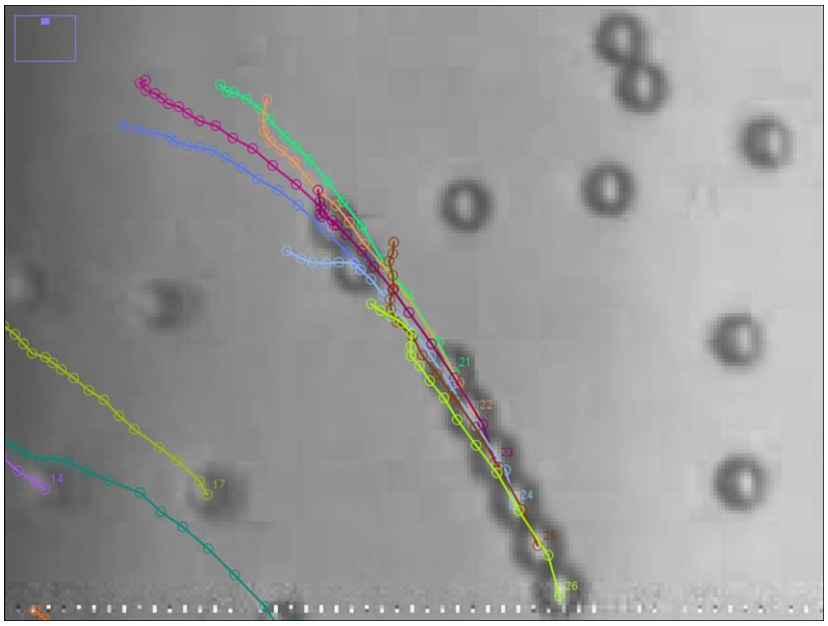

(b)

Figure 53: Agglomeration of non-magnetic particles during the motion. (a) t = 0s, (b) t = 3.6 s.

Figure 53 shows the motion of several non-magnetic particles captured in the

experiment with the figure-eight configuration. From Figure 53, we can see that particles 19, 20 and 21 – 26 were grouped to form a line during the motion. After alignment, the group motion speed was increased because fluidic drag force is proportional to the radius of the cross area of particles normal to the relation movement direction, and when particles form a line, their cross area remains small. So there is less fluidic drag force that impedes the motion.

For the figure-eight configuration of the wire-mesh coil, we conducted current pulses trains to three *x*-directional and three *y*-directional wires with directions as shown in Figure 54. Peak values of the magnetic flux density occur at the two branches of the figure-eight pattern. Since non-magnetic particles tend to move along the opposite direction of magnetic flux density, which is shown in Figure 54 by blue arrows, we expect that, for figure-eight configuration, the non-magnetic particles inside the figure-eight pattern will be moved out and enter the top right and bottom left grid of Figure 54.

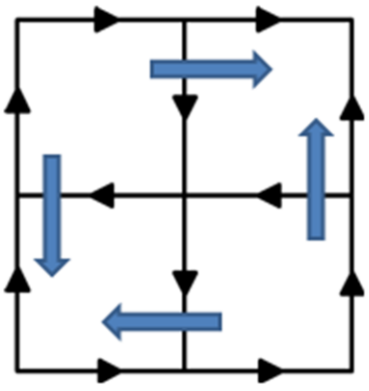

Figure 54: Black arrows denote the current flow in the figure-eight pattern, blue arrows denote the motion directions of non-magnetic particles due to magnetic buoyancy force.

This analysis was verified by finite element method simulation using COMSOL. As shown in Figure 55, where the arrows denote the movement directions of non-magnetic particles, the particles will move away from the two branches of the figure-eight pattern. As a result, this configuration can be used to move particles from one grid to another.

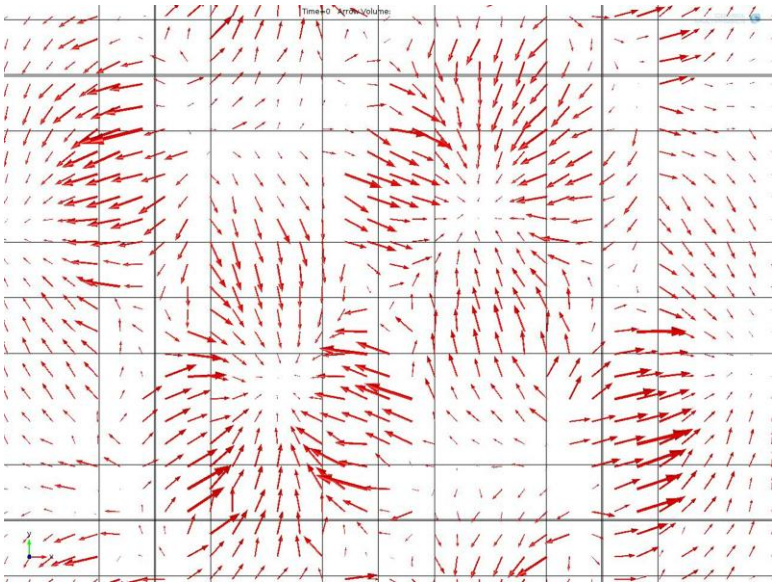

Figure 55: Simulation of non-magnetic particles motion by COMSOL for figure-eight configuration.

However, the experimental result for the figure-eight configuration did not match the analytical and simulation results. One explanation may be that the simulation shown in Figure 55 assumes that the two layers of wire-mesh coil are in the same plane, while in actuality the bottom layer of the wire-mesh coil is farther away from the chamber, and its effect on the non-magnetic particles will be small compared to the top layer. This was tested by the simulation shown in Figure 56, which presents the magnetic buoyancy force distribution in the *x*-*y* plane when the two layers of the wire-mesh coil are 600 μm apart, with the *y*-directional wires sitting on the top layer. We can see that the non-magnetic

particles within the range of three-by-three wire-mesh tend to move towards the middle vertical wire. This simulation matches the experimental result for figure-eight configuration (Figure 50).

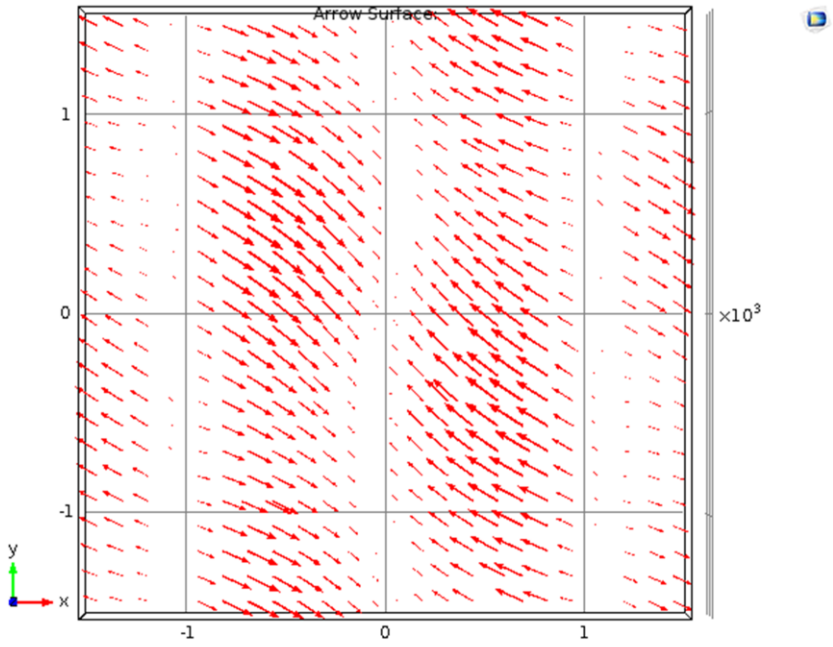

Figure 56: Real case simulation of non-magnetic particles motion by COMSOL for figure-eight configuration. The directions of the magnetic buoyancy force on non-magnetic particles are shown by the red arrows. The three-by-three wire mesh is depicted by the grey dashed lines.

For the ten-by-ten wire-mesh coil bench experiment, the copper wires in the testbench were too thin to sustain the 12.8 A current pulses train. When we conducted the second current pulses train to the ten-by-ten wire mesh coil, the single wire burned out. We need to increase the cross-sectional area of the ten-by-ten wire-mesh coil in future work. Stacking wires vertically will be helpful for reducing the total resistance of the wire, thus reducing heating.

The micro-fluidic mesh-wire coil device can be applied to sort non-magnetic

particles based on their sizes. This is achieved because a non-magnetic particle experiences a magnetic buoyancy force that is proportional to its volume, and a fluidic drag force proportional to its radius. As a result, non-magnetic particles with the same density but varying in size will move at different velocities, with bigger particles moving faster than smaller ones, thus allowing for particle sorting based on size.

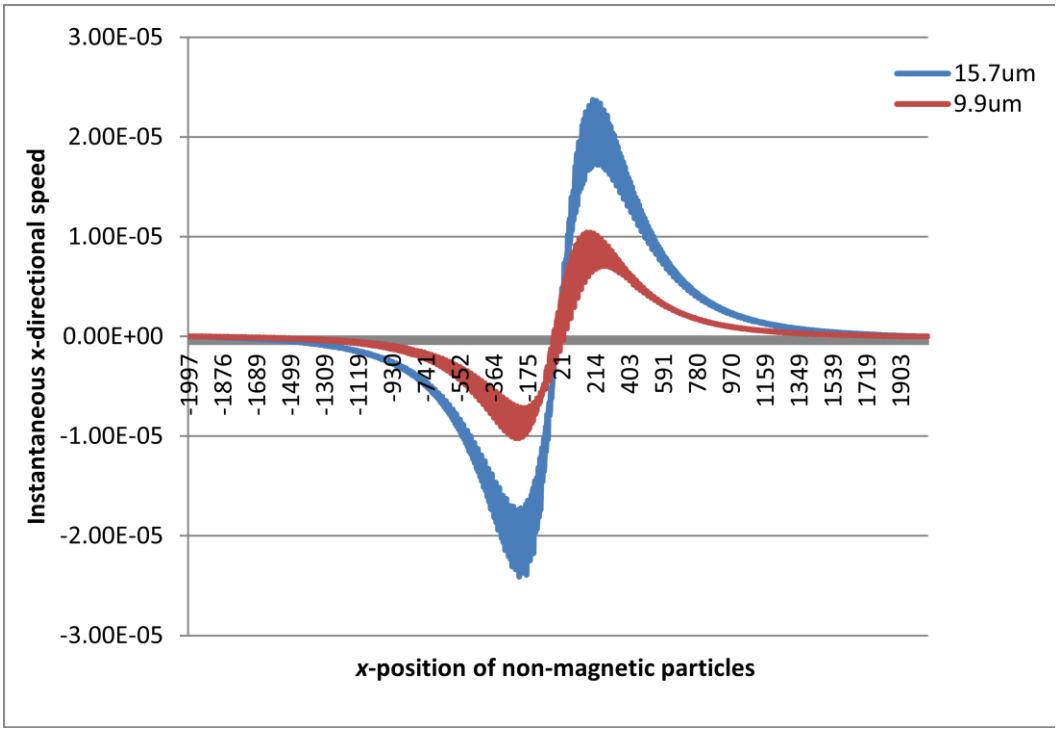

Figure 57: Instantaneous *x*-directional speed of non-magnetic particles of different sizes in ferrofluids for single wire configuration.

The motion of non-magnetic particles of different sizes in response to a magnetic field generated by the single wire configuration were simulated by COMSOL. Figure 57 shows the instantaneous *x*-directional speed of particles wire sizes 9.9 μm and 15.7 μm in diameter. We can see that bigger particles move more than two times faster. Separation can be achieved based on the difference of displacements of particles with different sizes.

Since the train of current pulses produces a time varying magnetic field, an electric field will also be generated. This could exert a dielectophoresis force on non-magnetic particles. The time varying electric field is caused by the AC component of the current pulses train. The train of current pulses can be treated as a periodic signal, with a single period (current pulse) as shown in Figure 58 and a power spectrum as shown in Figure 59.

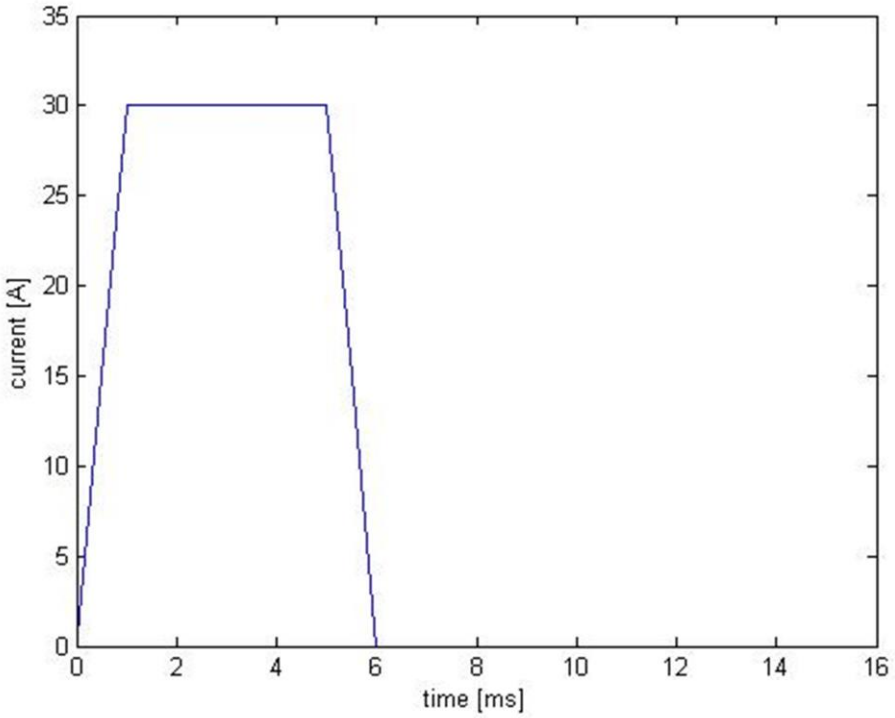

Figure 58: Mathematical model of the current pulse, which has 30 A peak value and ~1 ms transition zone according to the experiment result.

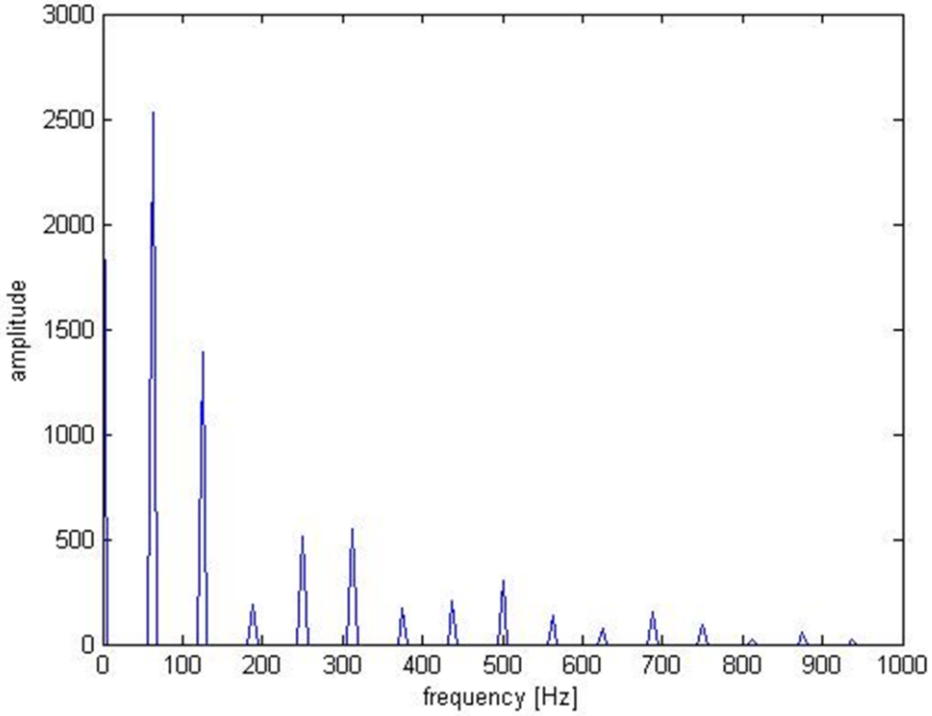

Figure 59: Power spectrum density of the current pulses train. Majority of the power is concentrated at DC (does not induce electric field) and AC frequencies at 62.5 Hz, 125 Hz, 250 Hz and 312 Hz.

Frequency domain simulation with the major frequencies as shown in Figure 59, demonstrated that the peak value of the normalized induced electric field in the chamber is around 0.04 V/m, which is far smaller than the 50 kV/m electric field needed to manipulate dielectric particles (Thomas et al., 2007). In summary, the time varying electric field caused by the current pulses train is too small to affect the motion of non-magnetic particles.

5.2 Suggestions for Future Work

The observations and findings in the experiments confirm the theoretical analysis on the motion of non-magnetic particles in ferrofluids for single wire, two parallel wires

and three parallel wires configurations. However, the performance of the figure-eight coil is limited because the wires in the bottom layer are too far away from the chamber and they have much less effect on the motion of the non-magnetic particles. In future work, we will manage to address this problem. One approach is depicted in Figure 60, which shows an alternative design of the microfluidic chip. The two layers of the wire-mesh coil are fabricated on two sides of the substrate respectively. The chamber is made of PDMS layer (50 μm in thickness) sandwiched by two pieces of cover glass (100 μm in thickness each). The total thickness of the chamber will be around 250 μm. The chamber is placed inside the substrate, between the two layers of the wire-mesh coil. With this design, the ferrofluids-particle mixture will be essentially in the middle of two layers of wires so that the two layers will have the same effect on particle manipulation.

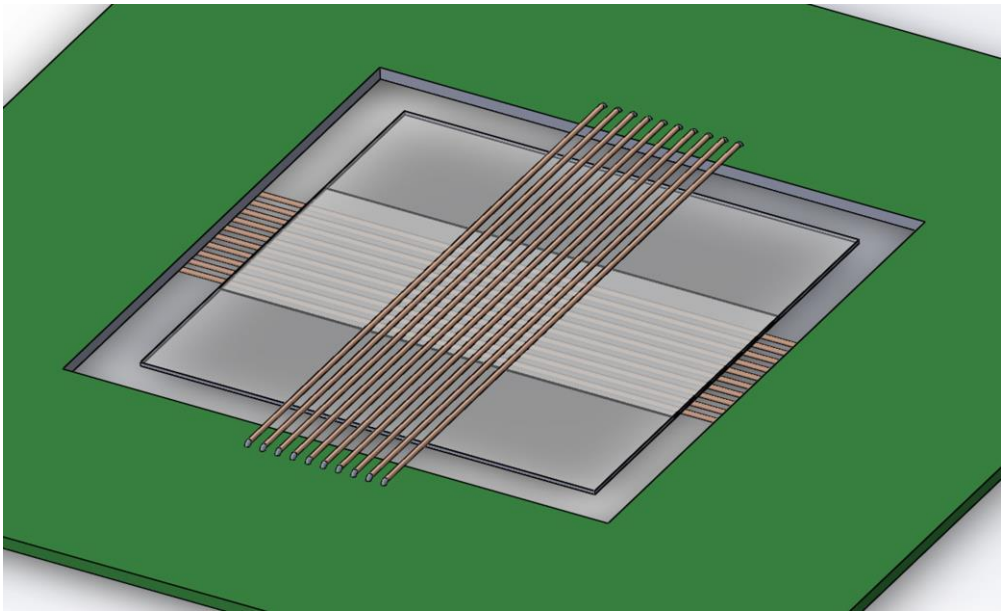

Figure 60: Schematic of the chip displaying one microfluidic chamber placed between two layers of the wire-mesh coil.

In the experiment we used AC power supply to deliver current pulse to the wire-

mesh coil. However, The output of AC source fluctuating, to output stable current pulse is to use a DC power source, which can provide a DC voltage as large as the peak value of the AC power source. Such a DC power source can be achieved by applying a bridge rectifier and a regulator to the 120V AC power source. Figure 61 shows the schematic view of the AC to DC circuit.

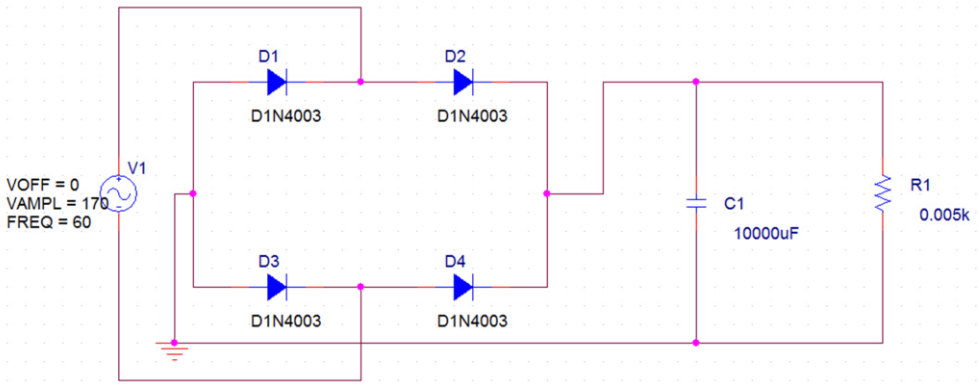

Figure 61: Schematic view of AC to DC circuit.

This circuit converts the 120V AC waveform to DC. When AC source V1 is on its positive half, diodes D2 and D3 are set into conductive mode, and the current flows down through the load resistor R1 and via D3 back to the load. For the negative half of V1, diodes D1 and D4 are in conductive mode, and the current also flows via D4 through R1 and D1. As a result, diodes D1-D4 form a bridge rectifier to convert the input AC sinusoidal waveform to positive polarity at its output.

Capacitor C1 works as a regulator to stabilize the voltage so as to generate a DC output. In Figure 62, the green curve is the input AC waveform, which is a sinusoidal 60 Hz wave with peak value of 170V. The red curve depicts the output ‘DC’ voltage.

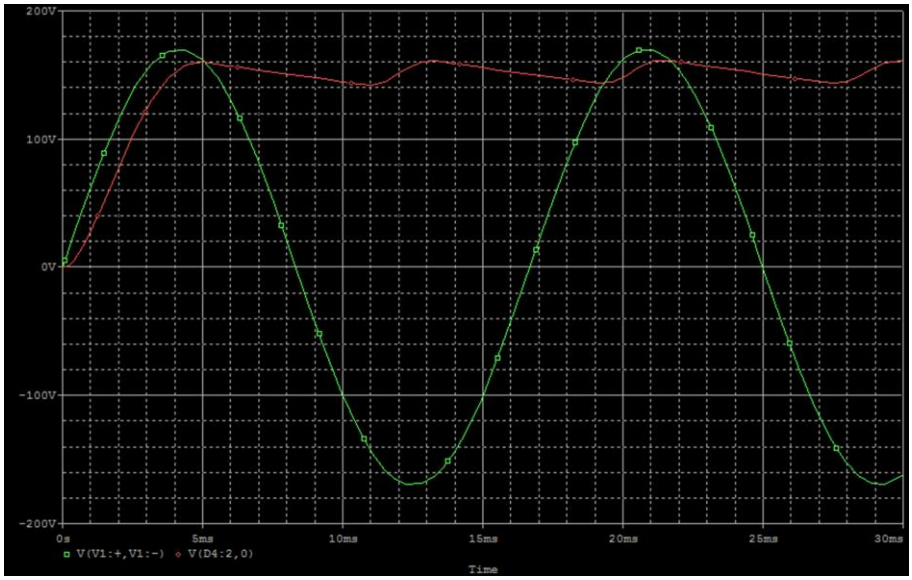

Figure 62: waveform of the AC input and DC output.

As we can see from Figure 62, when the waveform of AC power source is declining, the charge stored in the capacitor tends to maintain the output voltage. The time constant for the discharge process is $\tau = RC$, which is the time required for the voltage to fall to $\frac{V_0}{e}$. The bigger the time constant is, the cleaner the DC output we will get. Since we expect to conduct 30 A current in the wire-mesh coil, the resistance of the whole loop should be really small (about 5 ohms). As a result, a big capacitor is required. The capacitor for the simulation in Figure 61 is 10,000 μF. An Altera DE2 FPGA board is applied to deliver control signals to the switching unit.

References

Anttila, A., Pokhrel, A., Kotaniemi-Talonen, L., Hakama, M., Malila, N., & Nieminen, P. (2011). Cervical Cancer Patterns with Automation-assisted and Conventional Cytological Screening: A Randomized Study. *Int J Cancer, 128*, 1204-12.

Balvin, M., Sohn, E., Iracki, T., Drazer, G., & Frechette, J. (2009). Directional Locking and the Role of Irreversible Interactions in Deterministic Hydrodynamics Separations in Microfluidic Devices. *Phys Rev Lett, 103*(078301).

Bonner, W. A., Hulett, H. R., Sweet, R. G., & Herzenberg, L. A. (1972). Fluorescence Activated Cell Sorting. *Rev Sci Instrum, 43*, 404-9.

Cho, Y. K., Lee, J. G., Park, J. M., Lee, B. S., Lee, Y., & Ko, C. (2007). One-step Pathogen Specific DNA Extraction from Whole Blood on a Centrifugal Microfluidic Device. *Lab Chip, 7*, 565-73.

Cronje, H. S. (2004). Screening for Cervical Cancer in Developing Countries. *Int J Gynaecol Obstet*, 101-8.

Crydom. (2010). How to Bench Test a Solid State Relay.

Davis, J. A., Inglis, D. W., Morton, K. J., Lawrence, D. A., Huang, L. R., Chou, S. Y., Sturm, J. C., Austin, R. H. (2006). Deterministic Hydrodynamics: Taking Blood Apart. *Proc Natl Acad Sci U S A, 103*, 14779-84.

Easley, C. J., Karlinsey, J. M., Bienvenue, J. M., Legendre, L. A., Roper, M. G., Feldman, S. H., Landers, J. P. (2006). A Fully Integrated Microfluidic Genetic Analysis

System with Sample-in-answer-out Capability. *Proc Natl Acad Sci U S A, 103*, 19272-7.

Gadish, N., & Voldman, J. (2006). High-throughput Positive-dielectrophoretic Bioparticle Microconcentrator. *Analytical Chemistry, 78*, 7870-7876.

Ganatos P., P. R. (1980). A Strong Interaction Theory for the Creeping Motion of a Sphere Between Plane Parallel Boundaries 2. Parallel Motion. *J Fluid Mech*, 755–783.

Geir Helgesen, A. T. (2004). Aggregation Dynamic of Non-magnetic Particles in a Ferrofluid. *Physical Review*.

Gijs, M. A., Lacharme, F., & Lehmann, U. (2010). Microfluidic Applications of Magnetic Particles for Biological Analysis and Catalysis. *Chemical Reviews, 110*, 1518-1563.

Gossett, D. R., Weaver, W. M., Mach, A. J., Hur, S. C., Tse, H. T., Lee, W., Amini, H., Di Carlo, D. (2010). Label-free Cell Separation and Sorting in Microfluidic Systems. *Analytical and Bioanalytical Chemistry, 397*, 3249-3267.

Grier, D. G. (2003). A Revolution in Optical Manipulation. *Nature, 424*, 810-6.

Hafeli, U., Schutt, W., Teller, J., & Zborowski, M. (1997). Scientific and Clinical Applications of Magnetic Carriers. *Springer: New York*.

Huang, L. R., Cox, E. C., Austin, R. H., & Sturm, J. C. (2004). Continuous Particle Separation Through Deterministic Lateral Displacement. *Science, 304*, 987-90.

Hunt, T. P., Issadore, D., & Westervelt, R. M. (2008). Integrated Circuit/microfluidic Chip to Programmably Trap and Move Cells and Droplets with Dielectrophoresis. *Lab on a Chip, 8*, 81-87.

Jacobson, S. C., McKnight, T. E., & Ramsey, J. M. (1999). Microfluidic Devices for Electrokinetically Driven Parallel and Serial Mixing. *Anal Chem, 71*, 4455-4459.

Kitchener, H. C., Blanks, R., Dunn, G., Gunn, L., Desai, M., Albrow, R., Moss, S. (2011). Automation-assisted Versus Manual Reading of Cervical Cytology (MAVARIC): A Randomized Controlled Trial. *Lancet Oncol, 12*, 56-64.

Kose, A. R., Fischer, B., Mao, L., & Koser, H. (2009). Label-free Cellular Manipulation and Sorting via Biocompatible Ferrofluids. *P Natl Acad Sci USA, 106*, 21478-21483.

Krishnan GP, L. D. (1995). Inertial Lift on a Moving Sphere in Contact with a Plane Wall in a Shear-flow. *Phys Fluids, 7*, 2538–2545.

Lee, H., Liu, Y., Ham, D., & Westervelt, R. M. (2007). Integrated Cell Manipulation System - CMOS/microfluidic Hybrid. *Lab on a Chip, 7*, 331-337.

Li, J., Zhang, Z., Rosenzweig, J., Wang, Y. Y., & Chan, D. W. (2002). Proteomics and Bioinformatics Approaches for Identification of Serum Biomarkers to Detect Breast Cancer. *Clin Chem, 48*, 1296-304.

Liu, C., Stakenborg, T., Peeters, S., & Lagae, L. (2009). Cell Manipulation with Magnetic Particles Toward Microfluidic Cytometry. *Journal of Applied Physics, 105*, 102014-11.

Loutherback, K., Puchalla, J., Austin, R. H., & Sturm, J. C. (2009). Deterministic Microfluidic Ratchet. *Physical review letters, 102*(045301).

Mayrand, M. H., Duarte-Franco, E., Rodrigues, I., Walter, S. D., Hanley, J., Ferenczy, A., Ratnam, S., Coutlee, F., Franco, E. L. (2007). Human Papillomavirus DNA Versus Papanicolaou Screening Tests for Cervical Cancer. *N Engl J Med*, 1579-88.

Mihajlovic, G., Aledealat, K., Xiong, P., Von Molnar, S., Field, M., & Sullivan, G. J. (2009). Magnetic Characterization of a Single Superparamagnetic Bead by Phase-Sensitive Micro-Hall Magnetometry. *Applied Physics Letters, 91*.

Miller, M. M., Sheehan, P. E., Edelstein, R. L., Tamanaha, C. R., Zhong, L., Bounnak, S., Whitman, L., Colton, R. J. (2001). A DNA Array Sensor Utilizing Magnetic Microbeads and Magnetoelectronic Detection. *Journal of Magnetism and Magnetic Materials, 225*, 138-144.

Miltenyi, S., Muller, W., Weichel, W., & Radbruch, A. (1990). High Gradient Magnetic Cell Separation with MACS. *Cytometry, 11*, 231-8.

Morgan, N. G. (1997). Dielectrophoretic Investigations of Sub-micrometre Latex Spheres. *J. Phys. D: Appl.*

Muller, T., Pfennig, A., Klein, P., Gradl, G., Jager, M., & Schnelle, T. (2003). The Potential of Dielectrophoresis for Single-cell Experiments. *Ieee Engineering in Medicine and Biology Magazine, 22*, 51-61.

Nagrath, S., Sequist, L. V., Maheswaran, S., Bell, D. W., Irimia, D., Ulkus, L., Smith, M. R., Kwak, E. L., Digumarthy, S., Muzikansky, A., Ryan, P., Balis, U. J., Tompkins, R. G., Haber, D. A. Toner, M. (2007). Isolation of Rare Circulating Tumour Cells in Cancer Patients by Microchip Technology. *Nature, 450*, 1235-1239.

Nieminen, P., Kotaniemi, L., Hakama, M., Tarkkanen, J., Martikainen, J., Toivonen, T., Ikkala, J., Luostarinen, T., Anttila, A. (2005). A Randomised Public-health Trial on Automation-assisted Screening for Cervical Cancer in Finland: Performance with 470,000 Invitations. *Int J Cancer, 115*, 307-11.

Odenbach, S. (2002). Ferrofluids: Magnetically Controllable Fluids and Their Applications.

Odenbach, S. (2002). Magnetoviscous Effects in Ferrofluids.

Odenbach, S. (2009). Colloidal Magnetic Fluids - Basics, Development and Applications of Ferrofluids. *Springer: Berlin*.

Pamme, N. (2006). Magnetism and Microfluidics. *Lab Chip, 6*, 24-38.

Pamme, N. (2007). Continuous Flow Separations in Microfluidic Devices. *Lab Chip, 7,* 1644-1659.

Pamme, N., & Manz, A. (2004). On-Chip Free-Flow Magnetophoresis: Continuous Flow Separation of Magnetic Particles and Agglomerates. *Anal. Chem., 76*, 7250-7256.

Pamme, N., & Wilhelm, C. (2006). Continuous Sorting of Magnetic Cells via On-chip Free-flow Magnetophoresis. *Lab Chip, 6*, 974-980.

Park, K., Suk, H. J., Akin, D., & Bashir, R. (2009). Dielectrophoresis-based Cell Manipulation Using Electrodes on a Reusable Printed Circuit Board. *Lab Chip, 9*, 2224-9.

Rida, A., & Gijs, M. A. (2004). Manipulation of Self-assembled Structures of Magnetic Beads for Microfluidic Mixing and Assaying. *Analytical Chemistry, 76*, 6239-6246.

Rife, J. C., Miller, M. M., Sheehan, P. E., Tamanaha, C. R., Tondra, M., & Whitman, L. J. (2003). Design and Performance of GMR Sensors for the Detection of Magnetic Microbeads in Biosensors. *Sensor Actuat a-Phys, 107*, 209-218.

Rosensweig RE, L. W. (n.d.). Magnetically Stabilized Fluidized-beds for Solids Separation by Density. *Sep Sci Technol*, 25–45.

Rosensweig, R. E. (1985). Ferrohydrodynamics. *Cambridge University Press: Cambridge*.

Ruoli Jiang, B. J. (2013). Dynamic Multi-Channel TMS with Reconfigurable Coil. *IEEE Neural Systems and Rehabilitation Engineering*.

Shevkoplyas, S. S., Siegel, A. C., Westervelt, R. M., Prentiss, M. G., & Whitesides, G. M. (2007). The Force Acting on a Superparamagnetic Bead due to an Applied Magnetic Field. *Lab on a Chip, 7*, 1294-1302.

Staben ME, Z. A. (2003). Motion of a Particle between two Parallel Plane Walls in Low-Reynolds-number Poiseuille Flow. *Phys Fluids, 15*, 1711–1733.

Taotao Zhu, D. J. (2011). Analytical Model of Microfluidic Transport of Non-magnetic Particles in Ferrofluids under the Influence of a Permanent Magnet. *Microfluid Nanofluid*, 1233-125.

Thomas P. Hunt, D. I. (2007). Integrated Circuit/microfluidic Chip to Programmably Trap and Move Cells and Droplets with Dielectrophoresis. *Lab on a Chip, 8*, 81 - 87.

Toner, M., & Irimia, D. (2005). Blood-on-a-chip. *Annu Rev Biomed Eng, 7*, 77-103.

Tornay, R., Braschler, T., Demierre, N., Steitz, B., Finka, A., Hofmann, H., Hubbell, J. A., Renaud, P. (2008). Dielectrophoresis-based Particle Exchanger for the Manipulation and Surface Functionalization of Particles. *Lab Chip, 8*, 267-73.

Tsutsui, H., & Ho, C.-M. (2009). Cell Separation by Non-inertial Force Fields in Microfluidic Systems. *Mechanics Research Communications, 36*, 92-103.

Vernhes, M. C., Cabanes, P. A., & Teissie, J. (1999). Chinese Hamster Ovary Cells Sensitivity to Localized Electrical Stresses. *Bioelectrochemistry and Bioenergetics, 48*, 17-25.

Voldman, J. (2006). Electrical Forces for Microscale Cell Manipulation. *Annu Rev Biomed Eng, 8*, 425-54.

Westervelt, C. F. (2012). A Programmable Hybrid Integrated Circuit / Microfluidic Device for Cell Fusion. *Integrative Biology*.

Westervelt, K. B. (2011). Triaxial AFM Probes for Noncontact Trapping and Manipulation. *Nano Letters*, 3197-3201 .

Whitesides, G. M. (2006). The Origins and the Future of Microfluidics. *Nature*, *442*, 368-373.

Yung, C. W., Fiering, J., Mueller, A. J., & Ingber, D. E. (2009). Micromagnetic-Microfluidic Blood Cleansing Device. *Lab on a Chip, 9*, 1171-7.

Appendix

Theoretical Calculations for Magnetic Buoyancy Force

In this section, we briefly present a more detailed analytical approach that enables the estimation of magnetic buoyancy force on non-magnetic micro particles. We assume a perfectly spherical, incompressible microparticle and a magnetically linear ferrofluid, and a slip factor that is independent of field magnitude and frequency. We further assume that the spherical particle radius (r) is small enough so that the ferrofluids magnetization in the immediate vicinity of the microparticle and the effective magnetization ($\overrightarrow{M}_{eff}$) with in the particle's volume (V_p) can be approximated as uniform. We also assume that the magnetic field is constant within the interior extent of the micro non-magnetic particle. The total instantaneous force on that particle is given by

$$\overrightarrow{F}_m = V_p \nabla(\overrightarrow{M}_{eff} \cdot \overrightarrow{B}), \qquad \text{(a1)}$$

where $\overrightarrow{B}$ is the magnetic flux density within the spherical microparticle, which is assumed to be constant. To obtain the eventual analytical expression for the magnetic buoyancy force, it will be helpful to express $\overrightarrow{M}_{eff}$ and $\overrightarrow{B}$ in terms of the external magnetic field $\overrightarrow{H}$ in the absence of the non-magnetic micro particle, since the externally applied magnetic field can be easily obtained from calculation and simulation. The effective magnetization of the non-magnetic particle depends on $\overrightarrow{H}$ as

$$\overrightarrow{M}_{eff} = 3\left(\frac{\mu_p - \mu_f}{\mu_p + 2\mu_f}\right)\overrightarrow{H}, \qquad \text{(a2)}$$

where μ_p is the permeability of the non-magnetic particle which is essentially μ_0.

$\mu_f = \mu_0(1+\chi_f)$ is the permeability of the ferrofluids. The effective magnetization of non-magnetic particle can be express as

$$\overrightarrow{M}_{eff} = \frac{-3\chi_f}{3+2\chi_f}\overrightarrow{H}. \qquad \text{(a3)}$$

To determine the magnetic flux density and field within the particle requires consideration of the demagnetization field inside it. The overall field inside the particle is $\overrightarrow{H}_{in} = \overrightarrow{H} - \overrightarrow{H}_{dmag}$, with $\overrightarrow{H}_{dmag} = \overrightarrow{M}_{eff}/3$ for a sphere. Hence, in the linear regime where particle magnetization can be written as $\overrightarrow{\mathrm{M}}_{eff} = \chi_{eff}\overrightarrow{H}_{in}$. We can get

$$\overrightarrow{H}_{in} = \frac{\overrightarrow{M}_{eff}}{\chi_{eff}} = \overrightarrow{H} - \frac{\overrightarrow{M}_{eff}}{3} \Rightarrow \overrightarrow{M}_{eff} = (\frac{3\chi_{eff}}{3+\chi_{eff}})\overrightarrow{H}. \qquad \text{(a4)}$$

Comparing Equation a3 and a4 reveals the effective susceptibility of the particle in terms of the susceptibility of ferrofluids:

$$\chi_{eff} = \frac{-\chi_f}{1+\chi_f}. \qquad \text{(a5)}$$

Note that the effective magnetic susceptibility of non-magnetic particle depends on the susceptibility of ferrofluids, since non-magnetic micro particle responds to magnetic forces only because it displaces ferrofluids and creates a “magnetic hole”. In that regard, the magnetic medium in which the hole resides determines the strength of the interactions between that magnetic hole and externally applied fields. The negative sign in Equation a5 indicates that the effective magnetization of the microparticle is in the opposite direction of eh local ferrofluids, and this is why magnetic buoyancy force always points to region where magnetic flux density is lower. For $\chi_f << 1$, $\chi_{eff} \approx -\chi_f$. In a strong magnetisable medium (χ_f is large), the effective susceptibility of the magnetic

hole approaches -1.

The instantaneous magnetic buoyancy force on the non-magnetic particle can be expressed as

$$\vec{F}_m = V_p \mu_0 \nabla(\vec{M}_{eff} \cdot (\vec{H}_{in} + \vec{M}_{eff})) = V_p \mu_0 \nabla(\left|\vec{M}_{eff}\right|^2 \frac{\mathrm{Re}\{\chi_{eff}\}}{\left|\chi_{eff}\right|^2} + \left|\vec{M}_{eff}\right|^2). \quad \text{(a6)}$$

By applying Equation a4, we get:

$$\vec{F}_m = V_p \mu_0 (\frac{\mathrm{Re}\{\chi_{eff}\}}{\left|\chi_{eff}\right|^2} + 1)(\frac{9\left|\chi_f\right|^2}{9 + 6\,\mathrm{Re}\{\chi_f\} + 4\left|\chi_f\right|^2})\nabla\left|\vec{H}\right|^2. \quad \text{(a7)}$$

Chamber Design and Fabrication

The microfluidic chamber was designed and fabricated by Dr. Mao of the University of Georgia, Athens. The fabrication of poly(dimethylsiloxane) (PDMS) microfluidic device was primarily based on the standard soft lithography techniques. A mask of the device pattern was designed with AutoCAD software and produced by a commercial photo-plotting company (CAD/Art Services Inc., Chadds Ford, PA) with resolution 20000 dpi. SU-8 2025, a negative photoresist, was used to produce microfluidic device spin-coated silicon wafer. Then it was exposed to ultra-violet (UV) light that passes through the UV mask. After the UV processing, the silicon wafer was placed in a petri dish containing a few drops of chlorotrimethylsilane, which facilitates the removal of PDMS replica from the silicon wafer. A 10:1 mixture of PDMS prepolymer and curing agent was stirred thoroughly and degassed under vacuum three times. Then the prepolymer mixture was poured onto the photoresist mold and cured for 2 h at 72 ^{0}C. After curing, the PDMS replica was peeled from the mold and followed by attaching to a cover glass (No. 1). They were placed in a plasma cleaner (PDC-32G plasma cleaner, Harrick Plasma, Ithaca, NY) and oxidized at 11.2 Pa O_2 partial pressure

with 18W power for 30 s before attachment. The microfluidic channel has dimensions of 10 mm in length and 3 mm in width. Thickness of the device was measured to be 50 μm by a profilometer (Dektak 150, Veeco Instruments Inc., Chadds Ford, PA). Before sample injection, the device was placed in the plasma cleaner and oxidized for 10 min to render PDMS surfaces hydrophilic. This step reduced microparticles attachment onto PDMS surfaces during experiments.